Measuring asymmetry in strange beauty

Govorkova, E.

2020

document version
Publisher's PDF, also known as Version of record

Measuring asymmetry in strange beauty

Katya Govorkova

Cover designed using the Deep Dream Generator
Printed by Gildeprint – The Netherlands
ISBN 978-94-6402-263-6

This work is part of the research program of the Netherlands Organization for Scientific Research (NWO). It was carried out at the National Institute for Subatomic Physics (Nikhef) in Amsterdam, the Netherlands.

VRIJE UNIVERSITEIT

Measuring asymmetry in strange beauty

ACADEMISCH PROEFSCHRIFT

ter verkrijging van de graad Doctor aan
de Vrije Universiteit Amsterdam,
op gezag van de rector magnificus
prof.dr. V. Subramaniam,
in het openbaar te verdedigen
ten overstaan van de promotiecommissie
van de Faculteit der Bètawetenschappen
op woensdag 1 juli 2020 om 9.45 uur
in de aula van de universiteit,
De Boelelaan 1105

door

Ekaterina Govorkova

geboren te Moscow, Rusland

promotor: prof.dr. H.G. Raven
copromotor: dr. P. Koppenburg

Potius deficere quam desperare

Contents

Introduction

Our knowledge of the fundamental constituents of the universe and of their interactions has developed into the Standard Model (SM) of Particle Physics [1]. Despite the success of the model in predicting an abundance of phenomena with great precision, the Standard Model is an incomplete description of the universe and several important observations are left unexplained. One of such puzzles is the observed matter-anti-matter asymmetry in the universe. According to the cosmological model [2], an equal amount of matter and anti-matter has been created at the moment of the Big Bang, which should have annihilated with each other leaving our universe made purely of photons. However, what we observe is a matter-dominated universe, which means that there exists an asymmetry in the behaviour of matter and anti-matter.

The discrete symmetries of the SM are, among others, charge conjugation (C), parity (P), which reverses the handedness of space, and time reversal (T), which interchanges the forward and backward light-cones. The combined CP transformation replaces a particle with its anti-particle and reverses both momentum and helicity. Sakharov [3] postulated three conditions required to generate the observed matter-anti-matter asymmetry in the universe, one of which is the breaking of both C and CP symmetries in any model of particle interactions. The combined CPT transformation is however an exact symmetry in any local Lagrangian field theory [4]. Violation of the C and CP symmetries is present in the weak sector of the SM, but the amount of CP violation (CPV) is not enough to explain the observed matter-dominance [5].

Some extensions of the SM can violate CP symmetry and therefore can bring additional CP-violating couplings. Measuring CP violation is an indirect approach to search for physics beyond the SM, usually referred to as New Physics (NP). One of the systems that are used to measure CPV is the neutral B_s^0 meson. During its lifetime a B_s^0 meson may oscillate to its anti-particle $\overline{B}_s^0$ and back. This mixing process occurs via a second-order weak amplitude [6], that is sensitive to potential contributions from NP. The B_s^0 meson is not a stable particle, and its lifetime is measured to be $(1.510 \pm 0.004) \times 10^{-12}$ s [7]. One of the key decay mode of the B_s^0 meson that is used to measure CP violation is the $B_s^0 \to J/\psi\phi$ decay. Due to the presence of CPV in the SM, the total probability of the $B_s^0 \to J/\psi\phi$ decay is different from that of the $\overline{B}_s^0 \to J/\psi\phi$ decay, as explained in details in Chapter 1. The parameter that characterises this difference is the CP-violating phase ϕ_s. The value of ϕ_s is inferred in the SM with great precision to be $-0.03698^{+0.00081}_{-0.00070}$ rad [8, 9]. A direct experimental measurement of ϕ_s that differs from the expected value would be an indirect observation of a NP contribution.

The phase ϕ_s is measured in $B_s^0 \to J/\psi\phi$ decays using proton-proton collision data, corresponding to an integrated luminosity of $1.9\,\text{fb}^{-1}$, collected with the LHCb detector [10] at a centre-of-mass energy of 13 TeV in 2015 and 2016. LHCb is a dedicated experiment at the LHC [11] at CERN designed specifically to study CP-violating effects and to measure related quantities. The description of the detector is given in Chapter 2. The decay of B_s^0 to $J/\psi\phi$ is usually referred to as the "golden mode" to measure CP violation in B_s^0 system, since it has a branching fraction that is measured to be $(1.08 \pm 0.08) \times 10^{-3}$ [7] which is large in comparison to typical exclusive branching fractions for B_s^0 decays, and it has a clear experimental signature with $\mu^+\mu^-$ and K^+K^- pairs in the final state. The details on the experimental analysis performed using data collected by the LHCb experiment are presented in Chapter 4.

CP violation was first discovered in the kaon system [12], followed by observations in the B^0 [13] and B_s^0 systems [14]. Recently, breaking of the CP symmetry was observed in the decays of D^0 mesons [15], as well. The latter two observations were done with the LHCb detector. The main focus of the experiment is the study of the systems that contain a b quark. The physics program has been successfully extended to the study of systems containing a c quark. The challenge of charm physics is that the rate of $c\bar{c}$ pair production is 25 times larger than that of $b\bar{b}$ pairs. Stronger selection requirements have to be applied in order to fit into the the limited computer resources of the experiment. To overcome this limitation, a novel framework, that makes use of a reduced format, was implemented in the LHCb experiment. The extension of this framework, allowing for flexibility in specifying objects to be persisted is explained in detail in Chapter 3. The introduction of this framework made it possible to keep the accepted rate of charm physics high, and a lot of charm physics measurements, including the aforementioned observation of the CPV, became possible. Moreover, the framework is to become the default for the LHCb experiment in the upcoming Run 3 period of data-taking.

Chapter 1

Theory

In the Standard Model (SM) of elementary particles, the fundamental constituents of baryonic matter are quarks that come in six flavours, and which are organised in three families. Each family consists of one up-type quark with electric charge $+\frac{2}{3}$ e and one down-type quark with electric charge $-\frac{1}{3}$ e. Each quark has a corresponding anti-particle, anti-quark, which has the same mass and lifetime as quark (due to the CPT theorem [4]), but opposite quantum numbers for both charge and flavour. The changing of quark flavour in the SM is described by the weak force, whose three force carriers are the W^+, W^- and Z bosons. Changes of flavour in the SM can however only proceed via a charged current, i.e. through an intermediate $W^\pm$ boson.

1.1 CKM matrix

The coupling strength between quarks and the $W^\pm$ boson is proportional to the corresponding element in the Cabibbo–Kobayashi–Maskawa (CKM) matrix [16, 17], V^{CKM}. The CKM matrix is a unitary 3×3 matrix, corresponding to the three quark families in the SM. It is parametrised by 3 rotation angles and one irreducible complex phase. This single complex phase is the sole source of CP violation in the quark sector of the SM.

The CKM matrix exhibits an unexplained hierarchy, namely that the transitions inside one family, characterized by the diagonal elements, are favoured, while the transitions between different families are suppressed. This hierarchy is exploited by the Wolfenstein parametrisation [18] which uses four parameters. Three, A, ρ and η, are numbers of order unity, and the fourth, λ, is measured to be approximately 0.23 and plays the role of expansion parameter. The V^{CKM} matrix in the Wolfenstein

parametrisation reads as

$$V^{\mathrm{CKM}} = \begin{pmatrix} |V_{ud}| & |V_{us}| & |V_{ub}|e^{-i\gamma} \\ -|V_{cd}| & |V_{cs}| & |V_{cb}| \\ |V_{td}|e^{-i\beta} & -|V_{ts}|e^{i\beta_s} & |V_{tb}| \end{pmatrix} = \begin{pmatrix} 1-\lambda^2/2 & \lambda & A\lambda^3(\rho - i\eta) \\ -\lambda & 1-\lambda^2/2 & A\lambda^2 \\ A\lambda^3(1-\rho-i\eta) & -A\lambda^2 & 1 \end{pmatrix} + O(\lambda^4),$$

where β, β_s and γ are the angles of unitarity triangles defined in section 1.2. The magnitudes and the phases of the individual V^{CKM} elements are not predicted in the SM and can only be measured experimentally.

1.2 Unitarity triangles

The unitarity of the CKM matrix, imposed by the conservation of probability, implies various relations between its elements, i.e. $\sum_k V_{ik} V_{jk}^* = \delta_{ij}$. For the off-diagonal elements, these constraints can be interpreted as triangles formed in a complex plane. Two out of six of those triangles have sides of similar sizes, i.e. all terms are of the same order in λ, and are relevant for B-decays. These two triangles correspond to

$$V_{ud} V_{ub}^* + V_{cd} V_{cb}^* + V_{td} V_{tb}^* = 0\,, \tag{1.1}$$

$$V_{td} V_{ud}^* + V_{ts} V_{us}^* + V_{tb} V_{ub}^* = 0\,, \tag{1.2}$$

where the first one is usually referred to as the Unitarity triangle. The convention-independent definition of the angles is

$$\alpha \equiv \arg\left[-\frac{V_{td}V_{tb}^*}{V_{ud}V_{ub}^*}\right], \beta \equiv \arg\left[-\frac{V_{cd}V_{cb}^*}{V_{td}V_{tb}^*}\right], \gamma \equiv \arg\left[-\frac{V_{ud}V_{ub}^*}{V_{cd}V_{cb}^*}\right], \tag{1.3}$$

$$\beta_s \equiv \arg\left[-\frac{V_{ts}V_{tb}^*}{V_{cs}V_{cb}^*}\right].$$

The measurement of the sides and angles of these triangles and consistency between them serves as an important test of the SM. Any apparent violation of unitarity would imply the presence of additional amplitudes that contribute in some way to the decays under study, but which are not described by the SM. The current experimental status on the measurements of the CKM triangles is shown in figure 1.1.

1.3 Neutral meson mixing

The interactions between quarks are described by the strong force in the SM, with the gluon as force carrier. Quarks carry colour and anti-quarks carry anti-colour, and they combine together to form colour-neutral objects, called hadrons. So far only colourless objects have been observed in nature; this phenomenon is called colour

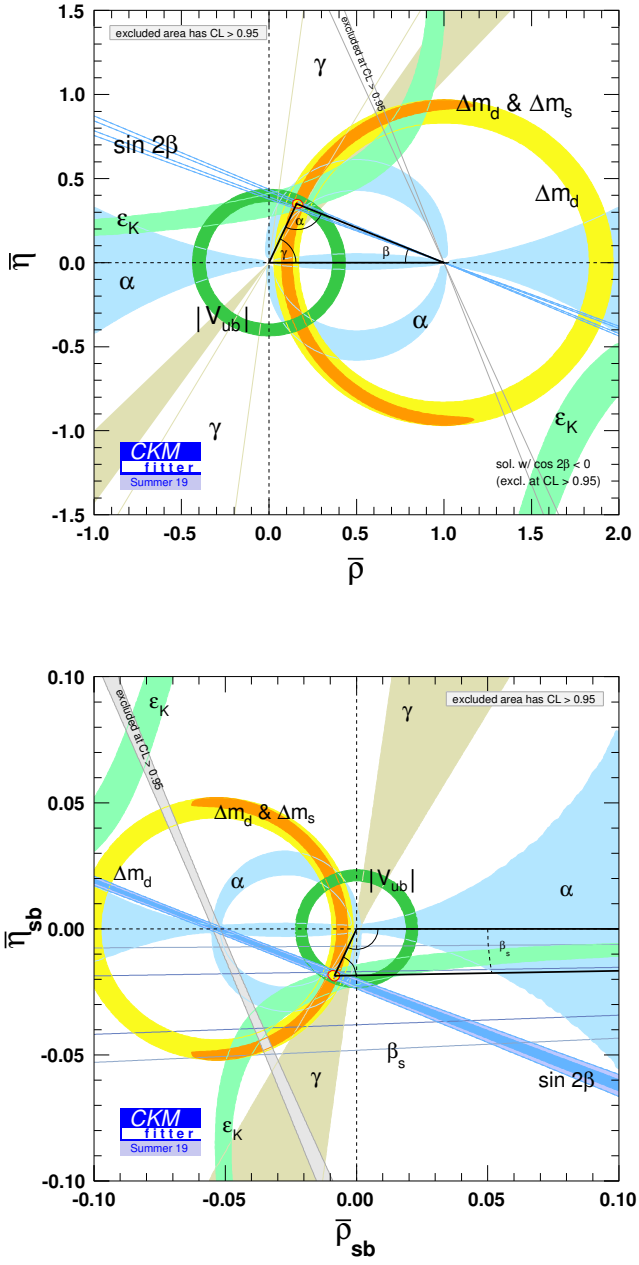

Figure 1.1: Current experimental status on the measurement of the CKM triangles parameters [8, 9]. Where $\bar{\rho} + i\bar{\eta} \equiv \frac{V_{ud}V_{ub}^*}{V_{cd}V_{cb}^*}$ and $\bar{\rho}_{sb} + i\bar{\eta}_{sb} \equiv \frac{V_{us}V_{ub}^*}{V_{cs}V_{cb}^*}$. The ε_K is the CP-violating parameter of the neutral kaon system.

confinement [1]. Mesons are colourless bound states of quarks and anti-quarks. The system of interest is the B_s^0 meson, an electrically neutral particle, that consists of a b anti-quark and an s quark. There are two distinct flavour eigenstates B_s^0 ($\bar{b}s$) and $\overline{B}_s^0$ ($b\bar{s}$) that each have a definite quark content and which are relevant for describing

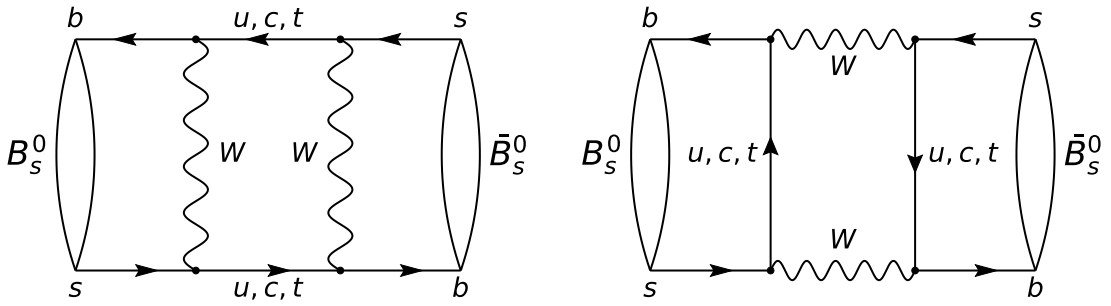

Figure 1.2: Feynman diagrams for $B_s^0 - \overline{B}_s^0$ oscillations. Diagrams are created using open source software [19].

both particle production and decay processes. The eigenstates of the Hamiltonian that governs the time evolution, with definite masses and lifetimes, evolve in time in a definite fashion. These eigenstates are not identical to the flavour eigenstates. As a result, the flavour eigenstates can interchange with each other while evolving as a function of time. This phenomenon is called neutral-meson mixing. Two possible Feynman diagrams for the B_s^0 meson oscillation process are shown in figure 1.2. The mixing proceeds via a flavour-changing neutral current, FCNC. In the SM, FCNC transitions are forbidden at tree level and can only occur via loop processes, which are heavily suppressed in the SM [6]. Due to this suppression, B_s^0 meson mixing is very sensitive to potential contributions from physics beyond the SM.

1.4 CP violation

Measuring CP violation allows for access to the complex phase, which is only possible if at least two amplitudes contribute to the process. The phase of each amplitude can be decomposed into a CP-odd weak phase and a CP-even phase that usually originates from the gluon exchange or from the dynamics of the mixing as in the case of $B_s^0 \to J/\psi\phi$ decay. As the weak force breaks CP, the corresponding phase changes sign under CP transformation while the CP-even phase does not. Thus the magnitude of the total amplitude can be different from its CP-conjugate. The CP-violating parameters can therefore be measured through the observed difference in the total amplitudes of a process and its CP-conjugate.

1.5 Anatomy of $B_s^0 \to J/\psi\phi$ decay

The decay mode exploited in this thesis in detail is the $B_s^0 \to J/\psi\phi$ transition. It allows to probe New Physics in CP violation introduced by the interference between direct decay and decay after mixing. The B_s^0 meson, being a neutral particle, can either

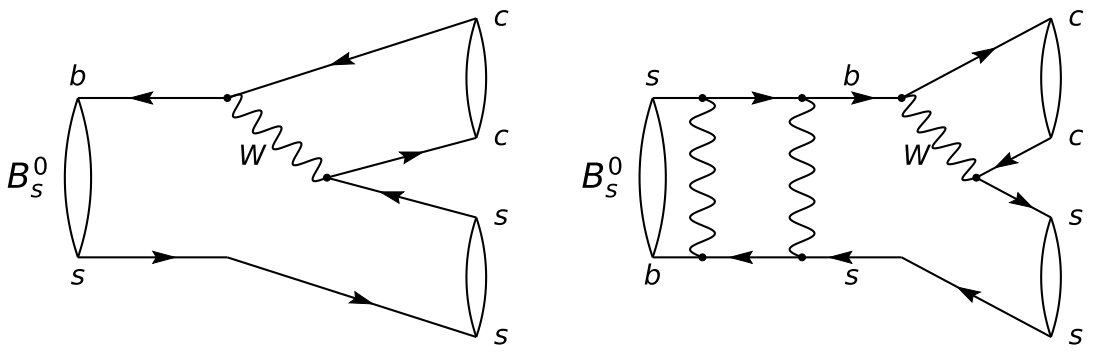

Figure 1.3: Feynman diagrams for $B_s^0 \to J/\psi\phi$ decay. The diagrams are created using open source software [19].

decay directly to the flavour eigenstate $J/\psi\phi$ or first oscillate to its anti-particle, the $\overline{B}_s^0$ meson, and then decay to the same final state. Therefore there are two interfering amplitudes that contribute to the total probability of the decay, and the corresponding diagrams are shown in figure 1.3.

To access CPV experimentally, the differential time-dependent decay rate of B_s^0 meson to the final state $J/\psi\phi$ is measured, which is defined as [20]

$$\frac{d\Gamma(B_s^0(t) \to J/\psi\phi)}{dt} = \frac{1}{N_{B_s^0}} \frac{dN(B_s^0(t) \to J/\psi\phi)}{dt} \tag{1.4}$$

for $B_s^0(t)$ identified as B_s^0 meson at $t = 0$, where $dN(B_s^0(t) \to J/\psi\phi)$ is the number of B_s^0 decays into the final state $J/\psi\phi$, occurring in a time interval $[t; t + dt]$, and $N_{B_s^0}$ the total number of B_s^0 mesons produced at $t = 0$.

1.5.1 Time evolution

The time evolution of an arbitrary $a(t)|B_s^0\rangle + b(t)|\overline{B}_s^0\rangle$ state, representing a superposition of the B_s^0 and $\overline{B}_s^0$ flavour eigenstates, i.e. those with a well-defined quark content, is governed by the time-dependent Schrödinger equation [21]

$$i\frac{d}{dt}\begin{pmatrix} a(t) \\ b(t) \end{pmatrix} = H\begin{pmatrix} a(t) \\ b(t) \end{pmatrix}. \tag{1.5}$$

The non-Hermitian H matrix can be decomposed as two 2×2 Hermitian matrices $M = M^\dagger$ and $\Gamma = \Gamma^\dagger$

$$H\begin{pmatrix} a(t) \\ b(t) \end{pmatrix} = \left(M - i\frac{\Gamma}{2}\right)\begin{pmatrix} a(t) \\ b(t) \end{pmatrix} = \begin{pmatrix} M - \frac{i}{2}\Gamma & M_{12} - \frac{i}{2}\Gamma_{12} \\ M_{12}^* - \frac{i}{2}\Gamma_{12}^* & M - \frac{i}{2}\Gamma \end{pmatrix}\begin{pmatrix} a(t) \\ b(t) \end{pmatrix}, \tag{1.6}$$

where the presence of the off-diagonal elements is due to the mixing process. Because of the CPT invariance $M_{11} = M_{22}$ and $\Gamma_{11} = \Gamma_{22}$, as well as for the off-diagonal elements

$M_{21} = M_{12}^*$ and $\Gamma_{21} = \Gamma_{12}^*$ which implies that for particles and their anti-particles, both mass and total decay width are identical. The eigenstates of the Hamiltonian that have well defined masses and lifetimes, usually referred to as light (B_L) and heavy (B_H) mass eigenstates, are quantum-mechanical superpositions of the flavour eigenstates with (complex) coefficients p and q

$$|B_L\rangle = p|B_s^0\rangle + q|\overline{B}_s^0\rangle, \; |B_H\rangle = p|B_s^0\rangle - q|\overline{B}_s^0\rangle, \tag{1.7}$$
$$\text{with } \frac{q}{p} = \pm\left[\frac{M_{12}^* - i\Gamma_{12}^*/2}{M_{12} - i\Gamma_{12}/2}\right]^{1/2} \text{ and } |p|^2 + |q|^2 = 1,$$

and with the corresponding eigenvalues $M_{L,H} - \frac{i}{2}\Gamma_{H,L}$. Solving the Schrödinger equation gives the time evolution for its eigenstates B_L and B_H

$$|B_L(t)\rangle = e^{-iM_L t - \frac{1}{2}\Gamma_L t}|B_L(0)\rangle, \tag{1.8}$$
$$|B_H(t)\rangle = e^{-iM_H t - \frac{1}{2}\Gamma_H t}|B_H(0)\rangle. \tag{1.9}$$

The B_s^0 system is usually described with the following four quantities

$$m_s = \frac{M_H + M_L}{2} \text{ and } \Gamma_s = \frac{\Gamma_H + \Gamma_L}{2}, \tag{1.10}$$
$$\Delta m_s = M_H - M_L \text{ and } \Delta\Gamma_s = \Gamma_L - \Gamma_H.$$

The mass difference, Δm_s, is chosen to be positive and the sign of the width difference, $\Delta\Gamma_s$, was determined to be positive in reference [22].

The time evolution of the initially pure B_s^0 or $\overline{B}_s^0$ states can be deduced combining equations 1.8 and 1.9:

$$|B_s^0(t)\rangle = g_+(t)|B_s^0\rangle + \frac{q}{p}\,g_-(t)|\overline{B}_s^0\rangle,$$
$$|\overline{B}_s^0(t)\rangle = \frac{p}{q}\,g_-(t)|B_s^0\rangle + g_+(t)|\overline{B}_s^0\rangle, \tag{1.11}$$
$$\text{with } g_\pm(t) = \frac{1}{2}\left(e^{-iM_H t - \frac{1}{2}\Gamma_H t} \pm e^{-iM_L t - \frac{1}{2}\Gamma_L t}\right).$$

1.5.2 Decay to the J/ψφ final state

The next step is to take into account the decay of the B_s^0 meson. The decay amplitudes of a time-evolved B_s^0 and $\overline{B}_s^0$ into the J/ψφ final state are

$$\langle J/\psi\phi|B_s^0(t)\rangle = g_+(t)\langle J/\psi\phi|B_s^0\rangle + \frac{q}{p}\,g_-(t)\langle J/\psi\phi|\overline{B}_s^0\rangle, \tag{1.12}$$
$$\langle J/\psi\phi|\overline{B}_s^0(t)\rangle = \frac{p}{q}\,g_-(t)\langle J/\psi\phi|B_s^0\rangle + g_+(t)\langle J/\psi\phi|\overline{B}_s^0\rangle. \tag{1.13}$$

The time-dependent decay rates for the $B_s^0 \to J/\psi\phi$ and $\overline{B}_s^0 \to J/\psi\phi$ decays becomes

$$\frac{d\Gamma(B_s^0(t) \to J/\psi\phi)}{dt} = |\langle J/\psi\phi|B_s^0(t)\rangle|^2 = \tag{1.14}$$
$$|A|^2 \frac{1+|\lambda|^2}{2} e^{-\Gamma_s t}\left[\cosh\frac{\Delta\Gamma_s t}{2} + D\sinh\frac{\Delta\Gamma_s t}{2} + C\cos(\Delta m_s t) - S\sin(\Delta m_s t)\right],$$
$$\frac{d\Gamma(\overline{B}_s^0(t) \to J/\psi\phi)}{dt} = |\langle J/\psi\phi|\overline{B}_s^0(t)\rangle|^2 = \tag{1.15}$$
$$|A|^2 \left|\frac{p}{q}\right|^2 \frac{1+|\lambda|^2}{2} e^{-\Gamma_s t}\left[\cosh\frac{\Delta\Gamma_s t}{2} + D\sinh\frac{\Delta\Gamma_s t}{2} - C\cos(\Delta m_s t) + S\sin(\Delta m_s t)\right],$$

where $\lambda \equiv \frac{q}{p}\frac{\overline{A}}{A}$, $D \equiv -\frac{2\Re(\lambda)}{1+|\lambda|^2}$, $C \equiv \frac{1-|\lambda|^2}{1+|\lambda|^2}$, $S \equiv \frac{2\Im(\lambda)}{1+|\lambda|^2}$, and where the two decay amplitudes of A and $\overline{A}$ are defined as $A \equiv \langle J/\psi\phi|B_s^0\rangle$ and $\overline{A} \equiv \langle J/\psi\phi|\overline{B}_s^0\rangle$. The complex parameter λ is used to characterize CP violation, since it has a convention-independent, physically meaningful, phase. In $B_s^0 \to J/\psi\phi$ case it is

$$\lambda = (-1)^l \left(\frac{V_{tb}^* V_{ts}}{V_{tb} V_{ts}^*}\right)\left(\frac{V_{cb} V_{cs}^*}{V_{cb}^* V_{cs}}\right) \tag{1.16}$$

where l is the relative momentum between the two vector particles (spin-1), the J/ψ and ϕ mesons. Due to the conservation of the total angular momentum and keeping in mind that the B_s^0 is a spinless particle, the orbital momentum between the J/ψ and ϕ mesons must compensate the relative orientation of their spin projections. The orbital momentum can take the values $l = 0, 1$ or 2. The CP eigenvalue of the final state depends on the angular momentum as $CP|J/\psi\phi\rangle_l = (-1)^l|J/\psi\phi\rangle_l$, the $J/\psi\phi$ state is therefore a superposition of two CP-eigenstates, CP-even and CP-odd. Depending on the relative spin orientation, there are three polarisation amplitudes contributing to the total amplitude of the process, $A_\parallel$ and A_0 that are CP-even and $A_\perp$ that is CP-odd. The different contributions have to be statistically separated from each other, since two out of the four terms in their expressions contribute with opposite sign in the decay rate, diluting the measurement of ϕ_s. Depending on the relative angular momentum, the final state particles follow specific angular distributions that can be used to distinguish between the different components. The angular configuration of the four-body final state is determined by three independent angles. The helicity angles formalism is used with three angles being θ_μ, θ_K and ϕ_h, as shown in figure 1.4.

Both the J/ψ and the ϕ final states are resonances that decay to a $\mu^+\mu^-$ and K^+K^- pair, respectively. However, the K^+K^- final state can also be reached directly, without an intermediate ϕ resonance, or through the spin-zero $f_0(980)$ resonance. These contributions have to be taken into account. Since both of them have spin equal to zero, the total contribution is denoted with the CP-odd amplitude A_S and it is referred to as S-wave. Due to the presence of the S-wave, the $B_s^0 \to J/\psi\phi$ decay mode will be referred to with $B_s^0 \to J/\psi K^+K^-$ in the following text.

The description of the $B_s^0 \to J/\psi K^+K^-$ transition requires in total four amplitudes, $A_\parallel$, $A_\perp$, A_0 and A_S; and three relative strong phases, $\delta_\parallel - \delta_0$, $\delta_\perp - \delta_0$ and $\delta_S - \delta_\perp$,

where by convention δ_0 is zero. The phase of the S-wave amplitude depends on the invariant mass of the K^+K^- combination, as explained in Chapter 4.

The phase of λ for $B_s^0 \to J/\psi K^+K^-$ decay consists of two parts. The weak decay phase defined as $\phi_D \equiv \arg(V_{cs}V_{cb}^*)$ and the weak mixing phase, $\phi_M \equiv \arg(M_{12}) \approx -\frac{(V_{ts}V_{tb}^*)}{(V_{ts}^*V_{tb})}$. The total phase equal to $\phi_M - 2\phi_D$ is denoted ϕ_s. It describes the CP violation in $b \to c\bar{c}s$ transition. It is measured as an amplitude of the time-dependent CP asymmetry, which is defined as

$$\mathcal{A}^{CP}(t) = \frac{\Gamma(B_s^0(t) \to J/\psi\phi) - \Gamma(\overline{B}_s^0(t) \to J/\psi\phi)}{\Gamma(B_s^0(t) \to J/\psi\phi) + \Gamma(\overline{B}_s^0(t) \to J/\psi\phi)} \propto \sin(\phi_s)\sin(\Delta m_s t)\,. \qquad (1.17)$$

In the SM, taking into account only tree processes for decay, this phase, ${\phi_s}^{SM,tree}$ is equal to $-2\beta_s$, where β_s is an angle of the unitarity triangle for B_s^0 meson. The value of $-2\beta_s$ is obtained from global fits to experimental data to be $-0.03698^{+0.00081}_{-0.00070}$ rad [8,9].

1.5.3 Contribution from penguin diagrams

What is measured experimentally by determining the CP asymmetry in $B_s^0 \to J/\psi K^+K^-$ given in equation 1.17 is the phase

$${\phi_s}^{exp} = {\phi_s}^{SM,tree} + {\phi_s}^{SM,penguin} + \Delta{\phi_s}^{NP},$$

where ${\phi_s}^{SM,penguin}$ arises from the penguin contribution in the $B_s^0 \to J/\psi K^+K^-$ transition and $\Delta{\phi_s}^{NP}$ is the potential contribution from physics processes beyond the SM description. The contribution from the penguin diagrams is carefully studied both theoretically [24] and experimentally [25]. To ensure that penguin pollution can be

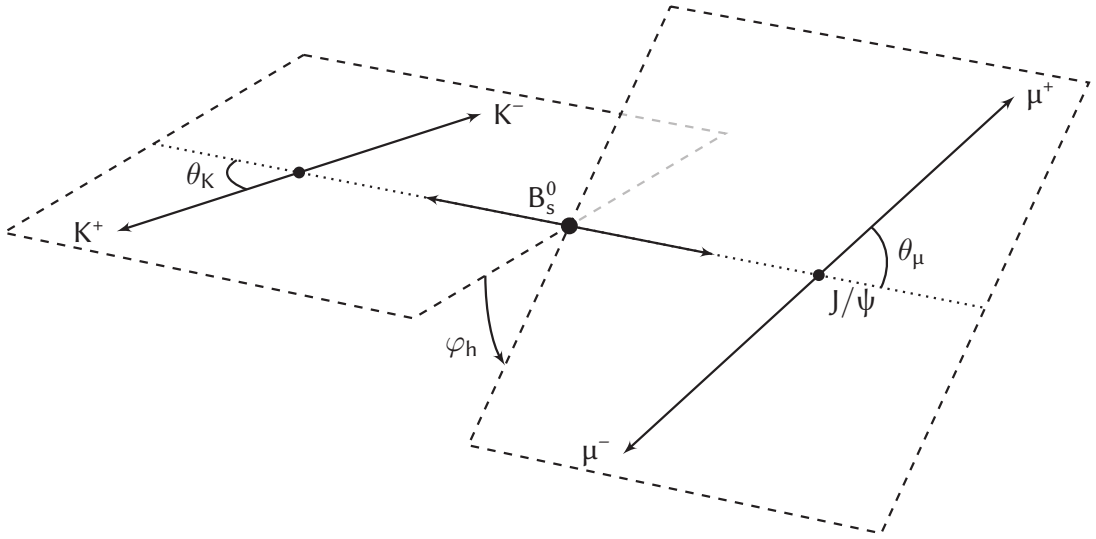

Figure 1.4: The three angles in the helicity formalism that described the angular configuration of the $J/\psi K^+K^-$ system. The plot is taken from reference [23].

Table 1.1: Definition of the functions $h_k(t|B_s^0)$, $h_k(t|\overline{B}_s^0)$ and $f_k(\theta_\mu, \theta_K, \phi_h)$.

k	$h_k(t\|B_s^0)$	$h_k(t\|\overline{B}_s^0)$	$f_k(\theta_\mu, \theta_K, \phi_h)$
1	$\|A_0(t)\|^2$	$\|\overline{A}_0(t)\|^2$	$4\sin^2\theta_\mu\cos^2\theta_K$
2	$\|A_\parallel(t)\|^2$	$\|\overline{A}_\parallel(t)\|^2$	$(1+\cos^2\theta_\mu)\sin^2\theta_K - \sin^2\theta_\mu\sin^2\theta_K\cos 2\phi_h$
3	$\|A_\perp(t)\|^2$	$\|\overline{A}_\perp(t)\|^2$	$(1+\cos^2\theta_\mu)\sin^2\theta_K + \sin^2\theta_\mu\sin^2\theta_K\cos 2\phi_h$
4	$\Im\{A_\parallel{}^*(t)A_\perp(t)\}$	$\Im\{\overline{A}_\parallel{}^*(t)\overline{A}_\perp(t)\}$	$2\sin^2\theta_\mu\sin^2\theta_K\sin 2\phi_h$
5	$\Re\{A_0{}^*(t)A_\parallel(t)\}$	$\Re\{\overline{A}_0{}^*(t)\overline{A}_\parallel(t)\}$	$-\sqrt{2}\sin 2\theta_\mu\sin 2\theta_K\cos\phi_h$
6	$\Im\{A_0{}^*(t)A_\perp(t)\}$	$\Im\{\overline{A}_0{}^*(t)\overline{A}_\perp(t)\}$	$\sqrt{2}\sin 2\theta_\mu\sin 2\theta_K\sin\phi_h$
7	$\|A_S(t)\|^2$	$\|\overline{A}_S(t)\|^2$	$\frac{4}{3}\sin^2\theta_\mu$
8	$\Re\{A_S{}^*(t)A_\parallel(t)\}$	$\Re\{\overline{A}_S{}^*(t)\overline{A}_\parallel(t)\}$	$-\frac{2}{3}\sqrt{6}\sin 2\theta_\mu\sin\theta_K\cos\phi_h$
9	$\Im\{A_S{}^*(t)A_\perp(t)\}$	$\Im\{\overline{A}_S{}^*(t)\overline{A}_\perp(t)\}$	$\frac{2}{3}\sqrt{6}\sin 2\theta_\mu\sin\theta_K\sin\phi_h$
10	$\Re\{A_S{}^*(t)A_0(t)\}$	$\Re\{\overline{A}_S{}^*(t)\overline{A}_0(t)\}$	$\frac{8}{3}\sqrt{3}\sin^2\theta_\mu\cos\theta_K$

neglected in the measurement of ϕ_s with $B_s^0 \to J/\psi K^+K^-$, decay modes are studied for which the penguin contribution is highly enhanced with respect to the tree one, e.g. $B^0 \to J/\psi\pi^+\pi^-$ [26] and $B_s^0 \to J/\psi\overline{K}^*$ [27] decays. This approach [28–30] requires the measurement of the branching fraction, direct CP asymmetries, and polarisation fractions of the penguin-enhanced decays in order to determine the significance of the penguin pollution for the $B_s^0 \to J/\psi K^+K^-$ mode. So far the penguin pollution is measured to be negligible and therefore any deviation from $-2\beta_s$ in the value of ${\phi_s}^{\rm exp}$ will be interpreted as contribution from NP.

1.5.4 Angular- and time- dependent decay rate

Taking into account the four contributing amplitudes, the time-angular-dependent decay rate for a B_s^0 meson is given by a sum of ten terms, corresponding to the four squared polarisation amplitudes and their interference terms

$$\frac{d^4\Gamma\left(B_s^0(t) \to J/\psi K^+K^-\right)}{dt\, d\theta_\mu\, d\theta_K\, d\phi_h} \propto \sum_{k=1}^{10} h_k(t|B_s^0) f_k(\theta_\mu, \theta_K, \phi_h)\,, \tag{1.18}$$

$$\frac{d^4\Gamma\left(\overline{B}_s^0(t) \to J/\psi K^+K^-\right)}{dt\, d\theta_\mu\, d\theta_K\, d\phi_h} \propto \sum_{k=1}^{10} h_k(t|\overline{B}_s^0) f_k(\theta_\mu, \theta_K, \phi_h)\,, \tag{1.19}$$

where functions $h_k(t|B_s^0)$, $h_k(t|\overline{B}_s^0)$ and $f_k(\theta_\mu, \theta_K, \phi_h)$ for $k = 1-10$ are derived in reference [31] and are given in table 1.1. The expressions of the ten functions $h_k(t|\overline{B}_s^0)$ are given below. The time evolution functions $h_k(t|\overline{B}_s^0)$ are obtained by reversing the sign of each term proportional to $\sin(\Delta m_s t)$ or $\cos(\Delta m_s t)$ in $h_k(t|\overline{B}_s^0)$.

$$
\begin{aligned}
|A_0(t)|^2 &= |A_0|^2 e^{-\Gamma_s t}\Big[\cosh\frac{\Delta\Gamma_s t}{2} - \cos\phi_s \sinh\frac{\Delta\Gamma_s t}{2} + \sin\phi_s \sin(\Delta m_s t)\Big], \\
|A_\parallel(t)|^2 &= |A_\parallel|^2 e^{-\Gamma_s t}\Big[\cosh\frac{\Delta\Gamma_s t}{2} - \cos\phi_s \sinh\frac{\Delta\Gamma_s t}{2} + \sin\phi_s \sin(\Delta m_s t)\Big], \\
|A_\perp(t)|^2 &= |A_\perp|^2 e^{-\Gamma_s t}\Big[\cosh\frac{\Delta\Gamma_s t}{2} + \cos\phi_s \sinh\frac{\Delta\Gamma_s t}{2} - \sin\phi_s \sin(\Delta m_s t)\Big], \\
\Im\{A_\parallel^*(t)A_\perp(t)\} &= |A_\parallel||A_\perp| e^{-\Gamma_s t}\Big[-\cos(\delta_\perp - \delta_\parallel)\sin\phi_s \sinh\frac{\Delta\Gamma_s t}{2} \\
&\quad + \sin(\delta_\perp - \delta_\parallel)\cos(\Delta m_s t) - \cos(\delta_\perp - \delta_\parallel)\cos\phi_s \sin(\Delta m_s t)\Big], \\
\Re\{A_0^*(t)A_\parallel(t)\} &= |A_0||A_\parallel| e^{-\Gamma_s t}\cos(\delta_\parallel - \delta_0)\Big[\cosh\frac{\Delta\Gamma_s t}{2} - \cos\phi_s \sinh\frac{\Delta\Gamma_s t}{2} \\
&\quad + \sin\phi_s \sin(\Delta m_s t)\Big], \\
\Im\{A_0^*(t)A_\perp(t)\} &= |A_0||A_\perp| e^{-\Gamma_s t}\Big[-\cos(\delta_\perp - \delta_0)\sin\phi_s \sinh\frac{\Delta\Gamma_s t}{2} \\
&\quad + \sin(\delta_\perp - \delta_0)\cos(\Delta m_s t) - \cos(\delta_\perp - \delta_0)\cos\phi_s \sin(\Delta m_s t)\Big], \\
|A_S(t)|^2 &= |A_S|^2 e^{-\Gamma_s t}\Big[\cosh\frac{\Delta\Gamma_s t}{2} + \cos\phi_s \sinh\frac{\Delta\Gamma_s t}{2} - \sin\phi_s \sin(\Delta m_s t)\Big], \\
\Re\{A_S^*(t)A_\parallel(t)\} &= |A_S||A_\parallel| e^{-\Gamma_s t}\Big[-\sin(\delta_\parallel - \delta_S)\sin\phi_s \sinh\frac{\Delta\Gamma_s t}{2} \\
&\quad + \cos(\delta_\parallel - \delta_S)\cos(\Delta m_s t) - \sin(\delta_\parallel - \delta_S)\cos\phi_s \sin(\Delta m_s t)\Big], \\
\Im\{A_S^*(t)A_\perp(t)\} &= |A_S||A_\perp| e^{-\Gamma_s t}\sin(\delta_\perp - \delta_S)\Big[\cosh\frac{\Delta\Gamma_s t}{2} + \cos\phi_s \sinh\frac{\Delta\Gamma_s t}{2} \\
&\quad - \sin\phi_s \sin(\Delta m_s t)\Big], \\
\Re\{A_S^*(t)A_0(t)\} &= |A_S||A_0| e^{-\Gamma_s t}\Big[-\sin(\delta_0 - \delta_S)\sin\phi_s \sinh\frac{\Delta\Gamma_s t}{2} \\
&\quad + \cos(\delta_0 - \delta_S)\cos(\Delta m_s t) - \sin(\delta_0 - \delta_S)\cos\phi_s \sin(\Delta m_s t)\Big].
\end{aligned}
$$

These expressions are derived under assumption that each of the four decay amplitudes is dominated by a single weak phase, therefore a common ϕ_s can be used in order to describe all CP eigenstates. However, some New Physics models can contribute as a polarisation-dependent shift in ϕ_s [32] and therefore an alternative, polarisation-dependent parametrisation is exploited and summarised in subsection 1.5.5.

1.5.5 Polarisation-dependent parametrisation

To fully explore potential NP contributions, an alternative parametrisation is used. The expressions for the coefficients are obtained under the assumption that CP violation can contribute differently for each polarisation of the final state and therefore distinctive CP-violating observables are used for each possible polarisation of the final state,

$\lambda_f = |\lambda_f| e^{-i\phi_s{}^f}, (f = 0, \|, \perp, S)$. Writing down the time-dependent part for an initial B_s^0 ($\overline{B}_s^0$) as

$$h_k(t|B_s^0) = N_k \frac{3}{4\pi} e^{-\Gamma_s t} \left(a_k \cosh\frac{\Delta\Gamma_s t}{2} + b_k \sinh\frac{\Delta\Gamma_s t}{2} + c_k \cos(\Delta m_s t) + d_k \sin(\Delta m_s t) \right), \tag{1.20}$$

$$h_k(t|\overline{B}_s^0) = N_k \frac{3}{4\pi} e^{-\Gamma_s t} \left(a_k \cosh\frac{\Delta\Gamma_s t}{2} + b_k \sinh\frac{\Delta\Gamma_s t}{2} - c_k \cos(\Delta m_s t) - d_k \sin(\Delta m_s t) \right), \tag{1.21}$$

the definition of the polarisation-specific coefficients N_k, a_k, b_k, c_k, d_k and of the angular functions $f_k(\theta_\mu, \theta_K, \phi_h)$ are derived in reference [30] and are given in table 1.2.

Table 1.2: Angular and time-dependent functions in the time and angles dependent differential decay rate, taking into account polarisation dependence. Abbreviations is used to shorten expression for coefficients, namely $c_K = \cos\theta_K$, $s_K = \sin\theta_K$, $c_l \equiv \cos\theta_\mu$, $s_l \equiv \sin\theta_\mu$, $c_\phi \equiv \cos\phi$ and $s_\phi \equiv \sin\phi$.

k	f_k	N_k	a_k	b_k	c_k	d_k
1	$c_K^2 s_l^2$	$\lvert A_0\rvert^2$	$\frac{1}{2}(1+\lvert\lambda_0\rvert^2)$	$-\lvert\lambda_0\rvert\cos({\phi_s}^0)$	$\frac{1}{2}(1-\lvert\lambda_0\rvert^2)$	$\lvert\lambda_0\rvert\sin({\phi_s}^0)$
2	$\frac{1}{2}s_K^2(1-c_\phi^2 s_l^2)$	$\lvert A_\parallel\rvert^2$	$\frac{1}{2}(1+\lvert\lambda_\parallel\rvert^2)$	$-\lvert\lambda_\parallel\rvert\cos({\phi_s}^\parallel)$	$\frac{1}{2}(1-\lvert\lambda_\parallel\rvert^2)$	$\lvert\lambda_\parallel\rvert\sin({\phi_s}^\parallel)$
3	$\frac{1}{2}s_K^2(1-s_\phi^2 s_l^2)$	$\lvert A_\perp\rvert^2$	$\frac{1}{2}(1+\lvert\lambda_\perp\rvert^2)$	$\lvert\lambda_\perp\rvert\cos({\phi_s}^\perp)$	$\frac{1}{2}(1-\lvert\lambda_\perp\rvert^2)$	$-\lvert\lambda_\perp\rvert\sin({\phi_s}^\perp)$
4	$s_K^2 s_l^2 s_\phi c_\phi$	$\lvert A_\perp A_\parallel\rvert$	$\frac{1}{2}\Big[\sin(\delta_\perp-\delta_\parallel)-\lvert\lambda_\perp\lambda_\parallel\rvert$ $\sin(\delta_\perp-\delta_\parallel-{\phi_s}^\perp+{\phi_s}^\parallel)\Big]$	$\frac{1}{2}\Big[\lvert\lambda_\perp\rvert\sin(\delta_\perp-\delta_\parallel-{\phi_s}^\perp)$ $+\lvert\lambda_\parallel\rvert\sin(\delta_\parallel-\delta_\perp-{\phi_s}^\parallel)\Big]$	$\frac{1}{2}\Big[\sin(\delta_\perp-\delta_\parallel)+\lvert\lambda_\perp\lambda_\parallel\rvert$ $\sin(\delta_\perp-\delta_\parallel-{\phi_s}^\perp+{\phi_s}^\parallel)\Big]$	$-\frac{1}{2}\Big[\lvert\lambda_\perp\rvert\cos(\delta_\perp-\delta_\parallel-{\phi_s}^\perp)$ $+\lvert\lambda_\parallel\rvert\cos(\delta_\parallel-\delta_\perp-{\phi_s}^\parallel)\Big]$
5	$\sqrt{2}s_K c_K s_l c_l c_\phi$	$\lvert A_0 A_\parallel\rvert$	$\frac{1}{2}\Big[\cos(\delta_0-\delta_\parallel)+\lvert\lambda_0\lambda_\parallel\rvert$ $\cos(\delta_0-\delta_\parallel-{\phi_s}^0+{\phi_s}^\parallel)\Big]$	$-\frac{1}{2}\Big[\lvert\lambda_0\rvert\cos(\delta_0-\delta_\parallel-{\phi_s}^0)$ $+\lvert\lambda_\parallel\rvert\cos(\delta_\parallel-\delta_0-{\phi_s}^\parallel)\Big]$	$\frac{1}{2}\Big[\cos(\delta_0-\delta_\parallel)-\lvert\lambda_0\lambda_\parallel\rvert$ $\cos(\delta_0-\delta_\parallel-{\phi_s}^0+{\phi_s}^\parallel)\Big]$	$-\frac{1}{2}\Big[\lvert\lambda_0\rvert\sin(\delta_0-\delta_\parallel-{\phi_s}^0)$ $+\lvert\lambda_\parallel\rvert\sin(\delta_\parallel-\delta_0-{\phi_s}^\parallel)\Big]$
6	$-\sqrt{2}s_K c_K s_l c_l s_\phi$	$\lvert A_0 A_\perp\rvert$	$-\frac{1}{2}\Big[\sin(\delta_0-\delta_\perp)-\lvert\lambda_0\lambda_\perp\rvert$ $\sin(\delta_0-\delta_\perp-{\phi_s}^0+{\phi_s}^\perp)\Big]$	$\frac{1}{2}\Big[\lvert\lambda_0\rvert\sin(\delta_0-\delta_\perp-{\phi_s}^0)$ $+\lvert\lambda_\perp\rvert\sin(\delta_\perp-\delta_0-{\phi_s}^\perp)\Big]$	$-\frac{1}{2}\Big[\sin(\delta_0-\delta_\perp)+\lvert\lambda_0\lambda_\perp\rvert$ $\sin(\delta_0-\delta_\perp-{\phi_s}^0+{\phi_s}^\perp)\Big]$	$-\frac{1}{2}\Big[\lvert\lambda_0\rvert\cos(\delta_0-\delta_\perp-{\phi_s}^0)$ $+\lvert\lambda_\perp\rvert\cos(\delta_\perp-\delta_0-{\phi_s}^\perp)\Big]$
7	$\frac{1}{3}s_l^2$	$\lvert A_S\rvert^2$	$\frac{1}{2}(1+\lvert\lambda_S\rvert^2)$	$\lvert\lambda_S\rvert\cos({\phi_s}^S)$	$\frac{1}{2}(1-\lvert\lambda_S\rvert^2)$	$-\lvert\lambda_S\rvert\sin({\phi_s}^S)$
8	$\frac{2}{\sqrt{6}}s_K s_l c_l c_\phi$	$\lvert A_S A_\parallel\rvert$	$\frac{1}{2}\Big[\cos(\delta_S-\delta_\parallel)-\lvert\lambda_S\lambda_\parallel\rvert$ $\cos(\delta_S-\delta_\parallel-{\phi_s}^S+{\phi_s}^\parallel)\Big]$	$\frac{1}{2}\Big[\lvert\lambda_S\rvert\cos(\delta_S-\delta_\parallel-{\phi_s}^S)$ $-\lvert\lambda_\parallel\rvert\cos(\delta_\parallel-\delta_S-{\phi_s}^\parallel)\Big]$	$\frac{1}{2}\Big[\cos(\delta_S-\delta_\parallel)+\lvert\lambda_S\lambda_\parallel\rvert$ $\cos(\delta_S-\delta_\parallel-{\phi_s}^S+{\phi_s}^\parallel)\Big]$	$\frac{1}{2}\Big[\lvert\lambda_S\rvert\sin(\delta_S-\delta_\parallel-{\phi_s}^S)$ $-\lvert\lambda_\parallel\rvert\sin(\delta_\parallel-\delta_S-{\phi_s}^\parallel)\Big]$
9	$-\frac{2}{\sqrt{6}}s_K s_l c_l s_\phi$	$\lvert A_S A_\perp\rvert$	$-\frac{1}{2}\Big[\sin(\delta_S-\delta_\perp)+\lvert\lambda_S\lambda_\perp\rvert$ $\sin(\delta_S-\delta_\perp-{\phi_s}^S+{\phi_s}^\perp)\Big]$	$-\frac{1}{2}\Big[\lvert\lambda_S\rvert\sin(\delta_S-\delta_\perp-{\phi_s}^S)$ $-\lvert\lambda_\perp\rvert\sin(\delta_\perp-\delta_S-{\phi_s}^\perp)\Big]$	$-\frac{1}{2}\Big[\sin(\delta_S-\delta_\perp)-\lvert\lambda_S\lambda_\perp\rvert$ $\sin(\delta_S-\delta_\perp-{\phi_s}^S+{\phi_s}^\perp)\Big]$	$-\frac{1}{2}\Big[-\lvert\lambda_S\rvert\cos(\delta_S-\delta_\perp-{\phi_s}^S)$ $+\lvert\lambda_\perp\rvert\cos(\delta_\perp-\delta_S-{\phi_s}^\perp)\Big]$
10	$\frac{2}{\sqrt{3}}c_K s_l^2$	$\lvert A_S A_0\rvert$	$\frac{1}{2}\Big[\cos(\delta_S-\delta_0)-\lvert\lambda_S\lambda_0\rvert$ $\cos(\delta_S-\delta_0-{\phi_s}^S+{\phi_s}^0)\Big]$	$\frac{1}{2}\Big[\lvert\lambda_S\rvert\cos(\delta_S-\delta_0-{\phi_s}^S)$ $-\lvert\lambda_0\rvert\cos(\delta_0-\delta_S-{\phi_s}^0)\Big]$	$\frac{1}{2}\Big[\cos(\delta_S-\delta_0)+\lvert\lambda_S\lambda_0\rvert$ $\cos(\delta_S-\delta_0-{\phi_s}^S+{\phi_s}^0)\Big]$	$\frac{1}{2}\Big[\lvert\lambda_S\rvert\sin(\delta_S-\delta_0-{\phi_s}^S)$ $-\lvert\lambda_0\rvert\sin(\delta_0-\delta_S-{\phi_s}^0)\Big]$

Chapter 2

The LHCb detector

The LHCb detector [10] at the LHC [11] at CERN, Geneva, is a general-purpose detector in the forward region, covering the pseudorapidity range $2 < \eta < 5$. The scheme of the detector, with the names of its sub-detectors specified, is shown in figure 2.1. The original motivation of the LHCb experiment, as follows from its name, is the study of the particles containing b quarks. The physics program however is much broader and includes, amongst others, the study of charm-quark systems, the search for exotic unknown particles, spectroscopy measurements, as well as heavy-ion collisions, electroweak boson production and even Higgs decays.

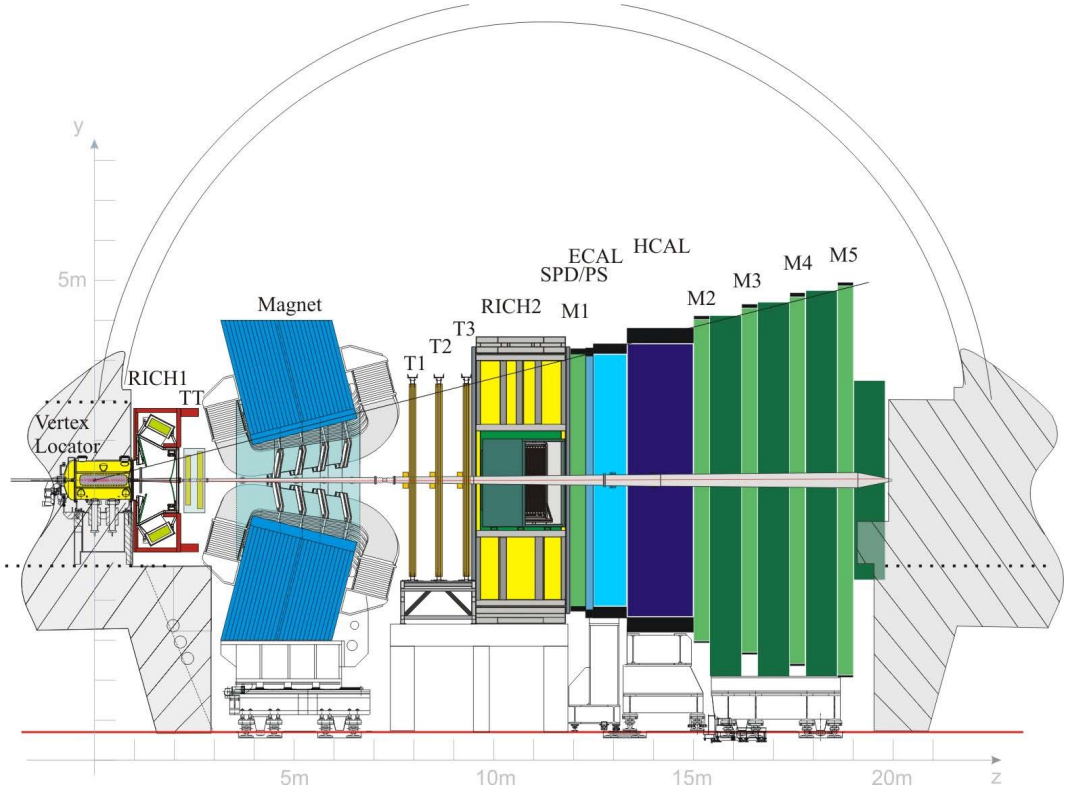

Figure 2.1: Scheme of the LHCb detector [33].

The layout of the detector is shown in figure 2.2. Overlaid is an example of a $B_s^0 \to J/\psi K^+ K^-$ decay (particles are shown schematically, not to scale), starting with a B_s^0 meson that is produced in the proton-proton collision.

2.1 Vertexing

The interaction region is surrounded with a high-precision silicon micro-strip tracking system, the VErtex LOcator [34]. B_s^0 mesons fly on average a distance of approximately 1 cm in the VELO before decaying and forming a so-called secondary vertex. By determining the trajectories from the signals that charged particles generate as they traverse the VELO detector, primary and secondary vertices are identified. The presence of the secondary vertex in an event is an important feature used in the high level trigger, which reduces its input event rate of 1 MHz to just a few kHz. Although the LHCb detector only measures particle's momenta in the forward region, the VELO sub-detector reconstructs tracks in the backward region as well, in order to improve the resolution on the reconstructed primary vertices. During its lifetime, the B_s^0 meson may oscillate to its anti-particle, the $\overline{B}_s^0$ meson with an oscillation frequency measured to be $17.757 \pm 0.021\,\mathrm{ps}^{-1}$ [7]. The oscillations obtained using the $B_s^0 \to D_s^- \pi^+$ sample introduced in section 4.5 are shown in figure 2.3. In order to perform CP-violation measurements, these oscillations have to be resolved. This imposes strong constraints

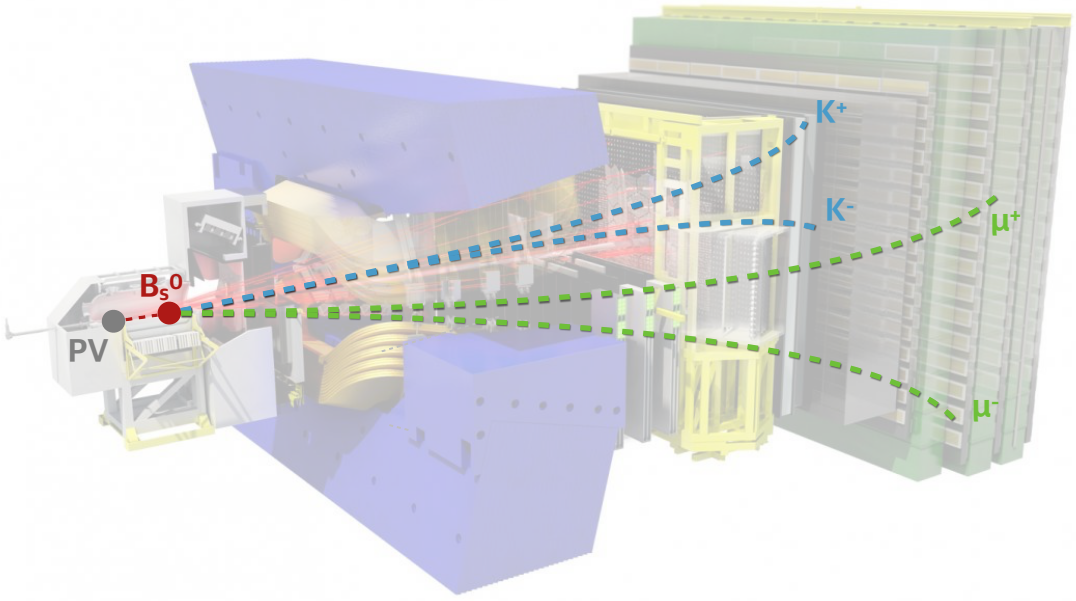

Figure 2.2: Scheme of the LHCb detector with tracks from $B_s^0 \to J/\psi K^+ K^-$ overlaid.

on the design of the VELO sub-detector. The average decay-time resolution achieved with the VELO detector for the $B_s^0 \to J/\psi K^+K^-$ decay mode is 45 fs. The dependence of the decay time resolution as a function of the B_s^0 momentum and as a function of the estimated decay time error is shown in figure 2.4.

2.2 Particle identification

Both J/ψ and ϕ mesons are resonances which decay without traveling significant distances. The J/ψ meson is reconstructed using the $J/\psi \to \mu^+\mu^-$ decay mode. The ϕ resonance is reconstructed using the $\phi \to K^+K^-$ decay mode. These four daughter particles travel trough the rest of the detector, traversing the first of the two ring-imaging Cherenkov (RICH1) [36] sub-detectors where charged particles will (most likely) emit Cherenkov light. When a particle travels through the gas inside the RICH sub-detectors (C_4F_{10} in RICH1 and CF_4 in RICH2) with a speed which is faster than the speed of light in that medium, it will emit a cone of light. The measurement of the particle velocity from the opening angle of that cone, or Cherenkov angle, is combined with momentum measurement to determine the mass and therefore establish the identity of the particle. The method is used predominantly to distinguish between muons, kaons, protons and pions. The RICH1 sub-detector is used to identify particles in the momentum region of $2 - 40\,\text{GeV}/c$. The RICH2 [36] sub-detector, situated upstream, provides particle identification (PID) for charged hadrons with a momentum in the range of $15 - 100\,\text{GeV}/c$. Without the PID determination of the RICH many measurements of CP violation would not be possible due to the large contamination

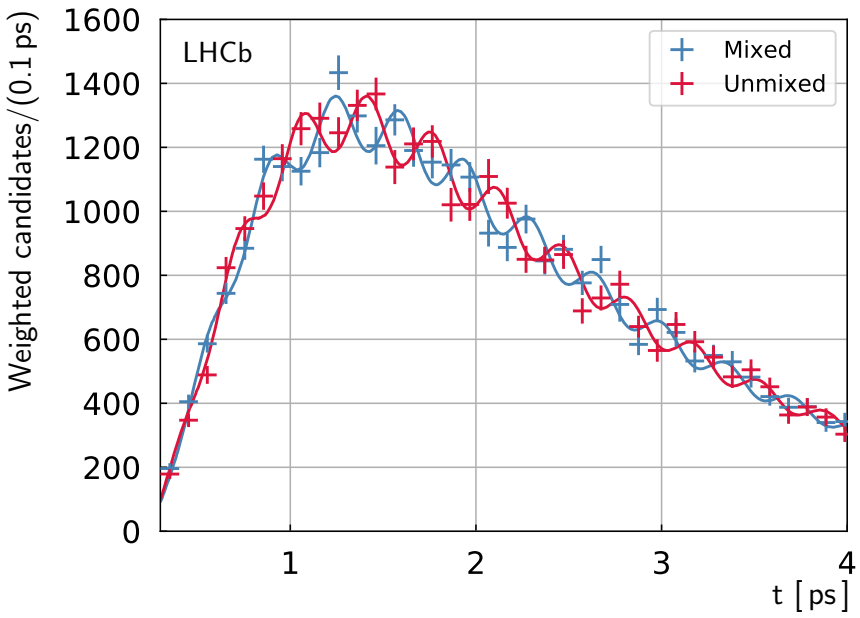

Figure 2.3: Distribution of the decay time for $B_s^0 \to D_s^-\pi^+$ background-subtracted signal tagged as mixed and unmixed with the projection of the fit result.

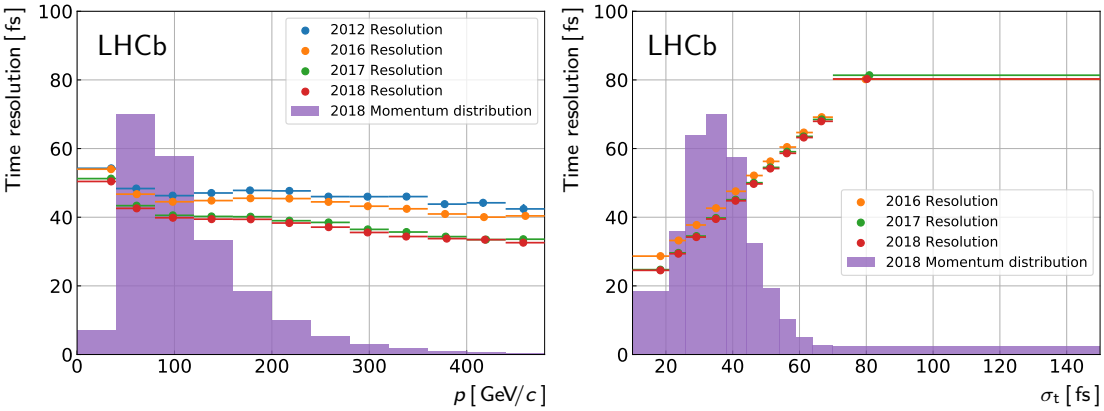

Figure 2.4: Comparison of the resolution for the B_s^0 decay time in $B_s^0 \to J/\psi\phi$ decay between different years. Left as a function of B_s^0 momentum and right as a function of estimated decay time error [35].

from the background. Kaons from the fragmentation of b quarks in the B_s^0 meson creation are used in the identification of its initial flavour. Those kaons usually have a low momentum, around 10 GeV/c and PID for hadrons with momentum down to few GeV/c significantly increases the tagging power of the experiment which is in turn essential for measurements of CP violation.

2.3 Tracking

After RICH1 particles pass through the first out of the four tracking stations of the LHCb tracking system [37], the Tracker Turicensis, TT [38]. After TT, the trajectories of the charged particles are bent in the dipole magnet [39] with a bending power of about 4 Tm. Beyond the magnet, particles pass through the remaining three tracking stations (T1–T3). Two different technologies are used due to the different occupancy level and the different sized areas they must cover. Silicon detectors allow for a very fine spatial resolution and are used downstream and upstream in the region close to the beam pipe, where the particle density is high. Both close to the beam pipe, the Inner Tracker (IT) [38] and the TT tracker are silicon micro-strip detectors, while the Outer Tracker (OT) [40, 41] uses straw-tube drift chambers. The tracking system of the LHCb detector is used to reconstruct the trajectories of the charged particles and since these trajectories are bent by the magnet their momentum can be determined from the curvature of the trajectory. Having a good momentum resolution is required for precise determination of the invariant mass of the B candidates, which in turn allows to better separate signal from background. The tracking system of the LHCb detector is used to measure momentum with a relative uncertainty from 0.5 % to 1 % for momenta up to 200 GeV/c, which results in an invariant-mass resolution for $J/\psi K^+K^-$ of around 8 MeV/c^2.

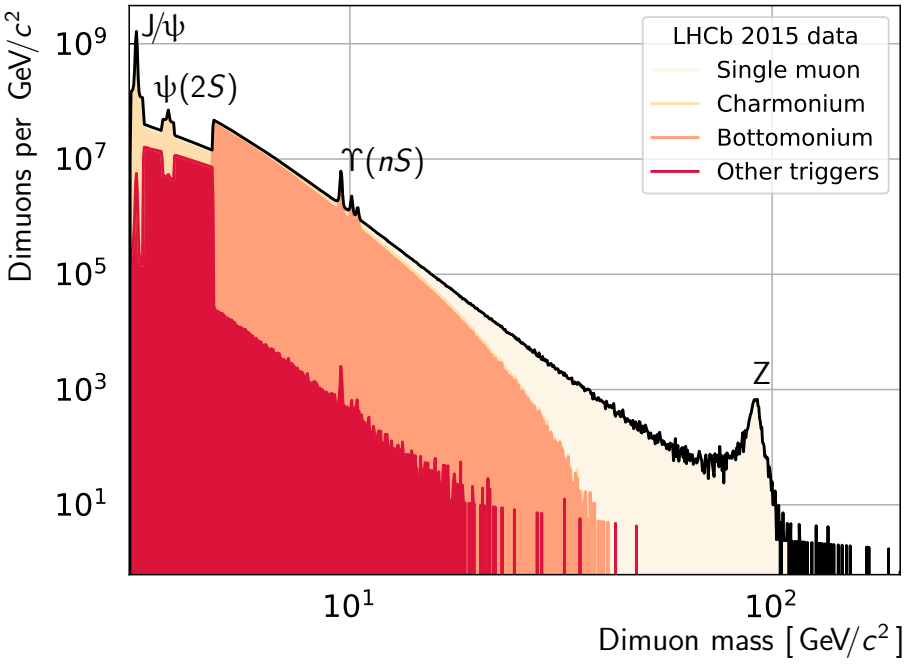

Figure 2.5: Dimuon mass distribution in 3–200 GeV/c^2 range [42], obtained directly from the trigger.

2.4 Calorimeter

After passing through the OT and RICH2, K^+ and K^- from ϕ meson decay are stopped in the calorimeter system [43]. The calorimeter system of the LHCb detector is composed of a scintillator pad detector, a preshower detector, an electromagnetic calorimeter and a hadronic calorimeter. It serves two main purposes: one is to measure neutral particles energy and to provide additional information for the particle identification and the other is to provide information to the hardware trigger [44].

2.5 Muon system

Muons, such as those originating from J/ψ decays, continue travelling through the detector to the muon system [45, 46]. The muon detector is composed of one station situated before the calorimeter system (M1) and four stations situated downstream (M2–M5) interleaved with 80 cm thick iron absorbers. Each station is of rectangular shape and is equipped with multi-wire proportional chambers. The information on the muon's hits in the muon detector combined with the beam spot location provides an estimation of the track p_T, which is used in the hardware trigger. The M1 station improves the resolution on the estimated transverse momentum from around 35% to around 25%, with respect to using only M2–M5 stations. At a later stage, the muon track segments in the muon system are combined with the information from the whole detector. The identification of muons provides high (around 90 %) trigger

efficiencies for the dimuon channels, such as $B_s^0 \to J/\psi K^+ K^-$ decay. The observed dimuon spectrum in the LHCb experiment is shown in figure 2.5.

2.6 Trigger system

A crucial part of the detector is its trigger system [47], which consists of a hardware stage, `L0`, based on information from the calorimeter and muon systems, followed by a software stage, `Hlt`, which applies a full event reconstruction. The detailed description of the system is given in section 3.

2.7 Data sample and simulation

The analysis is performed using proton-proton collision data collected by the LHCb detector at 13 TeV in 2015 and 2016, which corresponds to 0.3 and 1.6 fb^{-1}. In order to properly model the effects of the detector acceptance and of the selection requirements, a detailed simulation of the LHCb detector is used. In the simulation PYTHIA [48], with a specific LHCb configuration [49], is used to generate pp collisions. Decays of unstable particles are described by EVTGEN [50], in which final-state radiation is generated using PHOTOS [51]. The interaction of the generated particles with the detector, and its response, are implemented using the GEANT4 toolkit [52] as described in reference [53].

Chapter 3

Trigger

This chapter is dedicated to the trigger system of the LHCb experiment and its upgrade. The information presented is based on the four following publications, where the author of this thesis is one of the co-authors. "Design and performance of the LHCb trigger and full real-time reconstruction in Run 2 of the LHC" [54], "A comprehensive real-time analysis model at the LHCb experiment" [55], "Upgrade trigger selection studies" [56] and "A new scheduling algorithm for the LHCb upgrade trigger application" [57]. Some excerpts from the listed publications are presented below.

The LHC provides proton-proton collisions at a rate of 30 MHz, while the limited online and offline computing resources of the LHCb experiment allow to store data delivered at a rate of only about ten kHz. Therefore the input rate has to be reduced by a factor of thousand. A trigger system is employed in order to fit the bandwidth of the detector into the available computing resources, where bandwidth is defined as

$$\text{Bandwidth}\,[\text{MB/s}] = \text{Output rate}\,[\text{kHz}] \times \text{Event size}\,[\text{kB}]. \tag{3.1}$$

Bandwidth reduction can be done by lowering the output rate, i.e. rejecting more events, and by reducing the event size. In the following text the implementation of the second option in the trigger system of the LHCb experiment is discussed in detail.

The schemes for both Run 1 and Run 2 triggers of the LHCb experiment are shown in figure 3.1. Both consist of three stages: a hardware (`L0`) trigger which uses a fraction of the information from the calorimeter, muon, and pile-up systems and selects events at a maximum rate of 1 MHz to be transmitted from the detector; followed by a software (`Hlt1`) trigger which has access to information from all sub-detectors and which reduces the input rate to around 150 kHz. In Run 2 the output of `Hlt1` was buffered to disk storage in the online system where alignment and calibration of the detector are performed. A second step of the software trigger (`Hlt2`) runs asynchronously on events selected by `Hlt1` and performs the final selection of events reconstructed using the full alignment (also used by `Hlt1`), calibration, and detector reconstruction. The output rate of `Hlt2` is of around 12.5 kHz. If an event passes through all the trigger stages it is then persisted in long-term storage for further offline analysis.

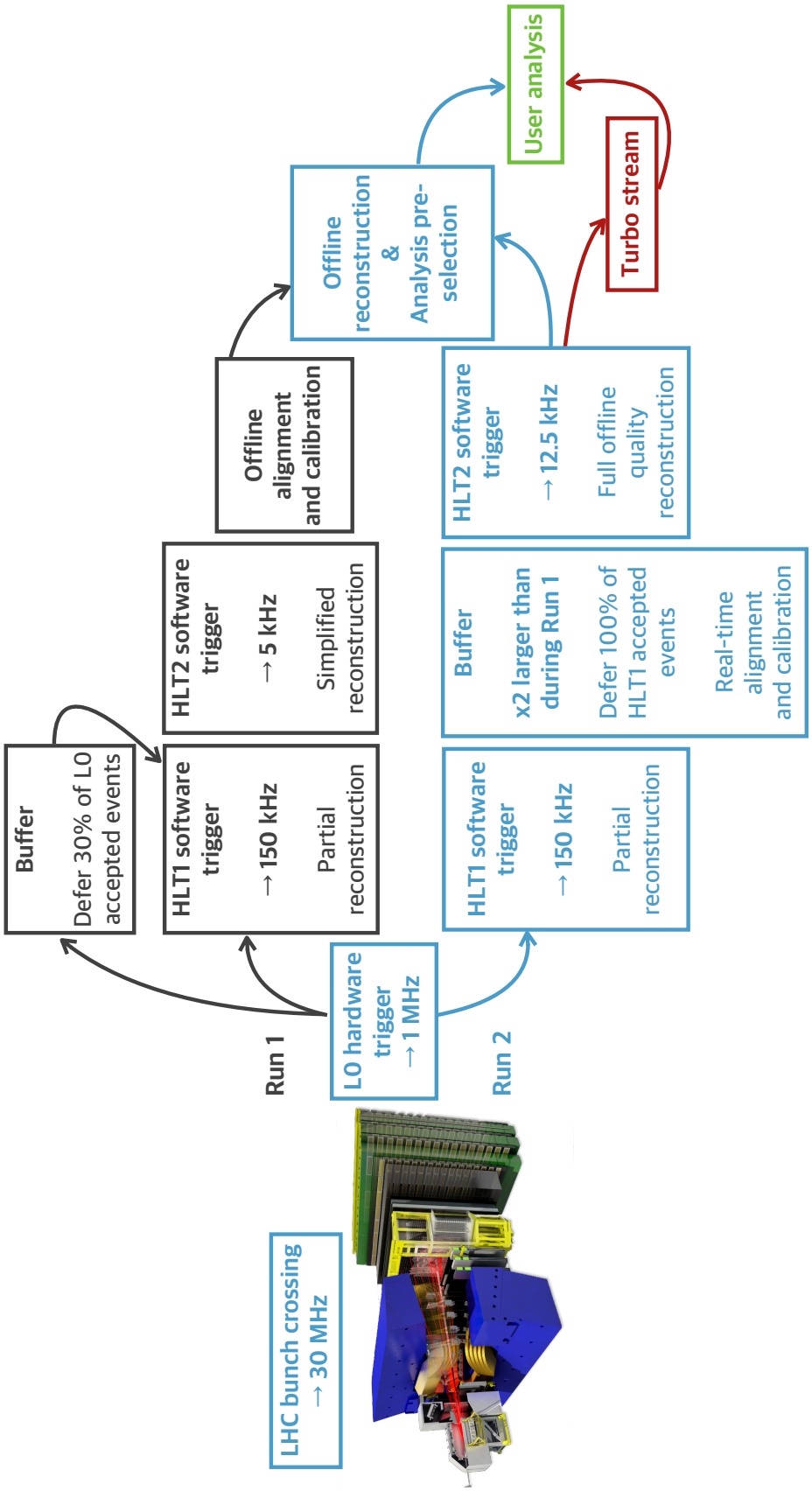

Figure 3.1: Scheme of data flow in the trigger system of the LHCb detector in Run 1 and Run 2. The diagram is adapted from poster [58].

Each of the three trigger stages consists of chains of algorithms, and depending upon their output, the decision is made whether an event is discarded or selected for the following stage of processing. According to the convention adopted in the LHCb experiment, a single trigger decision chain is referred to as a "line" and the trigger consists of a set of a trigger lines. The decision of each individual line is based on different criteria, with potentially some overlap, but logically independent and self-contained.

The disk space required to store the trigger output is estimated by integrating the output bandwidth over a given data-taking period. The permanent storage of the LHCb experiment has a limited capacity and therefore events that are to be persisted have to be carefully selected. By minimizing the event size one can effectively record more interesting events while keeping the bandwidth constant. In Run 1 the reduction of event size was not possible, because all events were written to permanent storage in a fixed so-called "raw" event format. A raw event consists of responses from all the sub-detectors. This type of persistency is referred to as "full stream". Offline, particle information is reconstructed from this "raw" event using calibration and alignment constants that are also calculated offline. The size for each raw event is approximately 70 kB.

In Run 2, two main new features were introduced: the size of the buffer was increased to 10 Pbytes and it was explicitly positioned between `Hlt1` and `Hlt2` as shown in figure 3.1, allowing for alignment and calibration to be provided in real time. From reference [54] " 'real time' is defined as the interval between a collision occurring and the point at which the corresponding event must be either discarded or sent offline for permanent storage". The addition of a disk buffer allows to perform computations to be postponed until periods when no data is accumulated. The size of the buffer extends 'real time' up to two weeks during nominal data-taking [54] which provides more than enough time to run alignment and calibration algorithms on the data stored in the buffer. As a result, the now identical performance of the online and offline reconstruction allows to persist event information in a reduced format, containing only information related to the reconstructed physics objects which passed the relevant set of trigger selections, as well as some event summary information, instead of persisting the full raw event. Performing full physics selections in real time in the trigger without a loss of precision provides a maximal reduction in persisted event size. This approach of data-persistency is called `Turbo` [59].

The `Turbo` model was first introduced in the LHCb trigger in 2015 for some fraction of the triggered events and has evolved considerably since then. The initial `Turbo` persistency model was suitable for exclusive selections where the full decay is completely specified, and no additional information is needed to perform the analysis. In this model, the objects that are saved for a given trigger line are [55]

- the set of all tracks and neutral objects, calorimeter and PID information relating to those objects, and decay vertices that form the trigger candidate;
- the tracking detector information associated to the candidate tracks;
- all of the reconstructed Primary Vertices (PVs) in the event.

Other reconstructed objects in the event, including the raw event, are discarded (except for the first year of when the model was implemented, when the raw event was preserved as well, to verify the correct implementation of the Turbo model). The typical event size in the Turbo model is ten times smaller than the raw event size. Therefore one can increase the number of events while keeping the bandwidth constant, extending the physics reach of the experiment by better exploiting the limited computational resources.

The Turbo model allowed the first LHCb Run 2 measurements to be presented 18 days after the data was collected [60, 61]. The introduction of the Turbo persistency model was originally driven by the desire to keep a rich charm physics program in Run 2. Since the charm production rate is 25 times larger that that for beauty [62, 63], only the reduced format allowed to select the high rate of charm triggers.

In Run 3 (2021–2024) the instantaneous luminosity delivered to the LHCb detector will be increased by a factor of 5, to $2 \times 10^{33}\,\mathrm{cm}^{-2}\,\mathrm{s}^{-1}$. The raw event size for the upgraded LHCb detector will grow as well, and therefore the reduced format persistency model has to become the default one. To be able to use Turbo for more physics measurements, it was extended to allow additional flexibility for defining which objects are to be persisted. In order to extend the usage of the Turbo model to inclusive selections and to analyses in which additional information in the event may be required at a later stage (such as performing flavour tagging or isolation studies), the Turbo++ model was introduced. In this model, the complete event reconstruction performed in Hlt2 can be persisted in addition to the object(s) responsible for a trigger decision. This model was successfully implemented and used. Even though Turbo++, as well as the Turbo model, allows for significant reduction of the CPU usage due to the fact that the reconstruction step performed offline is skipped, the combined size of all reconstructed objects is close to the size of a raw event, while typically only a small part of reconstructed objects is actually used. To allow for more flexibility, a more advanced reduced persistency model is introduced and explained in section 3.1.

3.1 Trigger in Run 2: TurboSP

To allow for a better flexibility, a compromise between Turbo and Turbo++ is introduced: TurboSP, where SP stands for Selective Persistence. With TurboSP it can be specified explicitly which information to store, whether it is reconstructed or raw, in addition to the trigger candidate itself. This permits a significant event size reduction with respect to Turbo++. The TurboSP persistency model was implemented in the LHCb trigger at the beginning of 2017.

The trigger framework was modified to enable users to specify extra algorithms. The trigger lines are then expanded with those additional selection algorithms, that are executed after the trigger decision for the given trigger line has been determined. This additional selection is not limited to the objects related to the trigger candidate.

A comparison between different types of Turbo persistency models together with the resulting event sizes is done using, as example, the $B_s^0 \to J/\psi K^+ K^-$ decay, as shown in figure 3.2. With Turbo, only objects specified in section 3 are kept, while in case of

Turbo++, the whole underlying reconstructed event will be stored. TurboSP on the other hand allows for much more flexibility, for instance if it desired to determine the flavour of the signal B_s^0 meson, the information used by flavour tagging algorithm (in the given example it is $B^+ \to J/\psi K^+$ candidate) can be added as an extra algorithm to the trigger line that selects on the $B_s^0 \to J/\psi K^+ K^-$ decay signature. The selection framework allows a user to specify additional requirements to be made on both extra information that is to be persisted. Similar selections can be added at the same time for other extra particles, such as kaons, photons, and hyperons to support a wide spectrum of charm spectroscopy measurements all based upon a single trigger selection.

Selective persistence is a key ingredient in the migration of the physics programme in preparation to Run 3 to the real-time analysis model [64]. A commonly used extra algorithm selects objects required to run the flavour-tagging algorithms that are used to determinate the initial flavour of a (anti-)beauty meson. Since the performance of the flavour tagging is constantly being improved, it is important to be able to re-run them during the offline analysis. The decision of one or more tagging algorithms, together with the probability of the assigned flavour being wrong, is computed using a set of reconstructed objects in the event related to the same PV as the signal decay. The set of reconstructed objects required as input to the tagging algorithms constitute only around 10 % of the space that would otherwise be required for persisting the full reconstruction.

By the end of Run 2, the number of trigger lines that are using one of the Turbo persistency models was around half of the number using the traditional model, however the output bandwidth for Turbo was only 25 % of the full stream thanks to the reduced average event size. Some of the examples of the physics measurements using the Turbo model include charm and J/ψ cross-sections [62, 63], the discovery of new ground-state and excited charm baryons [65, 66], searches for dark photons [67], and the characterisation of charmonium production within jets [68]. The reduced format has been successfully used and tested in the trigger system of the LHCb experiment. It will become the default persistency model for Run 3.

3.2 Trigger in Run 3: Scheduler

Together with the fivefold increase in luminosity in Run 3, the other major change will be the removal of the L0 hardware trigger from the trigger system, as it is no longer capable of providing the necessary signal-to-background separation. Therefore the LHCb experiment is going to operate a trigger-less readout of the full detector, followed by a software trigger. That means that the software trigger will need to process a 30 times larger event rate. Due to constraints on offline storage resources, the output bandwidth is limited to a maximum of 10 Gbytes/s [64]. These strict conditions require a significant optimisation of the trigger framework. One particular task that has to be revisited and optimised is the scheduling of the execution order of algorithms in the trigger. In the Run 1 and Run 2 trigger framework the user needs to define the complete sequence of algorithms in order to define a trigger line. Each algorithm has to have its data inputs explicitly specified and algorithms producing these inputs must

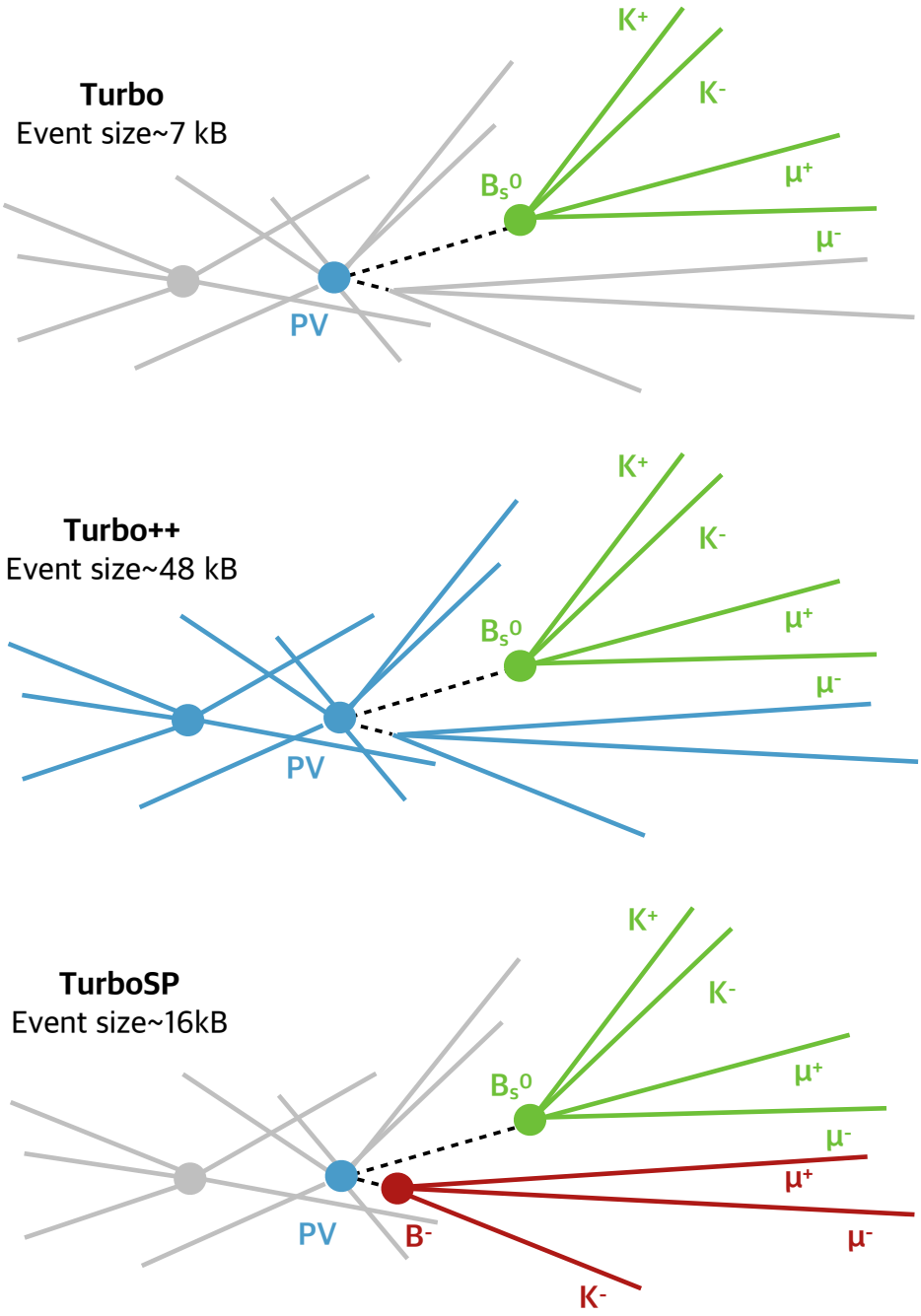

Figure 3.2: An example of which objects are persisted in the different `Turbo` schemes for the same reconstructed event: `Turbo` (top), `Turbo++` (middle) and `TurboSP` (bottom). Colored are objects are those that are persisted in each framework. In grey are the objects that are not kept.

be explicitly configured and executed prior to the consuming algorithm. The control flow is then implied by the explicit ordering and processing status of all algorithms contained in a trigger line.

For the upgrade of the LHCb experiment, an improved scheduling framework is developed. It is designed to give users general building blocks that are well defined, can be executed on multiple cores in parallel and that automatically handle the data flow between algorithms. The basic idea behind the Scheduler is that at initialisation time of the application a static data- and control-flow dependency graph can be generated to schedule algorithms in the right order, matching both the data- and control-flow dependencies.

The Scheduler is based on the concept of nodes, which can be of two general types: basic and composite. A basic, or control-flow, node is a wrapper around a single algorithm, which keeps track of the control-flow and data-dependency information for the given algorithm. Specifically, it determines whether the algorithm needs to be executed, and if so, if it has data dependencies and, if so, whether the producers of these data dependencies have been executed already. Algorithms that provide data are referred to as "data producers". A composite node consists of a set of children nodes, either basic or other composite nodes, and it can be of one of the following types:

- LAZY_AND - stop execution once a child node signals a negative decision
- NON_LAZY_AND - execute all child nodes; the decision of the node is positive only if the decisions of all of its children are positive
- LAZY_OR - stop execution once a child node signals positive decision
- NON_LAZY_OR - execute all child nodes; the decision of the node is positive if the decision of at least one of its children is positive
- NOT - the decision of the node is the opposite of the decision of its child

A trigger line consists of a sequence of algorithms, which are executed until the first decision-making algorithm signals the end of execution. A trigger line can therefore be represented as a composite node of the type LAZY_AND. Decisions of all the trigger lines in the software trigger must be independent of each other and therefore the trigger lines are children of a top level composite NON_LAZY_OR decision node. In case the event is selected by at least one of the trigger lines, it is persisted. To illustrate the work of the Scheduler, consider a simple case in which the trigger consists of just two trigger lines (two LAZY_AND nodes), which are children of the composite decision node (NON_LAZY_OR). Each line consists of three basic nodes: prescaler (P_1, P_2), filter (F_1, F_2) and a global event cut (G) which is shared between the two lines, as shown on the scheme in the figure 3.3.

The Scheduler is used to define the order of algorithms to be executed. The order is determined from the list of all control-flow nodes that is retrieved from the composite nodes, starting with the top node. In the given example the list of basic nodes is [P_1, F_1, G, P_2, F_2]. For ordering purposes the concept of edges is defined, where an edge is a pair of two sets of nodes. Nodes that are in the left set have to be executed before

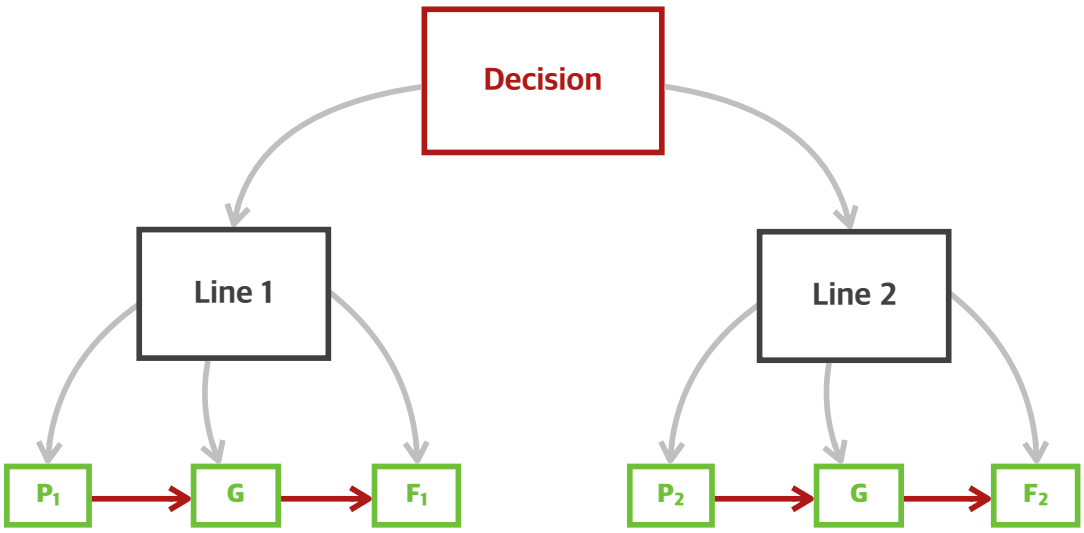

Figure 3.3: Scheme of the trigger in a simple case when the trigger consists of only two trigger lines.

those in the right set. Edges are defined automatically, depending on the type of a chosen composite node. However, the `Scheduler` framework allow users to define any number of additional edges. In the given example the edges have to be specified such that that $\mathtt{P}_1$ ($\mathtt{P}_2$) are executed before `G`, which needs to be executed before $\mathtt{F}_1$ ($\mathtt{F}_2$). This results in the ordering shown in figure 3.4. The flat list of basic nodes is ordered using the list of specified edges. Subsequently, the data dependencies need to be resolved. In the new Run 3 framework each algorithm has to explicitly declare its input(s) and output(s) (or their absence). In order to resolve data dependencies a data "broker" service is introduced. It is configured with all producers and given any direct data dependency, it builds the entire corresponding data-flow dependency graph.

Different trigger lines may include the same data producers, such as reconstruction algorithms, for example a track fit. Even though the tracks required to be fitted by various lines are in principle different, they will overlap in most cases. Algorithms, such as track fit, are "expensive", meaning that they require significant computational resources. Therefore executing these expensive algorithms on the same objects required by different trigger lines is extremely inefficient and time-consuming. To reduce the amount of work the concept of a "barrier" is introduced in the `Scheduler`. The schematic example of the `barrier` is shown in figure 3.5. The `barrier` introduces an additional ordering constraint, such that for the trigger lines registered with the `barrier` their algorithms that are scheduled before the `barrier` will be executed and only then the common work is performed by the `barrier`.

Additional bookkeeping is required to keep track of which subset of the input data belongs to which line. The `barrier` itself is built of three components: `gather`, algorithm and `scatter`. `Gather` is responsible for merging the input data from the trigger lines for the barrier algorithm. The actual reconstruction algorithm is blind

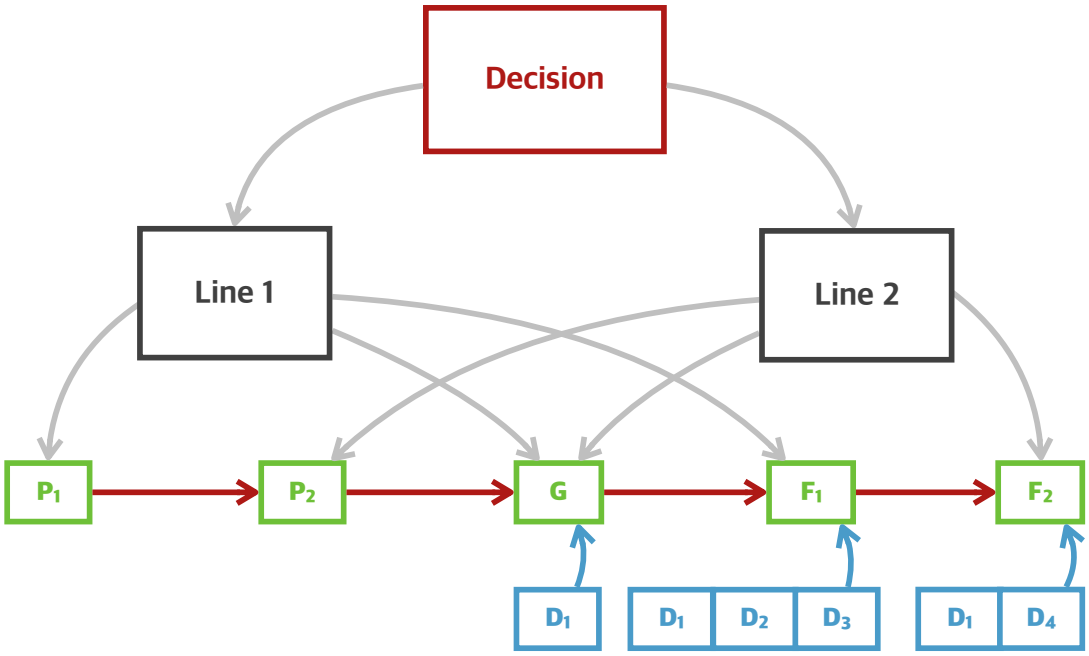

Figure 3.4: Example of the outcome of the ordering procedure for the simple, two-trigger-lines case.

to the barrier concept: the output of it is just one container with the data objects. This container subsequently needs to be split between the trigger lines. The splitting is performed by a dedicated `scatter`. The barrier is the only data dependency that explicitly affects the order of the list of control-flow nodes when the control-flow graph is flattened into the execution sequence. Since the input for the `barrier` is optional, the additional edges from each input to each output of the `barrier` are created to make sure the order of the flattened sequence is correct. After the static execution ordering is determined at initialization time, the second part of the `Scheduler` work is performed at run time. The list of the ordered control flow nodes is being executed; the first step is checking if the node is requested by it parent(s) to be executed. The check is done recursively and the corresponding runtime complexity, e.g. the amount of time it takes to run an algorithm, is up to $O(N_{\text{parents}})$. If a control-flow node is requested, then the producers of the data dependencies of the node are executed (in case they have no yet been executed); the runtime complexity is up to $O(N_{\text{producers}})$. Finally the node itself is executed. After the execution the parent(s) of the node are notified about the execution and its outcome, which implies a runtime complexity of up to $O(N_{\text{parents}})$. In case the node is not requested, it is skipped and the following node in the list is checked.

The general design of the `Scheduler` has been developed and validated using a standalone prototype written in the `Python` programming language. The details about implementation and performance of the actual `Scheduler` algorithm of the upgraded LHCb detector can be found in reference [69].

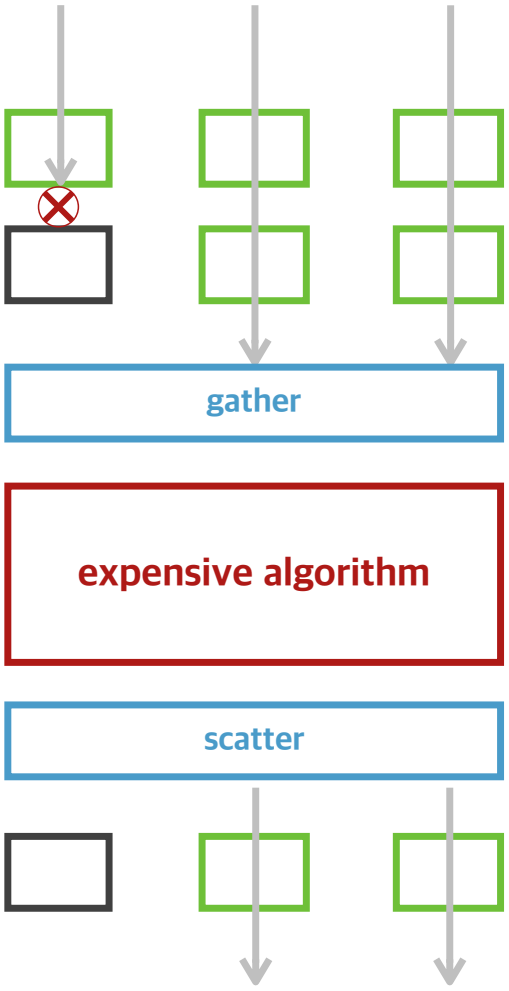

Figure 3.5: Scheme illustrates an example usage of the `barrier`.

3.3 Triggering on $B_s^0 \to J/\psi K^+K^-$ in Run 3

In order to migrate the physics program of LHCb to the new trigger, a study dedicated to the bandwidth division is performed as described in reference [56]. The main purpose of the study is to put together all possible trigger lines and to estimate whether the output of these lines fits into the available bandwidth. The selection criteria have to be adjusted for those lines that do not fit into the allocated bandwidth. The trigger selection and corresponding bandwidth of the $B_s^0 \to J/\psi K^+K^-$ trigger line are estimated using a sample of roughly 50M minimum bias events and signal samples, of approximately 250k events generated according to conditions specified in reference [56].

The trigger line is implemented in the new framework that includes both the `Scheduler` and `TurboSP`. The realistic data- and control- flow graphs obtained in the new framework are shown in figures 3.7 and 3.6, respectively.

The output rate is assessed with the fraction of selected candidates from the trigger

line, while running over the simulated sample. This fraction is multiplied by 30 MHz, the non-empty LHC bunch crossing rate, to get an estimate of the rate. The estimated rate for the $B_s^0 \to J/\psi K^+K^-$ trigger line that is based on the stripping selection criteria introduced in section 4.1 is measured to be 310 Hz.

The expected rate is estimated from the instantaneous luminosity multiplied with the cross-section and the signal efficiency. The instantaneous luminosity expected in Run 3 is $2 \times 10^{33}\,\mathrm{cm}^{-2}\,\mathrm{s}^{-1}$. The expected cross-section for $B_s^0 \to J/\psi K^+K^-$ decay is defined as

$$\sigma(pp \to b\bar{b}X) \times 2 \times B_s^0 \text{ fragmentation fraction} \times \mathcal{B}(B_s^0 \to J/\psi K^+K^-) \times \mathcal{B}(J/\psi \to \mu^+\mu^-)$$

where $\sigma(pp \to b\bar{b}X) = 100\,\mu b$ [62]. The signal efficiency is defined as the fraction of the selected signal events in the sample and is estimated to be 43% for $B_s^0 \to J/\psi K^+K^-$ mode, using the same simulated sample described above. The output rate is therefore expected to be around 2.5 Hz. The large difference between the measured and expected trigger rates for $B_s^0 \to J/\psi K^+K^-$ decay mode is evidence that the selection criteria are quite loose and therefore a large fraction of selected events is background.

As follows from the equation 3.1, the event size is needed to calculate the expected bandwidth. The average event size for the $B_s^0 \to J/\psi K^+K^-$ is found to be around 5 kB when only the triggered candidate is persisted. However, the information required by the flavour tagging is also required in order to be able to re-evaluate the tagging decision offline. Requesting the objects required by the flavour tagging algorithms to be persisted within the `TurboSP` framework, increases the average event size to approximately 15 kB. For comparison, the size of the corresponding, full, underlying raw event is around 230 kB. Using this event size estimate, the bandwidth is expected to be around 4.7 MB/s. Given that an estimated total output bandwidth for `Hlt2` will be between 2 GB/s and 10 GB/s, while number of exclusive selections exceeds 400, the $B_s^0 \to J/\psi K^+K^-$ bandwidth has to be significantly lowered. To lower the bandwidth and simultaneously increase the signal efficiency, an additional study has to be performed to strengthen the selection. There is also a possibility to use multivariate techniques directly in the trigger, as suggested in reference [70].

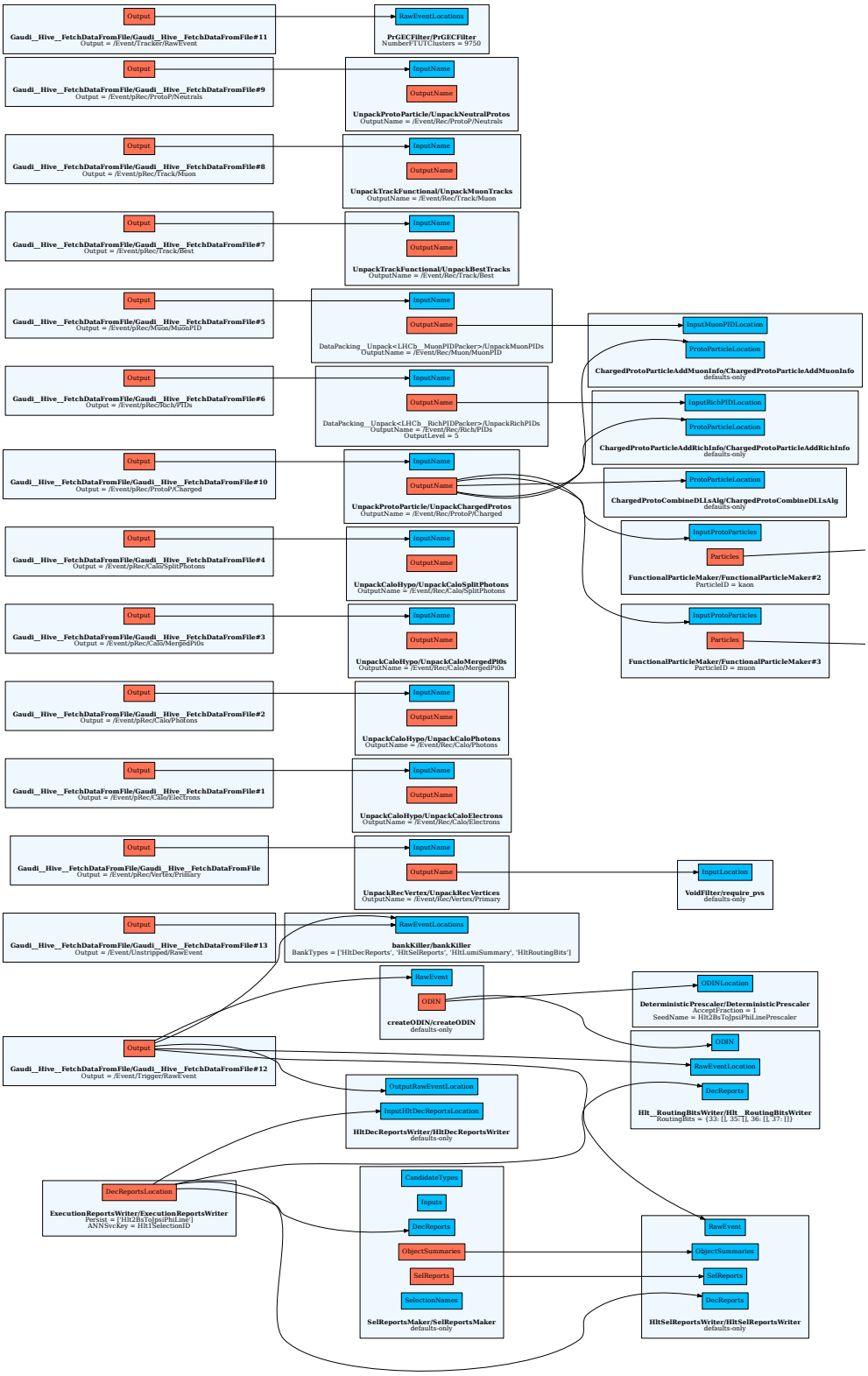

Figure 3.6: First part of the scheme which illustrates the data flow of the real $B_s^0 \rightarrow J/\psi K^+K^-$ trigger line implemented in the new framework.

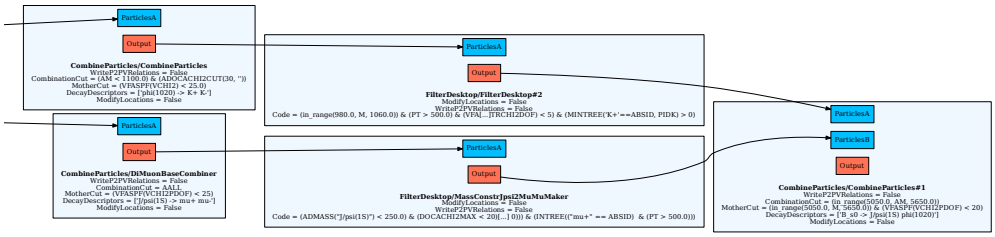

Figure 3.6: Second part of the scheme which illustrates the data flow of the real $B_s^0 \to J/\psi K^+K^-$ trigger line implemented in the new framework.

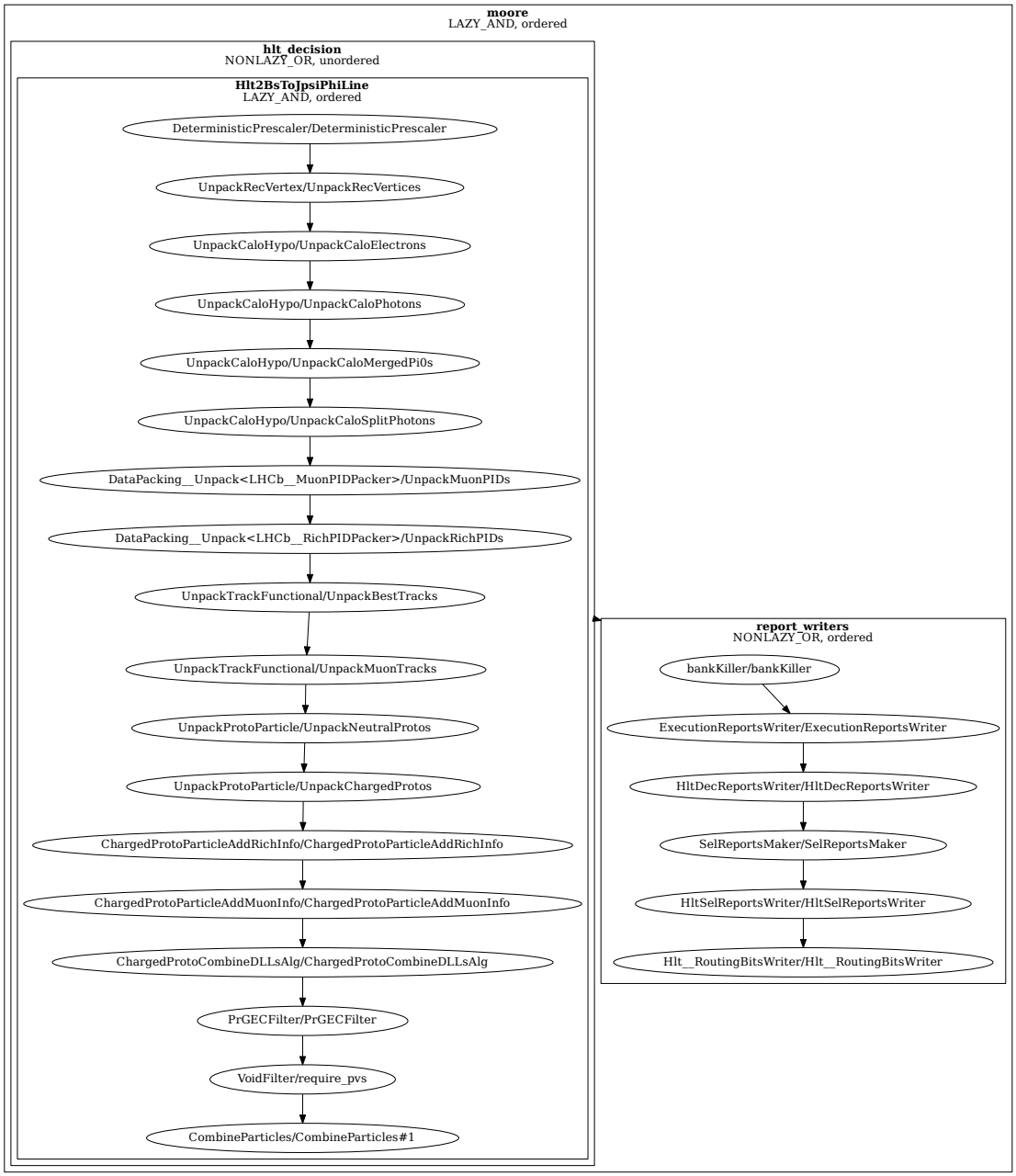

Figure 3.7: This schema illustrates the control flow scheme of the real $B_s^0 \to J/\psi K^+ K^-$ trigger line implemented in the new framework.

Chapter 4

Analysis

To extract the physics parameters of interest an unbinned maximum-likelihood fit is performed to the decay-time (t) and angular (Ω) distributions of the signal candidates. As introduced in reference [71], the likelihood is defined as

$$\mathcal{L}(\theta) = \prod_{i=1}^{n} p(\vec{x};\theta) \tag{4.1}$$

where $\vec{x}$ is a vector of observables, n is the number of measurements and θ is the set of parameters of the PDF $p(\vec{x};\theta)$. The parameter estimators are found by maximizing the likelihood function. Instead of $\mathcal{L}$, its logarithm, the log-likelihood, is used since it translates the product of probability functions in $\mathcal{L}$ into a sum of their logarithms

$$\ln \mathcal{L}(\theta) = \sum_{i=1}^{n} \ln\ p(\vec{x};\theta) \tag{4.2}$$

and therefore simplifies the maximization procedure. In the case of the $B_s^0 \to J/\psi K^+K^-$ analysis, the function $p(\vec{x};\theta)$ is the differential decay rate introduced in Chapter 1, modified to take into account the detector response effects which are the decay-time resolution $G(t|\sigma_t)$ as a function of the decay-time uncertainty σ_t, reconstruction and selection efficiency as a function of decay time and angles, $\varepsilon(t,\Omega)$, and the estimate of the wrong-tag probability η, and the corresponding calibrated estimate ω ($\bar{\omega}$). The resulting normalised, differential decay rate is given by

$$\begin{aligned} p(t,\Omega|q,\eta,\sigma_t) = \frac{1}{N}\sum_{k=1}^{10} f_k(\Omega)\varepsilon(t,\Omega) \\ \cdot \{[(1+q(1-2\omega(\eta)))\cdot h_k(t|B_s^0) + (1-q(1-2\bar{\omega}(\eta)))\cdot h_k(t|\overline{B}_s^0)] \otimes G(t|\sigma_t)\}, \end{aligned} \tag{4.3}$$

where the definitions of angular functions, $f_k(\Omega)$, and time-dependent functions, $h_k(t|B_s^0)$ and $h_k(t|\overline{B}_s^0)$, are given in table 1.1 for each index k that runs over all possible configurations of the amplitudes contributing to the final state. To account for the presence of the S-wave, the sample is divided into six subsamples in m_{KK}, where i ($i \in [1;6]$) denotes the subsample index and the boundaries are defined as

$[990, 1008, 1016, 1020, 1024, 1032, 1050]$ MeV/c^2. In the fit to the each subsample, the interference between the S- and P-wave contributions is accounted for by multiplying amplitudes $k = 8, 9, 10$ with the corresponding effective coupling factor, C_{SP}^{i}. The details about the computation of the C_{SP} factors can be found elsewhere [72]. The C_{SP} values are found to be $0.8463, 0.8756, 0.8478, 0.8833, 0.9415$ and 0.9756 from the lowest to the highest $\mathrm{m_{KK}}$ bin.

The normalisation of the PDF, N, is given by

$$N = \int_{t=0.3\,\mathrm{ps}}^{15\,\mathrm{ps}} \int_{\Omega} \sum_{k=1}^{10} w_k f_k(\Omega)\varepsilon(\mathrm{t}) \cdot \{[(1 + q(1 - 2\omega(\eta))) \cdot h_k(\mathrm{t}|\mathrm{B_s^0}) + (1 - q(1 - 2\bar{\omega}(\eta))) \cdot h_k(\mathrm{t}|\overline{\mathrm{B}}_{\mathrm{s}}^{0})] \otimes G(\mathrm{t}|\sigma_{\mathrm{t}})\}, \tag{4.4}$$

where w_k are normalisation weights that are used to model the efficiency as a function of decay angles in the PDF.

From equation 4.4, it can be deduced that the sensitivity to ϕ_{s} depends on several experimental factors, $\sigma^{-1}(\phi_{\mathrm{s}}) \sim \sqrt{N\,\varepsilon_{\mathrm{tag}}}(1-2\omega)e^{-\frac{{\sigma_{\mathrm{t}}}^2\Delta m^2}{2}}$, where N is the signal yield; $\sqrt{\varepsilon_{\mathrm{tag}}}(1-2\omega)$ is the effective tagging power that specifies which part of the sample can be used for ϕ_{s} determination; and $e^{-\frac{{\sigma_{\mathrm{t}}}^2\Delta m^2}{2}}$ is the damping effect that is caused by the finite decay time resolution of the detector [73]. Each analysis step is designed in order to maximize the ϕ_{s} sensitivity, starting with the selection of the signal candidates. The background subtraction is performed in several steps, where first the background is significantly reduced using a dedicated selection, followed by the subtraction of peaking background contributions as described in the section 4.1. Subsequently, the signal candidates are separated from the remaining background candidates using the *sPlot* method [74] utilizing $\mathrm{m}(\mathrm{J/\psi K^+K^-})$ as the discriminating variable and using σ_{m} as conditional observable, as described in section 4.2.

Both the geometry of the LHCb detector and the selection requirements introduce a non-uniform efficiency as a function of the decay angles and time. Various selection requirements used by the trigger introduce a non-uniform efficiency as a function of decay time. To account for this, the sample under study is separated in two parts according to the trigger category. Events that pass only those trigger lines that have an explicit selection on the flight distance of the $\mathrm{B_s^0}$ candidate or its daughter particles are classified as trigger *biased*. Those that pass the selection of the lines which do not require time-biasing cuts are classified as *almost unbiased*. The efficiency, $\varepsilon(\mathrm{t})$ is then determined separately for the two trigger categories as well as for each of the two years of the data-taking to account for the differences in the data-taking conditions and reconstruction algorithms. Its determination is explained in the section 4.3.1. The efficiency as a function of decay angles is accounted for by normalisation weights w_k in the normalisation of the PDF. The determination of these weights is detailed in section 4.4.1

The $G(\mathrm{t}|\sigma_{\mathrm{t}})$ function in equation 4.4 denotes the gaussian decay-time resolution function with the width parameter given by the decay time uncertainty σ_{t}, which is estimated for each candidate using a kinematic fit [75] and then calibrated. The

calibration procedure is discussed in section 4.3.3. The PDF is conditional upon the estimated decay-time uncertainty.

As explained in the section 4.5, the flavour of the B_s^0 meson at production is determined using the same-side (SS) and opposite side (OS) flavour tagging algorithms. Each tagging algorithm provides the corresponding flavour tag decision q^{OS} and q^{SSK}, which can take the value ± 1 depending on the estimated flavour at production, B_s^0 ($\overline{B}_s^0$). If the type of B_s^0 meson can not be determined for the given candidate, the tag decision is set to zero. Together with the tag decision, the tagging algorithm provides an estimate, η, of the probability that the decision is estimated incorrectly, the so-called mistag probability. The mistag is calibrated with the procedure explained in section 4.5. The PDF is conditional upon the mistag probability.

All physics parameters are allowed to vary in the fit and are common across the subsamples, except for the S-wave fraction, F_S, and the phase difference $\delta_S - \delta_\perp$, which are independent parameters for each m_{KK} bin.

The analysis presented in this thesis was performed by a corresponding working group in the LHCb Collaboration and is summarised in the publication "Updated measurement of time-dependent CP-violating observables in $B_s^0 \to J/\psi K^+K^-$ decays" [72]. Some excerpts from the publication are presented in the thesis. For completeness, all analysis steps are mentioned in this thesis. Parts to which the author directly contributed are covered in more detail. Those include the treatment of Λ_b^0 background, the mass fit model, and the PDF normalisation including the description of the time acceptance as a product of two cubic splines.

4.1 Candidate selection

Candidate $B_s^0 \to J/\psi K^+K^-$ decays are combined from two oppositely charged tracks reconstructed as muons produced in the decay of $J/\psi \to \mu^+\mu^-$, with a pair of oppositely charged tracks, identified as kaons, coming predominantly from a $\phi \to K^+K^-$ decay. In hadronic collisions the multiplicity of particles produced in the primary proton-proton interaction is very high, resulting in a large number of reconstructed tracks in an event. When two tracks identified as muons are combined with two other tracks identified as kaons to form the signal candidate, it is possible that some of those tracks are either misidentified or do not originate from a $B_s^0 \to J/\psi K^+K^-$ decay. Random combinations formed from those tracks introduce a combinatorial background in the studied sample.

The search for signal events containing $B_s^0 \to J/\psi K^+K^-$ decays starts in the trigger system of the LHCb detector. The trigger system consists of three stages where at each stage events are required to pass trigger lines, as explained in section 3. For the hardware `L0` level, data passing any of the `L0` trigger lines are used in the analysis.

The subsequent software trigger consists of two stages. In `Hlt1` events are required to pass at least one of the trigger lines `Hlt1DiMuonHighMass` or `Hlt1TrackMuon` or `Hlt1TwoTrackMVA`. The `Hlt1DiMuonHighMass` line selects events with two well-identified oppositely charged muons with an invariant mass larger than $2700\,\mathrm{MeV}/c^2$. The `Hlt1TrackMuon` line retains events containing at least one muon with transverse momentum larger than 1 GeV/c and with a large impact parameter (IP) χ^2 with

respect to all PVs in the event, which is defined as the difference in the vertex-fit χ^2 of the PV fitted with and without the considered track. And the `Hlt1TwoTrackMVA` line selects events using a multivariate algorithm that identifies a two-track displaced vertex with a large sum of transverse momenta of the associated charged particles. The last two trigger lines have explicit requirements on the displacement of the signal tracks from the PV, which introduces a nontrivial dependence of the efficiency as a function of the B_s^0 decay time. Events that are selected by either of the `Hlt1TrackMuon` or `Hlt1TwoTrackMVA` lines, but not by the `Hlt1DiMuonHighMass` line, are classified as *biased* and are treated separately from the rest, *almost unbiased*, for which the efficiency is close to uniform as a function of B_s^0 decay time.

In the second stage of the trigger, events containing a $\mu^+\mu^-$ pair with invariant mass within 120 MeV/c^2 of the nominal J/ψ mass [7] and which form a vertex that is significantly displaced from the PV are selected, introducing further non-trivial contributions to $\varepsilon(t)$. Those events that pass the requirements of both trigger stages are persisted for further offline analysis.

Offline, two oppositely charged tracks identified as muons are required to originate from a common vertex and both must have a transverse momenta in excess of 500 MeV/c. To select only those muons coming from a J/ψ meson, the invariant mass of the $\mu^+\mu^-$ pair must be in the range 3020–3170 MeV/c^2. The other two tracks, required to form a B_s^0 candidate, have to be identified as kaons with transverse momenta larger than 500 MeV/c and with the invariant mass of the combination close to the nominal mass of the ϕ meson, i.e. within the interval 990–1050 MeV/c^2. The J/ψ meson candidates are further combined with these K^+K^- pairs to form the B_s^0 candidate. To minimize the effect of the detector resolution, the invariant mass of the combination, m(J/ψK^+K^-), is calculated from a kinematic fit that constrains the B_s^0 candidate to originate from the associated PV and which constrains m($\mu^+\mu^-$) to the known J/ψ mass [7]. If multiple PVs are reconstructed in the event, the one with the smallest value of the B_s^0 impact parameter significance is associated with the candidate. The J/ψK^+K^- invariant mass is required to be in the range 5200–5550 MeV/c^2. The decay time, t, and helicity angles of the B_s^0 candidate are computed with the same constraints applied. The lower bound on the decay time is set to 0.3 ps to suppress a large fraction of the combinatorial background.

The analysis makes use of machine learning techniques to discriminate between signal and background. A gradient-boosted decision tree (BDT) [76, 77] technique is used, as a more sophisticated and efficient alternative to a simple rectangular-cut-based selection. Various input quantities are used in the BDT to exploit the features of the signal decay in order to distinguish it from background, namely the track-fit χ^2 of the final-state particles, the particle identification probability, the quality of the candidate J/ψ and B_s^0 decay vertices, the p_T and pseudorapidity of the B_s^0 candidate and its IP with respect to the origin vertex and p_T of the K^+K^- combination. The corresponding distributions in the simulated signal sample are weighted to match those in data, such that the simulated sample can be used as a signal proxy for training the BDT. As a background proxy, candidates from the upper sideband in data i.e. candidates within the interval 5450 MeV/c^2 < m(J/ψK^+K^-) < 5550 MeV/c^2 are used. Only the higher

invariant-mass region is used as proxy for the combinatorial background, as the lower sideband is not a good combinatorial background representation, since it contains peaking backgrounds as explained below. The selection requirement on the BDT output is chosen such that it maximises the decay-time dependent fit sensitivity to the parameters of interest. The figure of merit (FOM) used to optimise the BDT response is given by

$$\mathrm{FOM} = \frac{(\sum_i w_i)^2}{\sum_i w_i^2}, \tag{4.5}$$

where the index i runs over all candidates in the sample and w_i are per-candidate weights that are determined from the invariant mass fit that is performed at each point in the scan over the BDT response. The value of the BDT cut is chosen at the maximum point of the FOM curve.

4.1.1 Peaking backgrounds

Apart from the combinatorial background that is formed from randomly combined tracks, the signal sample contains another type of background that comes from real meson or baryon decays. The two main contributions originate from decays where the pion (in $B^0 \to J/\psi K^{*0}$, $K^{*0} \to K^+\pi^-$ decays) or the proton (in $\Lambda_b^0 \to J/\psi p K^-$ decays) are misidentified as a kaon. These backgrounds lie around the B_s^0 mass in the $m(J/\psi K^+K^-)$ distribution, as shown in figure 4.1 and therefore have to be carefully studied and accounted for.

In order to estimate the contributions from both decay modes, the $m(J/\psi K^+K^-)$ sidebands are used. For each of the two background modes, the $J/\psi K^+K^-$ invariant mass is recalculated under a different particle hypothesis, replacing the mass of the kaon with the mass of the proton (pion) for the Λ_b^0 (B^0) contribution. The amount of peaking background candidates for both modes found in the sideband region can be extrapolated to the full $m(J/\psi K^+K^-)$ mass region and the fraction of Λ_b^0 (B^0) decays with respect to the number of the signal decays is found to be approximately 4.5 % (0.3 %). In order to suppress these contributions, as described below, a tighter particle-identification requirement on the kaon is applied. Those $B_s^0 \to J/\psi K^+K^-$ candidates where the probability of one of the kaon candidates to be a pion is larger than 0.7, or with probability of the kaon candidate to be a kaon is smaller than 0.35, and the value of $m(J/\psi K^\pm\pi^\mp)$, obtained by setting the mass of the candidate to the pion mass, is within ± 15 MeV of the nominal B^0 meson mass [7], are removed. To reduce the contribution from Λ_b^0 decays, the $B_s^0 \to J/\psi K^+K^-$ candidate is removed if the probability of one of the kaon candidates to be a proton is larger than 0.7, or if the probability of the kaon candidate to be a kaon is smaller than 0.35, and the value of the $J/\psi K^\pm\pi^\mp$ invariant mass, obtained by setting the mass of the candidate to the proton mass is within $\pm$ 15 MeV of the mass of the Λ_b^0 baryon [7]. After these vetoes are applied the fraction of the leftover B^0 contribution is estimated to be less than 0.1 % and therefore is neglected in the further analysis. A systematic uncertainty accounting for this approximation is assigned. The contribution from the Λ_b^0 decays is reduced to less than 1.4 %. The remaining Λ_b^0 candidates can be treated in a few different ways. One

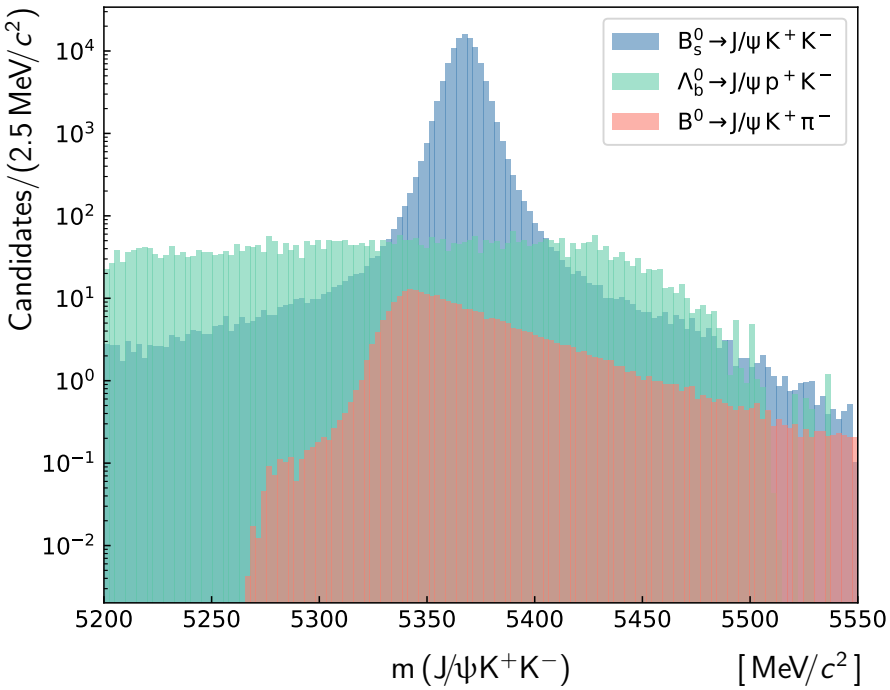

Figure 4.1: Invariant-mass distributions of $J/\psi K^+ K^-$ in simulated $B_s^0 \to J/\psi K^+ K^-$, $\Lambda_b^0 \to J/\psi p K^-$ and $B^0 \to J/\psi K^{*0}$ decays.

option is to explicitly model the Λ_b^0 contribution in the fit to the $J/\psi K^+ K^-$ invariant mass and subsequently subtract it during the *sWeighting* procedure. The downside of this method is that the correlations between the candidate mass and the angular variables are not accounted for. To overcome this, another method is used in which simulated Λ_b^0 decays are inserted into the data sample with negative weights, such that the sum of the negative weights is equal to minus the number of the expected Λ_b^0 candidates

$$\sum_{i=1}^{N(\Lambda_b^0)} w_{\mathrm{MC},i}^{\Lambda_b^0} = -N_{\mathrm{data}}^{\Lambda_b^0 \to J/\psi p K^-}. \tag{4.6}$$

The inserted simulated sample of $\Lambda_b^0 \to J/\psi p K^-$ decays is weighted to match the resonant structure obtained from the data in the pentaquark analysis [78]. The kinematic distributions of the Λ_b^0 baryon, p and p_T, are also weighted to correct for the difference between the data and simulation.

The information provided by the tagging algorithms is resampled from data. The mis-tag probabilities in the $\Lambda_b^0 \to J/\psi p K^-$ simulation are resampled according to their distributions in the vetoed data. To obtain the distributions the *sPlot* technique [74] is used with $m(J/\psi p K^-)$ as discriminating variable. The value of $m(J/\psi p K^-)$ is obtained from the $B_s^0 \to J/\psi K^+ K^-$ dataset, substituting the mass of one of the kaon candidates with the mass of the proton. If a K^- (K^+) candidate is assigned the proton mass, then the probability of the candidate to be a kaon is required to be larger than 0.7.

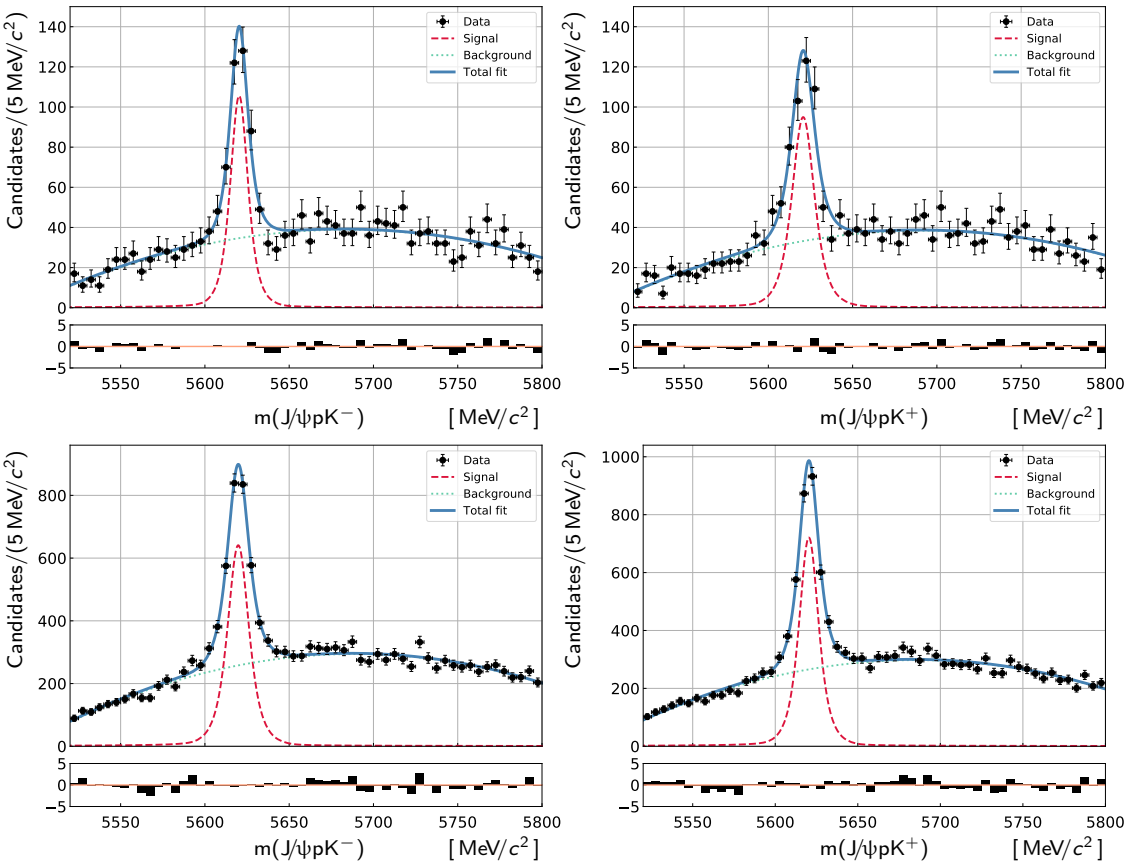

Figure 4.2: The invariant-mass distribution from J/ψpK$^-$ (left) and J/ψ$\bar{\text{p}}$K$^+$ (right) combinations obtained with 2015 (top) and 2016 (bottom) data sample.

The m(J/ψpK$^-$) distribution is fitted with a double-sided Hypatia function [79] with the tail parameters fixed to the values obtained from the $\Lambda_b^0 \to$J/ψpK$^-$ MC and the background is modelled using Chebychev polynomials. The results of the fit to the 2016 and 2015 data are shown in figure 4.2.

Next, the *sWeighting* procedure is performed and the distributions of OS and SS mis-tag probabilities are obtained. Their distributions are shown in figure 4.3 for 2015 and 2016 data samples (the mis-tag probabilities are shown only for the tagged candidates).

Each candidate in the $\Lambda_b^0 \to$J/ψpK$^-$ simulated sample is assigned a tagging decision according to OS only, SS only, both OS and SS tagged fractions observed in data. In case the candidate is OS (SS) tagged, the tagging decision is randomly assigned to be either B_s^0 or $\overline{B}_s^0$ with equal probability. The m(J/ψK$^+$K$^-$) distribution is shown in figure 4.4 for the simulated Λ_b^0 sample after the full selection and reweighting procedure have been applied.

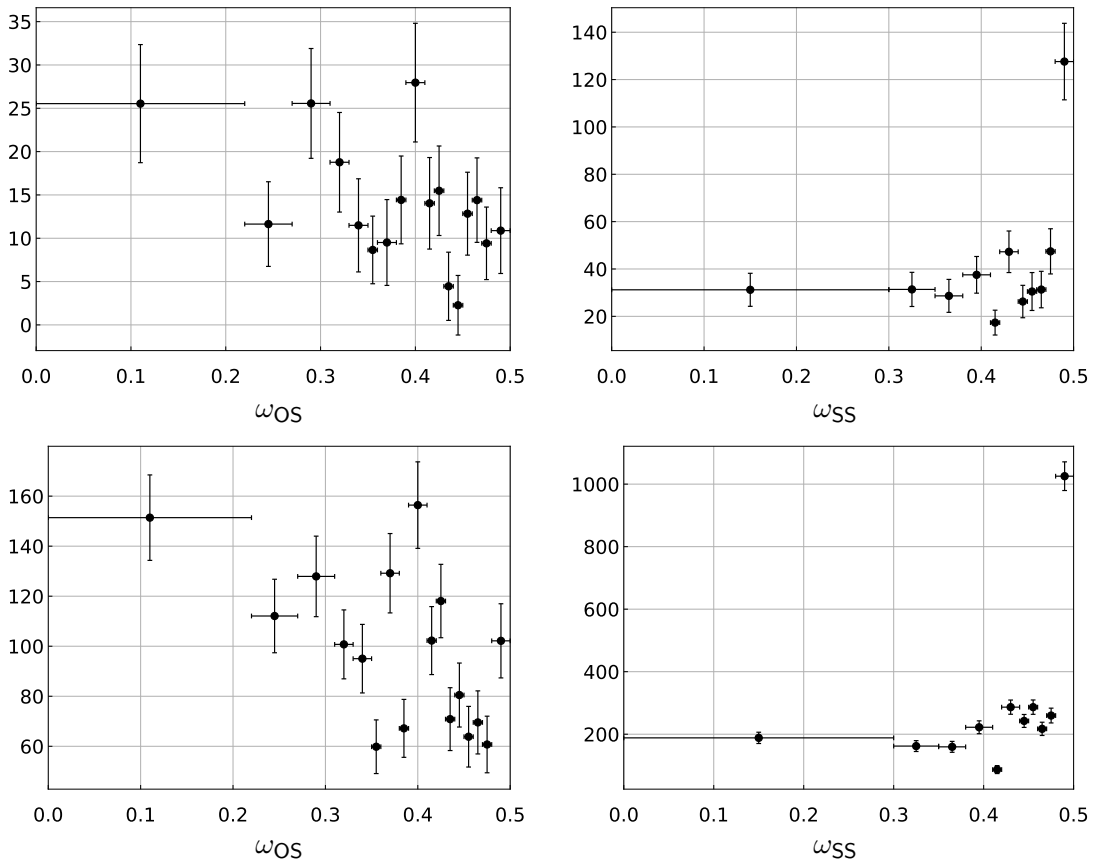

Figure 4.3: The distributions of OS mis-tag probability (left) and SS mis-tag probability (right) obtained with 2015 (top) and 2016 (bottom) data samples.

4.1.2 Multiple candidates

Following the recommendation given in reference [80], the presence of events containing multiple reconstructed candidates after the full selection has been applied are investigated. The fraction of the events containing more than one candidate is found to be 1.51% in the full B_s^0 mass region $[5200, 5550]\,\text{MeV}/c^2$, however in the narrow mass window $[5340, 5400]\,\text{MeV}/c^2$ surrounding the signal B_s^0 peak only approximately 0.27% of events contain more than one candidate. For the majority of the events with multiple candidates, the reconstructed J/ψ meson is shared between the candidates and different kaon candidates are added. Due to the smallness of the fraction of the multiple candidates in the sample, they are kept in the analysis and a study of the associated systematic uncertainty is performed as explained in the Chapter 5.

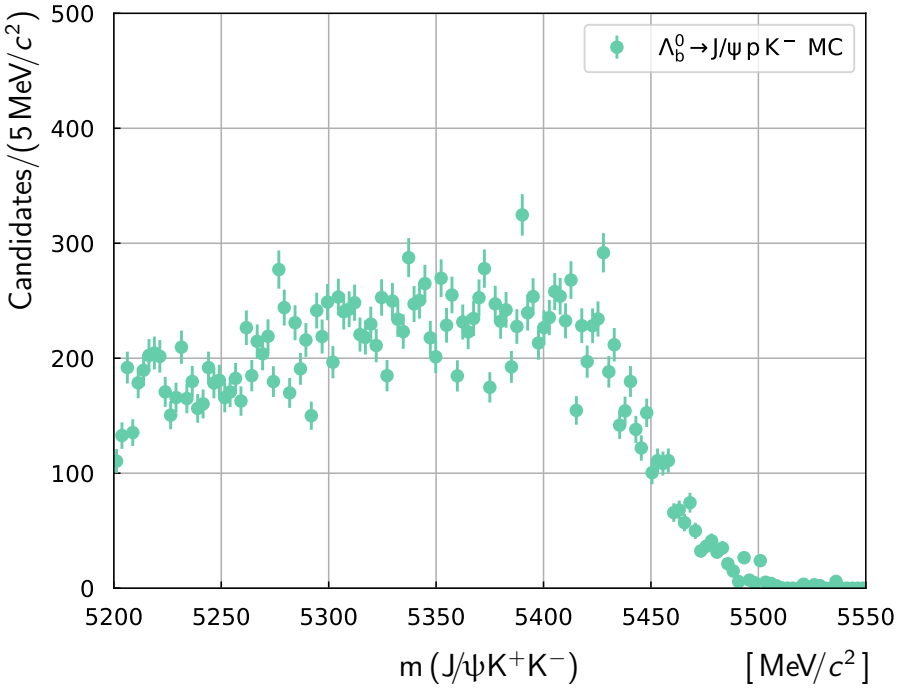

Figure 4.4: Distribution of m ($J/\psi K^+K^-$) from the $\Lambda_b^0 \to J/\psi pK^-$ MC after final selection and subsequent reweighting.

4.2 Mass fit

After the offline selection is applied and the negatively-weighted simulated Λ_b^0 sample is injected, a small fraction of background remains in the sample as can be seen in the weighted $J/\psi K^+K^-$ invariant-mass distributions in figure 4.11. Some of the background has invariant mass very close to the known B_s^0 mass [7] and therefore has to be statistically separated from the signal. The *sPlot* technique [74] is used to statistically subtract those background candidates. As explained in reference [74], the *sPlot* technique relies on the assumption of no correlation between the discriminating variable and the variables of interest. However, it has been found in the previous version of the analysis [81] that the shape of the $J/\psi K^+K^-$ invariant mass is correlated to one of the observables, the helicity angle $\cos(\theta_\mu)$. In order to account for this correlation a new signal mass shape is introduced as explained below. If for the signal and background events the corresponding distributions are known for the so-called discriminating variable, then the method allows to unfold signal and background distributions for the remaining observables of interest. The first step of the *sPlot* procedure is to perform a maximum likelihood fit to the invariant-mass distribution in order to extract the signal and background yields N_s and N_b. Following the definition in reference [82], the corresponding extended log-likelihood can be written as

$$ln\mathcal{L}(\theta) = \sum_{i=1}^{N} ln\ (N_s f_s(\theta_s) + N_b f_b(\theta_b)) - (N_s + N_b) \tag{4.7}$$

where $f_s\,(f_b)$ is the PDF with the set of parameters $\theta_s\,(\theta_b)$ for the description of signal (background).

4.2.1 Shape of the combinatorial background

The invariant mass of the $J/\psi K^+K^-$ combinations is used as the discriminating variable, as the signal and background distributions in this observable are very distinct. The signal distribution is a delta function, centered at the signal mass and subsequently convolved with the detector resolution, while the combinatorial background typically follows an exponential distribution. The shape of the combinatorial background can be quantitatively established from the basic principles of kinematics as explained in reference [83]. The derivation follows from two kinematics laws: first, the p_T distribution of particles forming combinatorial background follows an exponential distribution; second, light particles, produced at the LHC, form, as function of momentum, a so-called pseudorapidity plateau. The latter is shown in the paper of R. Feynman [84]. Following these two main assumptions, the p_T of J/ψ and ϕ are generated according to exponential distributions with the mean of the distribution taken as the approximate average p_T in data, which is around 3 GeV/c for J/ψ and 2.5 GeV/c for ϕ. The pseudorapidity, η, is generated to be flat within the LHCb acceptance, i.e. between 2 and 5, mimicking the pseudorapidity plateau. The momentum of the particles can be calculated as $p = p_T \cosh(\eta)$. The generated distributions are shown in figure 4.5. The invariant mass is calculated as $m = \sqrt{(\sum E)^2 - (\sum p)^2}$ where the masses of

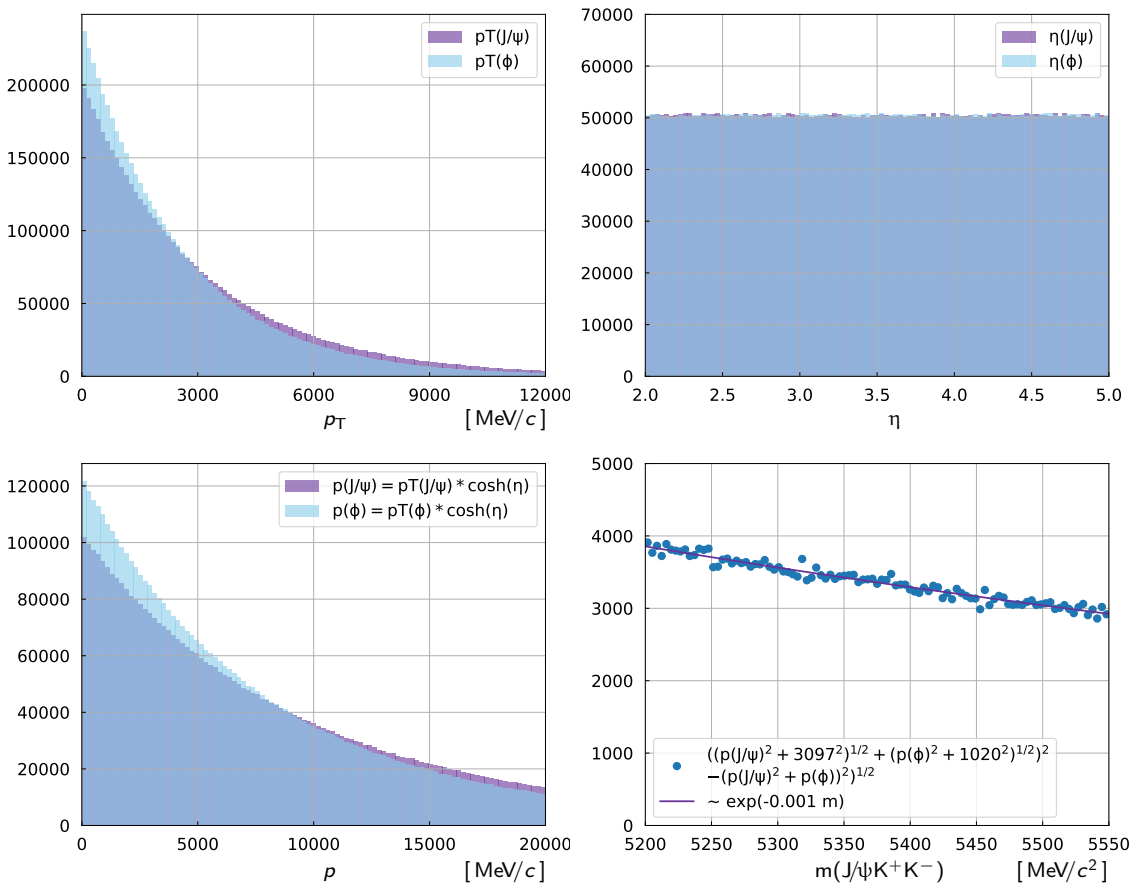

Figure 4.5: The distributions of the generated p_T and η of J/ψ and ϕ, of the derived momenta and of the derived invariant mass.

the J/ψ and ϕ are taken as their nominal masses and assuming that their momenta are parallel. The resulting invariant-mass distribution is shown in the figure 4.5, zoomed in around the fitting range of the $B_s^0 \rightarrow J/\psi K^+K^-$. The resulting distribution is an exponential. To determine the decay constant, the distribution is fitted with an exponential function. The value is found to be around $-0.001 \frac{1}{\text{MeV}/c^2}$. Following this, the PDF for the combinatorial background in the $J/\psi K^+K^-$ invariant-mass fit is described by an exponential function with the initial value of the parameter representing the slope set to the value found in this study.

4.2.2 Effect of J/ψ mass-constraint

As described in section 4.1, in order to improve the measured mass resolution, the invariant mass is computed from a kinematic fit which constrains the mass of the J/ψ to the PDG value [7] and which constrains the reconstructed momentum of the B_s^0 meson to point back from the reconstructed decay vertex to the primary vertex. Since this procedure can potentially cause an additional correlation between the invariant mass and the decay time, it has first to be verified that such a correlation is not actually

introduced. To do that, the results of the maximum log-likelihood fit to the invariant mass of the B_s^0 candidates are computed both with and without the PV constraint and compared. The m($J/\psi K^+K^-$) distribution is split in eight approximately equally populated bins in the decay time with boundaries [0.3, 0.4, 0.5, 0.6, 0.8, 1, 2, 4, 15] ps and mass distribution in each bin is fitted. The mass model used to describe the invariant-mass distributions for the signal is a sum of two Gaussian functions with shared mean parameter but different widths and with the fraction of the two Gaussians fixed, and an exponential distribution for the combinatorial background. The procedure is repeated for masses computed both with and without the PV constraint and the resulting fit parameters, σ_1, σ_2 and γ, are shown in figure 4.6. The resolution of the mass increases as a function of decay time, which is taken into account in the final mass model by using the per-event computed mass uncertainty. The slope of the exponential distribution varies significantly as a function of decay time. This observed correlation is taken into account in the evaluation of the systematic uncertainty. Since the size of the correlation is the same for the invariant masses determined without and with the PV constraint, the latter is chosen due to the improvement in the mass resolution.

The signal component of the invariant-mass distribution is described with a double-sided *Crystal Ball* (CB) [85] function. The core of the distribution is a Gaussian function with mean, μ, and width σ, connected at the points α_1 on the left and α_2 on the right with two additional exponential-like tails with n_1 (n_2) as slopes of the corresponding exponential distributions. The mathematical form reads as follows:

$$\mathrm{CB}(m;\mu,\sigma,\alpha_1,\alpha_2,n_1,n_2) = N\cdot\begin{cases} e^{-\frac{(x-\mu)^2}{2\sigma^2}}, & \text{for } \alpha_1 < \frac{(x-\mu)}{\sigma} < \alpha_2 \\ A_1\cdot\left(B_1-\frac{(x-\mu)}{\sigma}\right)^{-n_1}, & \text{for } \frac{(x-\mu)}{\sigma} < \alpha_1 \\ A_2\cdot\left(B_2-\frac{(x-\mu)}{\sigma}\right)^{-n_2}, & \text{for } \frac{(x-\mu)}{\sigma} > \alpha_2 \end{cases}$$
$$\text{where } A_i = \left(\frac{n_i}{|\alpha_i|}\right)^{n_i}\cdot e^{-\frac{|\alpha_i|^2}{2}},\ B_i = \frac{n_i}{|\alpha_i|} - |\alpha_i|, i = [1,2] \qquad (4.8)$$

and N is the normalisation parameter. The use of a double-sided CB function is motivated by the need to properly describe the tails of the invariant-mass distribution. The tail on the left is mainly caused by final state radiation: the radiated photons are not reconstructed and the computed invariant mass thus ends up below the expected value. The J/ψ mass constraint introduces a tail on the right side of the B_s^0 mass. A J/ψ meson may decay to $\mu^+\mu^-$ pair and a radiative photon, which is not reconstructed, therefore the $\mu^+\mu^-$ invariant mass would lie below the J/ψ mass. When the J/ψ mass constraint is applied, these $\mu^+\mu^-$ pairs are now constrained to a larger invariant mass, and the invariant mass of the corresponding B_s^0 candidates is overestimated, appearing as a tail on the right side of the B_s^0 mass. In order to properly model the shape of these tails, the simulated sample is used.

4.2.3 Correlation with $\cos(\theta_\mu)$

The shape of the $J/\psi K^+K^-$ invariant mass is found to be correlated to the helicity angle $\cos(\theta_\mu)$. This correlation is expected since the invariant-mass resolution depends

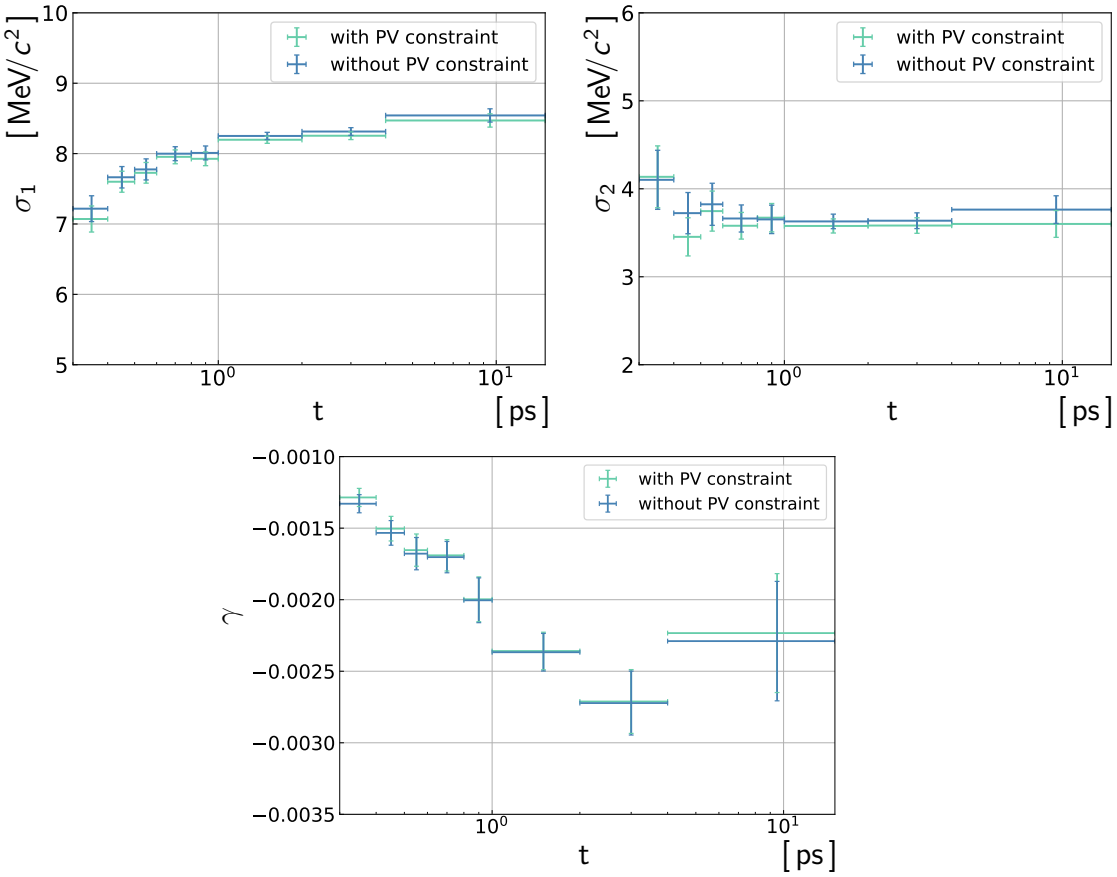

Figure 4.6: Values of the resolutions of the two signal Gaussians, σ_1 (top left) and σ_2 (top right), and the slope for the background exponential PDF (bottom) obtained by fitting the $m(J/\psi K^+K^-)$ distribution as a function of the B_s^0 decay time. In blue are the values obtained using $m(J/\psi K^+K^-)$ from a kinematic fit constraining the mass of the J/ψ to the PDG value, in green are the values obtained using in addition the PV constraint in the evaluation of $m(J/\psi K^+K^-)$.

on the observed opening angle between the two muons in the final state. The error of the quasi-two-body decay can be used as a good approximation of the estimated per-event error. Assuming that masses of the daughter particles are much smaller than their momenta and their uncertainties are negligible, the uncertainty on mass M of the mother particle decaying to two daughter particles with masses m_1 and m_2 is computed as

$$\sigma_M = \sqrt{\left(\frac{\sigma_{p_1}}{p_1}\right)^2 + \left(\frac{\sigma_{p_2}}{p_2}\right)^2 + \left(\frac{\sigma_{\cos\theta}}{1-\cos\theta}\right)^2} \cdot \frac{M^2 - m_1^2 - m_2^2}{2M} \tag{4.9}$$

where $\sigma_{p_{1(2)}}$ is uncertainty on the momenta of daughter particles and $\cos\theta$ is cosine of the angle between the two momenta. The mass uncertainty depends on the angle between the two daughter particles. In the $J/\psi K^+K^-$ final state, the angle between the directions of the J/ψ and ϕ momenta is correlated with the angle between the

momenta of μ^+ and μ^-. This is due to the fact that the mass of the ϕ is very close to the mass of the K^+K^- pair and therefore the opening angle between two kaons is very small. As the opening angle between the muons is correlated to the helicity angle θ_μ, the mass resolution varies for different values of $\cos(\theta_\mu)$. The correlations between the per-event mass uncertainty and both cosine of the angle between the muons in the laboratory frame and the helicity angle $\cos(\theta_\mu)$ is shown in figure 4.7, which is obtained from the simulated $B_s^0 \to J/\psi K^+K^-$ sample.

This observed correlation is not properly taken into account when fitting the mass distribution with a PDF that has only a single parameter σ, describing the average width of the distribution, independent of $\cos(\theta_\mu)$. In order to take into account the observed correlation, the mass uncertainty of $m(J/\psi K^+K^-)$, estimated on an event-by-event basis from the vertex fit, is used. The per-event mass uncertainty of $m(J/\psi K^+K^-)$ is introduced into the mass fit as a conditional observable. A conditional PDF of x is a PDF that gives the probability density of x, given a certain value of y, where y is the conditional observable. The conditional PDF is defined as

$$\sum_i P_i(x,y) = \sum_i (P_i(x|y)P(y)) = \sum_i (P_i(x|y))P(y). \tag{4.10}$$

The observable y therefore becomes a parameter of a function, whose value is taken directly from data on an event-by-event basis. As long as the actual distribution of y is the same for signal and background, the term $P(y)$ factors out of the sum in equation 4.10, and is thus irrelevant in the likelihood fit. The distributions of the per-event mass uncertainty in the signal region (approximately one standard deviation around the B_s^0 mass: $\pm 7\,\mathrm{MeV}/c^2$), in the sidebands ($m(J/\psi K^+K^-) < 5310\,\mathrm{MeV}/c^2$ or $m(J/\psi K^+K^-) > 5420\,\mathrm{MeV}/c^2$) and in the simulation sample are shown in figure 4.8 (left). The distributions of the per-event mass uncertainty separately for the upper and lower sideband regions are shown in figure 4.8 (right). Since the distributions of the per-event mass uncertainty are very similar but not identical between the signal region and sideband region, a corresponding systematic uncertainty is assessed, as described in Chapter 5.

4.2.4 Mass PDF

The mass PDF used in this analysis accounts for the difference in the mass uncertainty on an event-by-event basis. The parameter σ of the CB is parametrised such that it is dependent on the per-event mass uncertainty. The quadratic dependency is chosen based on the the parametrisation found in study of the simulated samples. To check the relation between the per-event mass uncertainty and the true invariant-mass resolution, the simulated $B_s^0 \to J/\psi K^+K^-$ sample is divided in 100 equally populated bins in the per-event mass uncertainty. The true invariant-mass resolution is defined as the difference between the generated and reconstructed values in the simulation. The fit to the $J/\psi K^+K^-$ invariant mass is performed in the each bin with a single Gaussian function to obtain the estimated true resolution. To be able to neglect the tails of the signal distribution, the fit is performed in a very narrow range around the

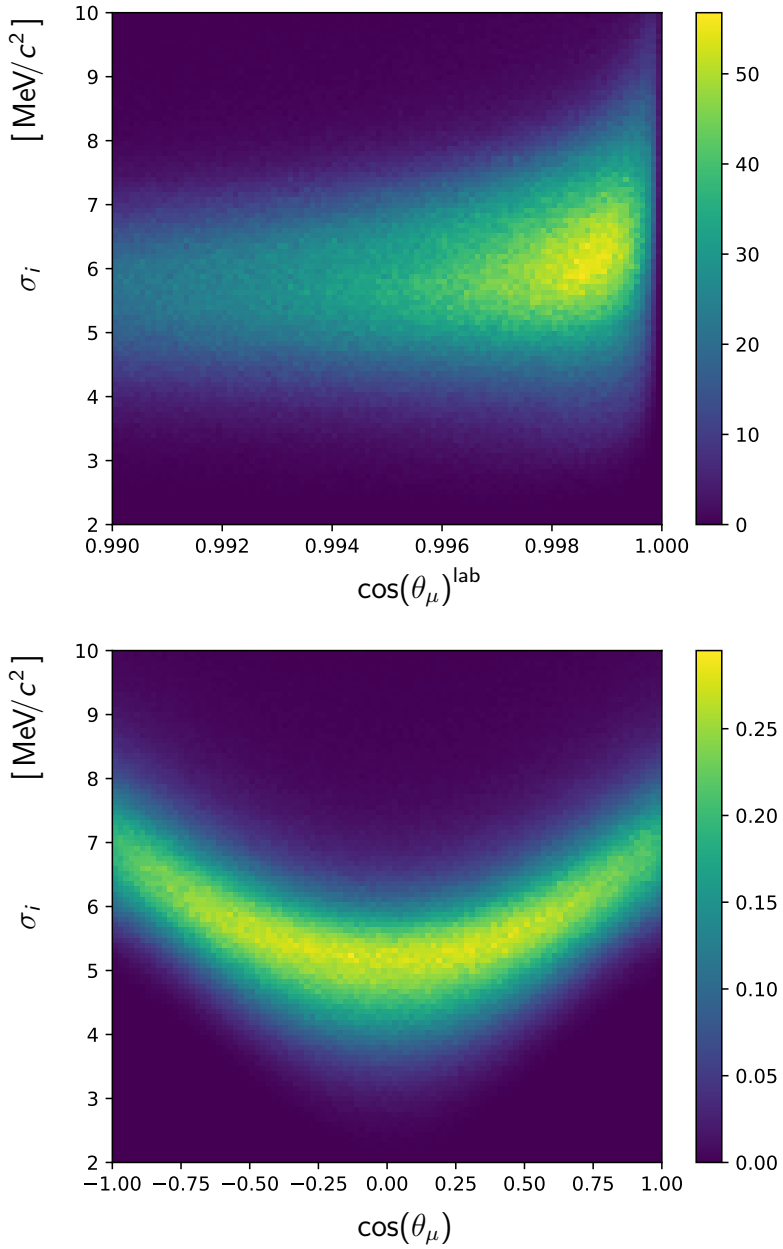

Figure 4.7: Two-dimensional histograms with (top) $\cos(\theta_\mu)$ in lab frame and (bottom) $\cos(\theta_\mu)$ in the helicity frame on the x-axis and on the y-axis, the estimated per-event mass uncertainty of m ($J/\psi K^+K^-$), obtained with the simulated $B_s^0 \rightarrow J/\psi K^+K^-$ sample.

B_s^0 mass, m ($J/\psi K^+K^-$) in [5355, 5380] MeV/c^2. The resulting distribution of the estimated resolution (σ_{True}) as a function of the per-event mass error (σ_i) is shown in figure 4.9. The true resolution is related to the per-event mass uncertainty with a quadratic dependence. Therefore the following parametrisation in the mass fit is chosen: $\sigma_{CB} = s_1\,\sigma_i + s_2\,\sigma_i^2$, where s_1 and s_2 are free parameters of the fit. When the estimated invariant-mass error is zero the true resolution is also zero and therefore

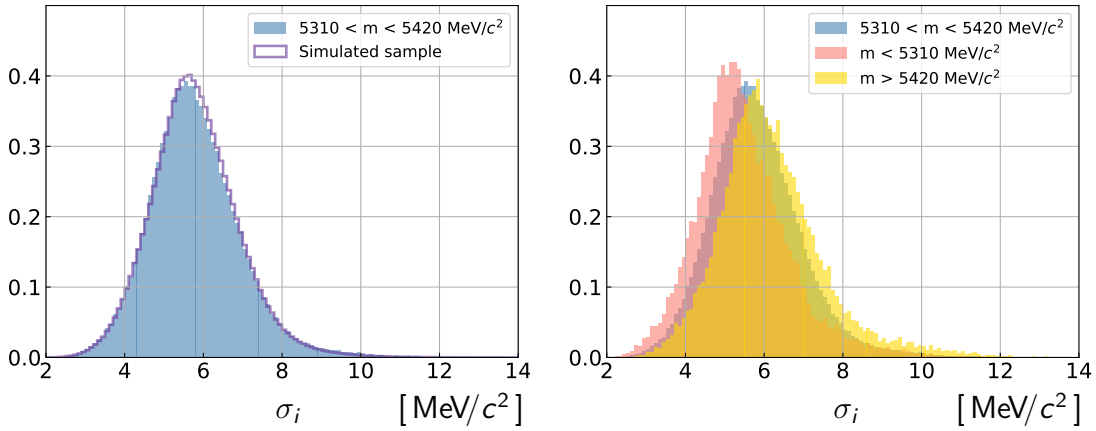

Figure 4.8: On the left are the normalised distributions of the per-event mass uncertainty in the signal region $5310 < \mathrm{m}(\mathrm{J/\psi K^+K^-}) < 5420\,\mathrm{MeV}/c^2$ in the data sample and in the simulated sample. On the right are normalised distributions of the per-event mass uncertainty in the signal region, left sideband $\mathrm{m}(\mathrm{J/\psi K^+K^-}) < 5310\,\mathrm{MeV}/c^2$ and right sideband $\mathrm{m}(\mathrm{J/\psi K^+K^-}) > 5420\,\mathrm{MeV}/c^2$.

the offset is set to zero in the mass fit to reduce the number of free parameters in the fit. The blue line in figure 4.9 represents the $(s_1\,\sigma_i + s_2\,\sigma_i^2)$ curve, where s_1 and s_2 are the fit parameters. The values obtained from the fit are $s_1 = 1.069 \pm 0.004$ and $s_2 = 0.014 \pm 0.001\ \frac{1}{(\mathrm{MeV}/c^2)}$. The scale factors in data are expected to be of the same order, however the values can be different since the σ parameter of the CB does not correspond exactly to the resolution of the invariant mass. When the magnitudes of α_i parameters are significantly below 1.5 the CB-σ parameter is smaller than the corresponding Gaussian-σ parameter, as follows from equation 4.8.

At the $\mathrm{B^0}$ mass a small contribution originating from $\mathrm{B^0} \to \mathrm{J/\psi K^+K^-}$ decays is observed. The final-state particles in this decay are exactly the same as in the signal decay, but they originate from a $\mathrm{B^0}$ meson instead. This contribution is modelled in the mass fit with a Gaussian distribution. The difference between the mean of $\mathrm{B_s^0}$ and $\mathrm{B^0}$ distributions in the fit is fixed to the known difference of the $\mathrm{B_s^0}$ and $\mathrm{B^0}$ masses. The resolution of the $\mathrm{B^0}$ contribution is fixed to 7 MeV/c^2, which is the value obtained by fitting the mass distribution of the $\mathrm{B^0} \to \mathrm{J/\psi K^{*0}}$ control channel. A different value for the mass resolution is studied as a possible source to the systematic uncertainty as mentioned in Chapter 5. During the *sPlot* procedure, the $\mathrm{B^0}$ component is treated as background species together with the combinatorial component and *sWeights* are calculated accordingly.

The full PDF is then

$$\begin{aligned} p = {} & N_{\mathrm{sig}}\mathrm{CB}(\mathrm{m}; \mu, \alpha_1, \alpha_2, n_1, n_2, s_1, s_2|\sigma_i) \\ & + N_{\mathrm{bkg}}\left[(1 - f_{\mathrm{B^0}})e^{-\gamma_b \mathrm{m}} + f_{\mathrm{B^0}}\mathrm{G}(\mathrm{m}; \mu_{\mathrm{B^0}}, \sigma_{\mathrm{B^0}})\right], \end{aligned} \tag{4.11}$$

where N_{sig} and N_{bkg} are the number of signal and background events correspondingly, μ is the mean, s_1 and s_2 are scale factors which account for possible underestimation of the per-event mass uncertainty, $\alpha_1, \alpha_2, n_1, n_2$ are the parameters describing the tails,

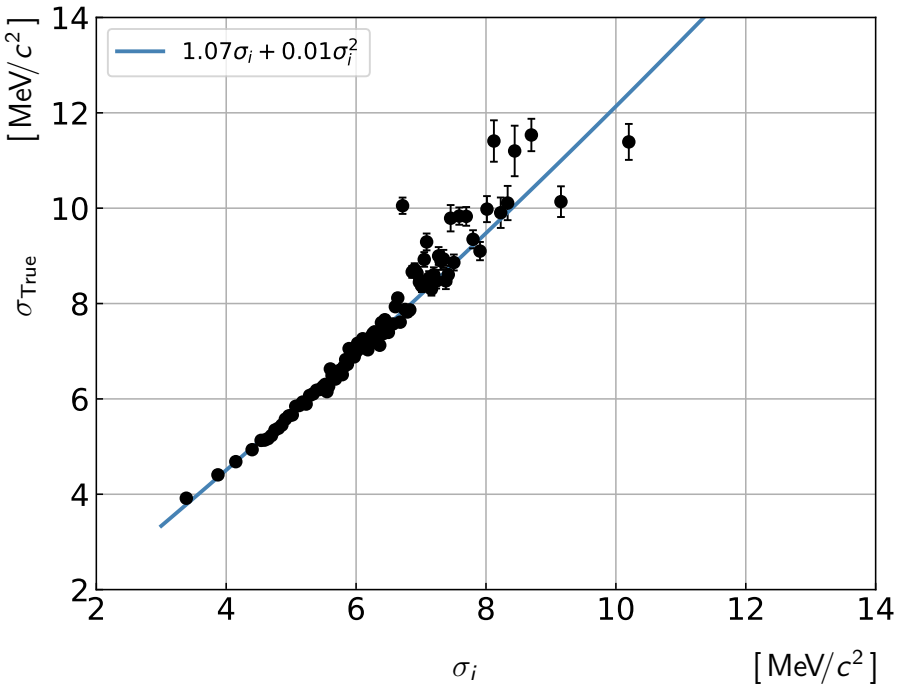

Figure 4.9: Distribution of the per-event mass error (σ_i) vs true estimated resolution (σ_{True}), obtained using simulation. The result of the fit to the distribution is shown with the blue line.

and γ_b is the slope of the exponential in the background distribution. The fraction of $B^0 \to J/\psi K^+K^-$ decays is denoted as f_{B^0}.

For the fit to the m($J/\psi K^+K^-$) distribution, the sample is divided into twenty-four subsamples, each with an independent signal fraction and different signal mass shapes. The subsamples correspond to six bins in the K^+K^- invariant mass ([990, 1008, 1016, 1020, 1024, 1032, 1050] MeV/c^2), two trigger categories:

Biased: `Hlt1TrackMuonDecision` or `Hlt1TwoTrackMVADecision` and not `Hlt1DiMuonHighMassDecision`

Almost unbiased: `Hlt1DiMuonHighMassDecision`

and two years of the data-taking (2015 and 2016). In order to obtain the $J/\psi K^+K^-$ signal mass shape parameters in each category, the simulated sample is used.

4.2.5 Mass fit to the simulated sample

Particles, generated in the simulated sample undergo the full LHCb reconstruction to mimic the reconstruction of the data. For some candidates it can occur that non-signal objects in an event are reconstructed as signal ones. These candidates should not be present in the simulated sample. To find these candidates a truth-matching procedure is applied. The truth-matching algorithm matches reconstructed and generated particles in the simulated sample. This algorithm assigns each candidate to one of the so-called background categories. The first category consists of pure signal events. The

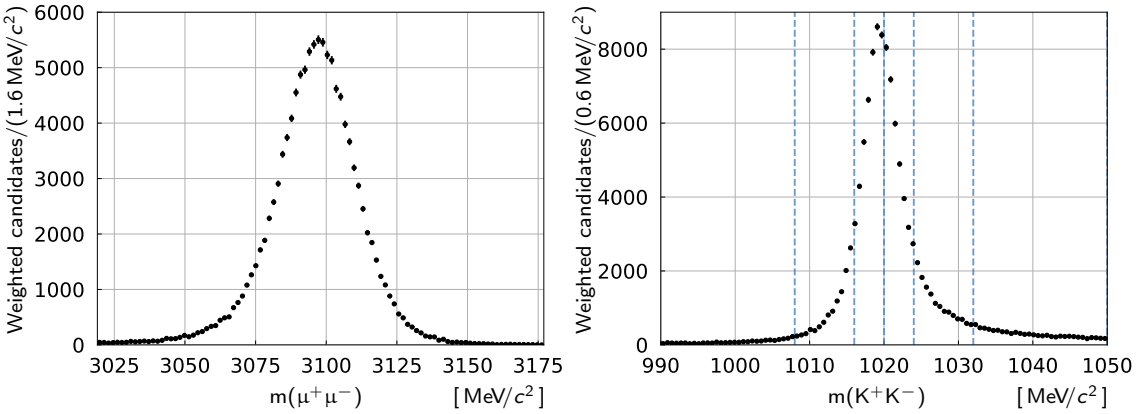

Figure 4.10: Distributions of the (left) $\mu^+\mu^-$ and (right) K^+K^- invariant mass from selected $B_s^0 \to J/\psi K^+K^-$ decays. The background is subtracted using the *sPlot* technique. The dashed red lines indicate the boundaries of the six bins.

other background categories are split into those with candidates with the final state radiation (FSR), and those with ghost tracks. A shortcoming of the truth-matching algorithm is that not all categories are always assigned correctly, as a result some of the signal is wrongly matched to the ghost background category. It can be observed as a peaking contribution in the non-peaking invariant-mass distribution of the ghost background category. This peaking contribution has to be taken into account to properly represent the reconstruction effects. To do so, first, only signal and FSR events are selected and the mass fit is performed only with the signal component of the PDF to determine the tail parameters of the signal distribution. The corresponding plots are shown in figures A.1 to A.4. Table A.1 summarises the obtained fit parameters. The resulting tail parameters of the double-sided CB function, $\alpha_1, \alpha_2, n_1, n_2$, are fixed when performing the fit on the full simulated sample (that includes signal, FSR and ghost events), with an exponential introduced as background PDF. The *sWeighting* procedure is performed on the simulated sample to statistically subtract the non-peaking component in the ghost background category. The corresponding plots are shown in figures A.5 to A.8. In the following analysis steps, only the distributions in the simulated sample weighted with signal weights are used.

4.2.6 Results

The peaking-background-subtracted invariant-mass distributions in data are fitted using the fit parameters obtained from the fit to the simulated signal sample (ghost and FSR categories). The background-subtracted distributions of the $\mu^+\mu^-$ and K^+K^- invariant mass are shown in figure 4.10. The invariant-mass distributions of the samples are shown together with the total curves in figure 4.11 for 2015 (top) and 2016 (bottom). The $B_s^0 \to J/\psi K^+K^-$ signal yields are $15\,316 \pm 131$ and $102\,378 \pm 340$, respectively, in the fit mass range for 2015 and 2016 data. The distributions, together with the fit curves, in the six K^+K^- mass bins and two trigger categories for 2015 and 2016 data

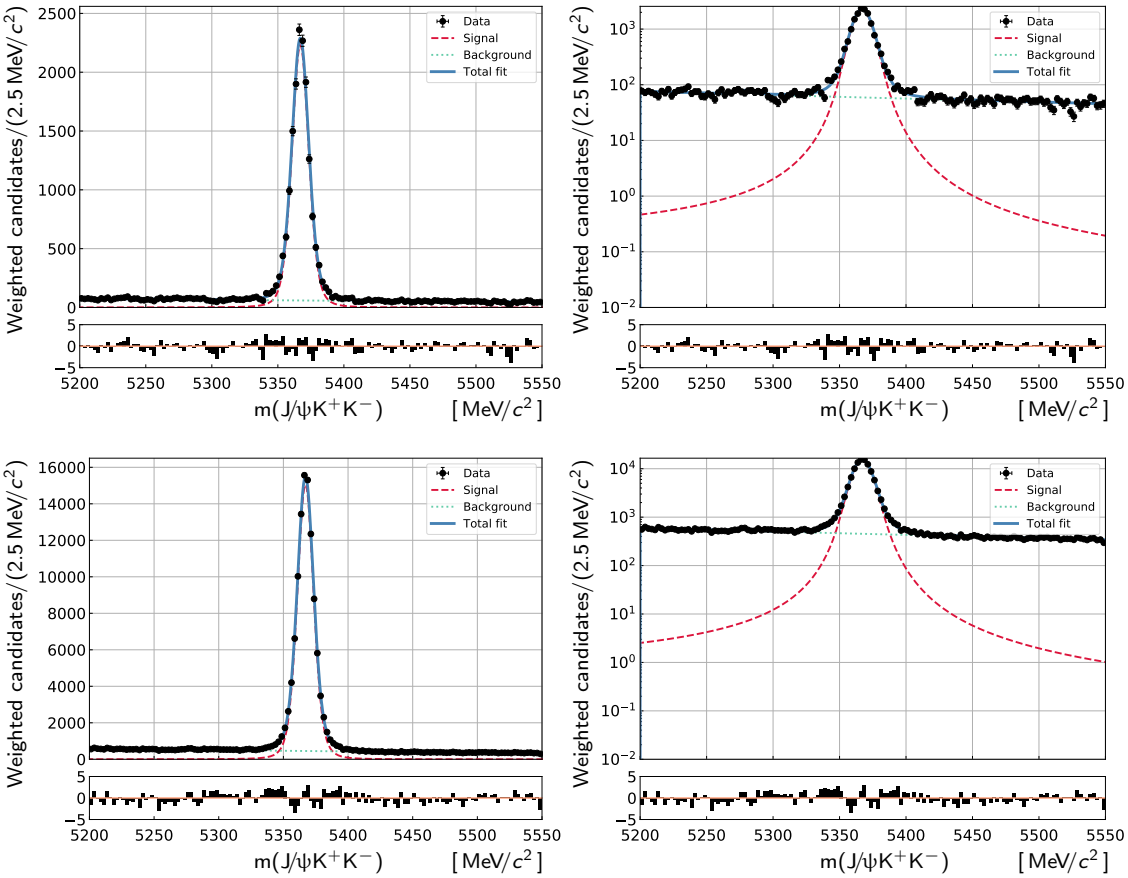

Figure 4.11: Fits to the m(J/ψK$^+$K$^-$) distribution in 2015 (top) and 2016 (bottom) data (solid blue line) and pull using a Crystal Ball shape for the signal (dashed blue line) and an exponential distribution for the background (dashed green line) in the full mass range (left) and in logarithmic scale (right).

are shown in figures 4.13, 4.14, 4.15 and 4.16.

The projections of the mass fits in three bins of cos(θ_μ) are shown in figure 4.12 for the entire data sample. Since the fit agrees very well, one can see that the observed correlation between the mass shape and cos(θ_μ) is now properly accounted for by the mass model, which uses the per-event mass uncertainty as conditional observable. By performing the mass fit in this way we implicitly assume that the shape of the invariant J/ψK$^+$K$^-$ mass is independent of the decay time and the other two helicity angles, cos(θ_K) and ϕ_h. A systematic uncertainty corresponding to this assumption is assigned, and the details of the corresponding procedure are summarised in Chapter 5.

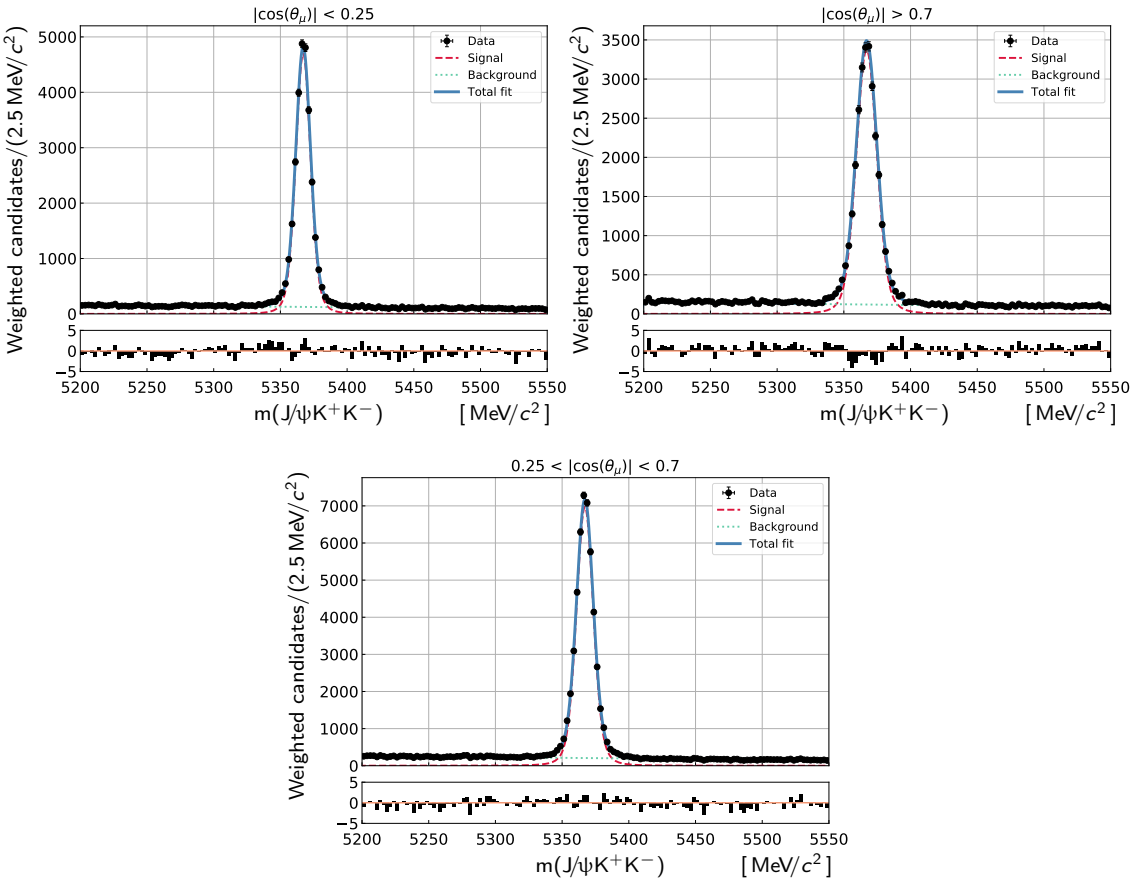

Figure 4.12: Projection of the total fit to the m $(J/\psi K^+K^-)$ distribution for data in the three $\cos(\theta_\mu)$ bins.

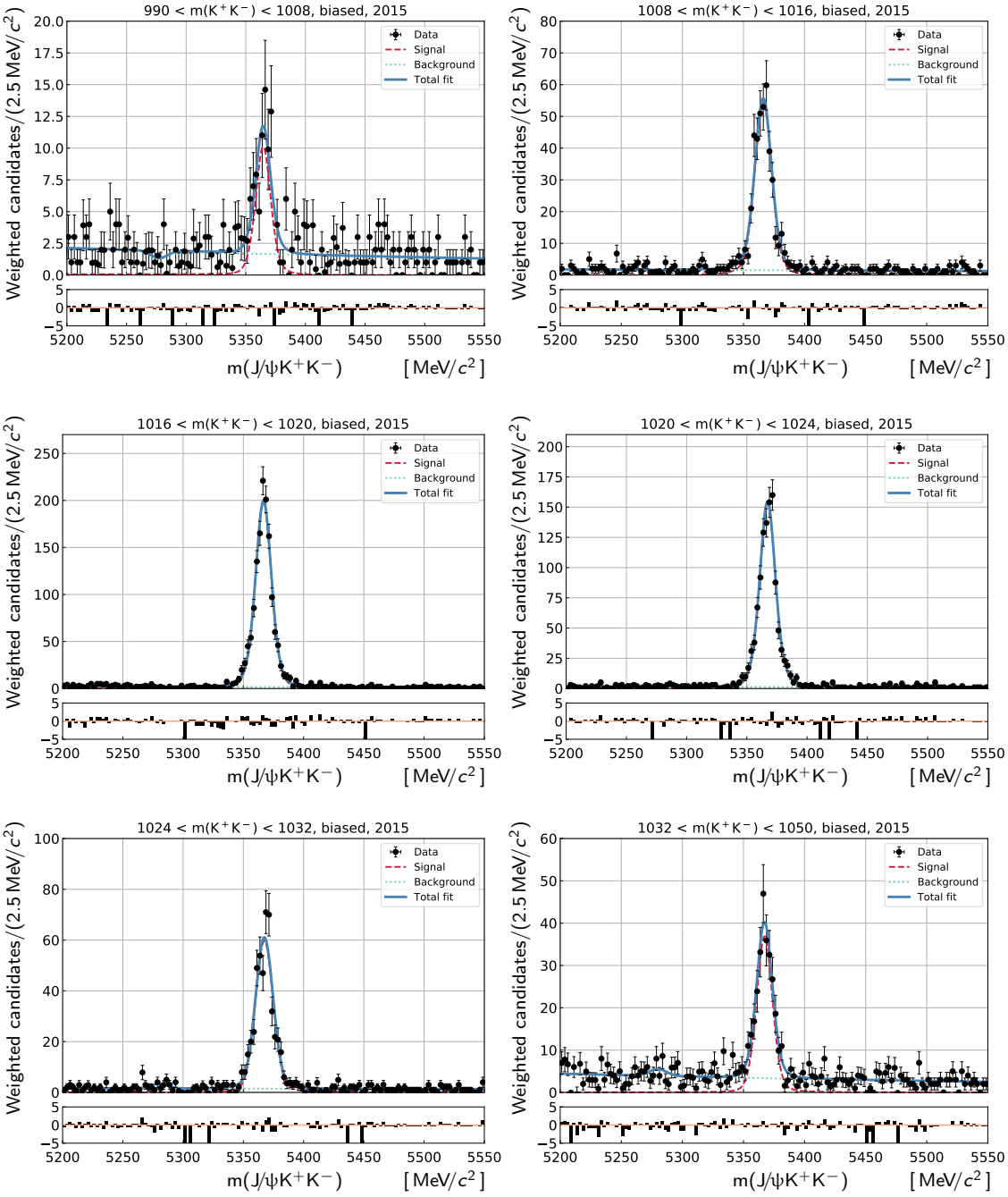

Figure 4.13: Fits to the $m(J/\psi K^+K^-)$ distribution divided into six bins in m_{KK}, namely [990, 1008, 1016, 1020, 1024, 1032, 1050] MeV/c^2, in the biased 2015 sample (solid blue line) and pull using a Crystal Ball shape for the signal (dashed blue line) and an exponential distribution for the background (dashed green line).

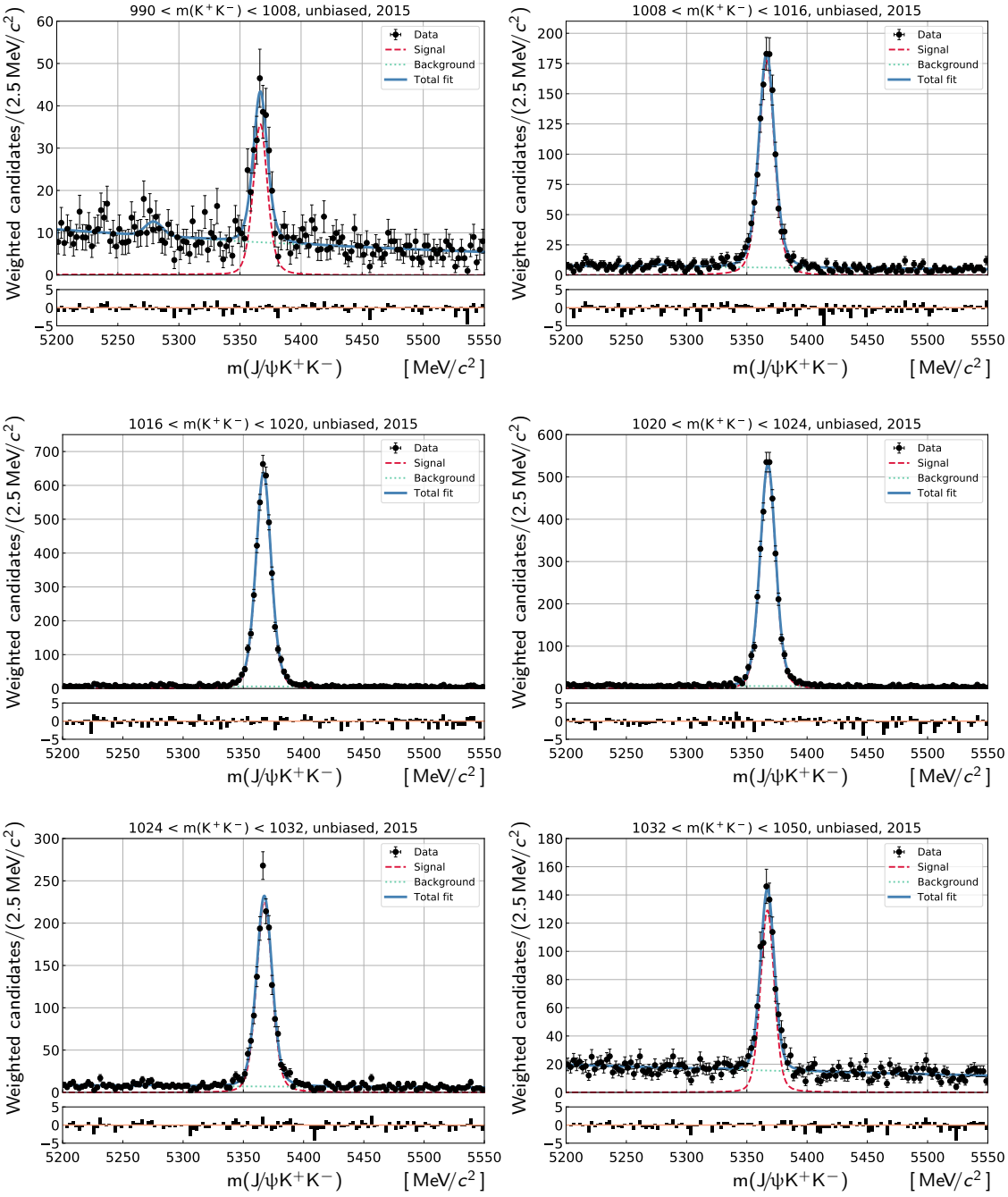

Figure 4.14: Fits to the $m(J/\psi K^+K^-)$ distribution divided into six bins in m_{KK}, namely [990, 1008, 1016, 1020, 1024, 1032, 1050] MeV/c^2, in the unbiased 2015 sample (solid blue line) and pull using a Crystal Ball shape for the signal (dashed blue line) and an exponential distribution for the background (dashed green line).

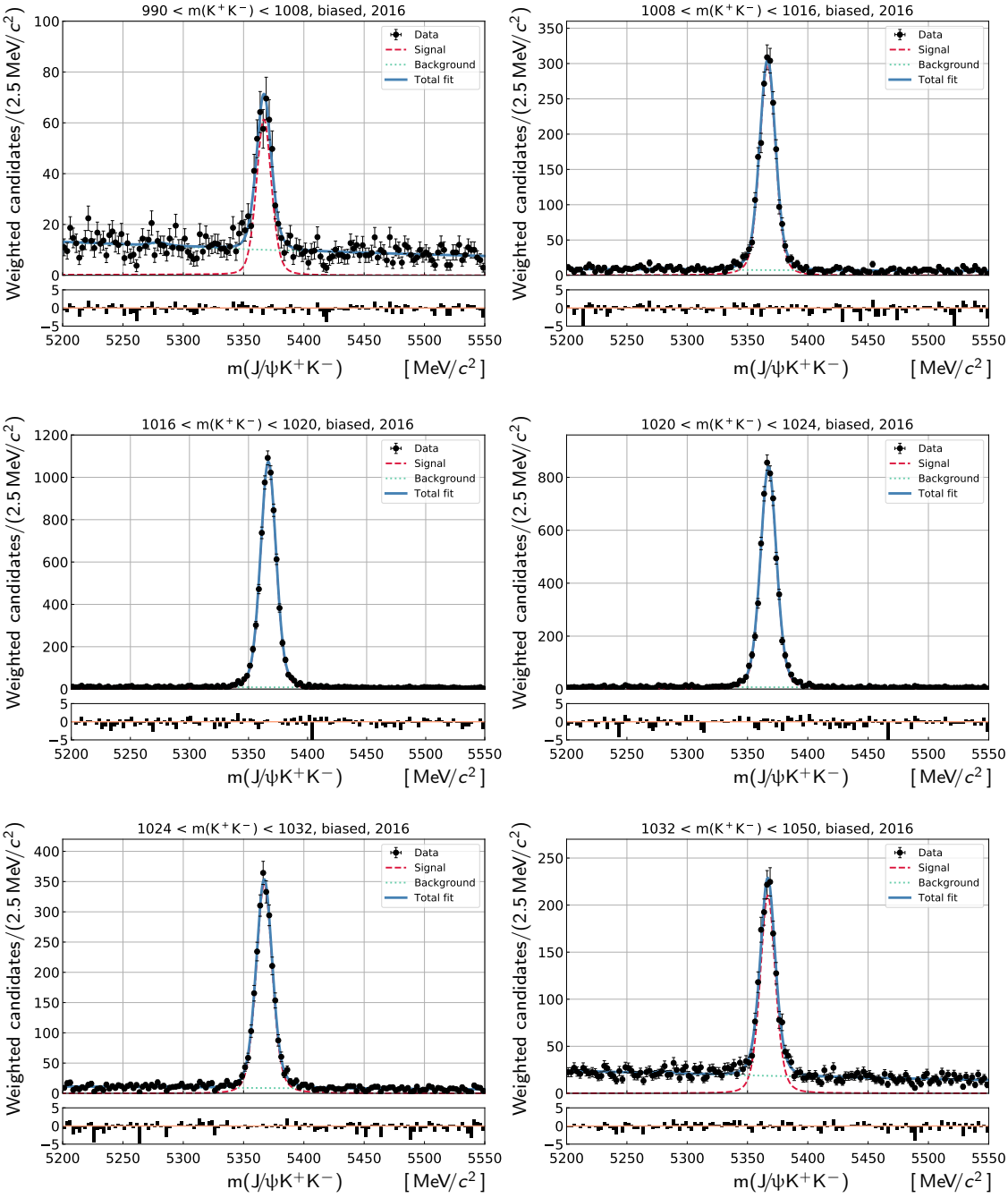

Figure 4.15: Fits to the $m(J/\psi K^+K^-)$ distribution divided into six bins in m_{KK}, namely [990, 1008, 1016, 1020, 1024, 1032, 1050] MeV/c^2, in the biased 2016 sample (solid blue line) and pull using a Crystal Ball shape for the signal (dashed blue line) and an exponential distribution for the background (dashed green line).

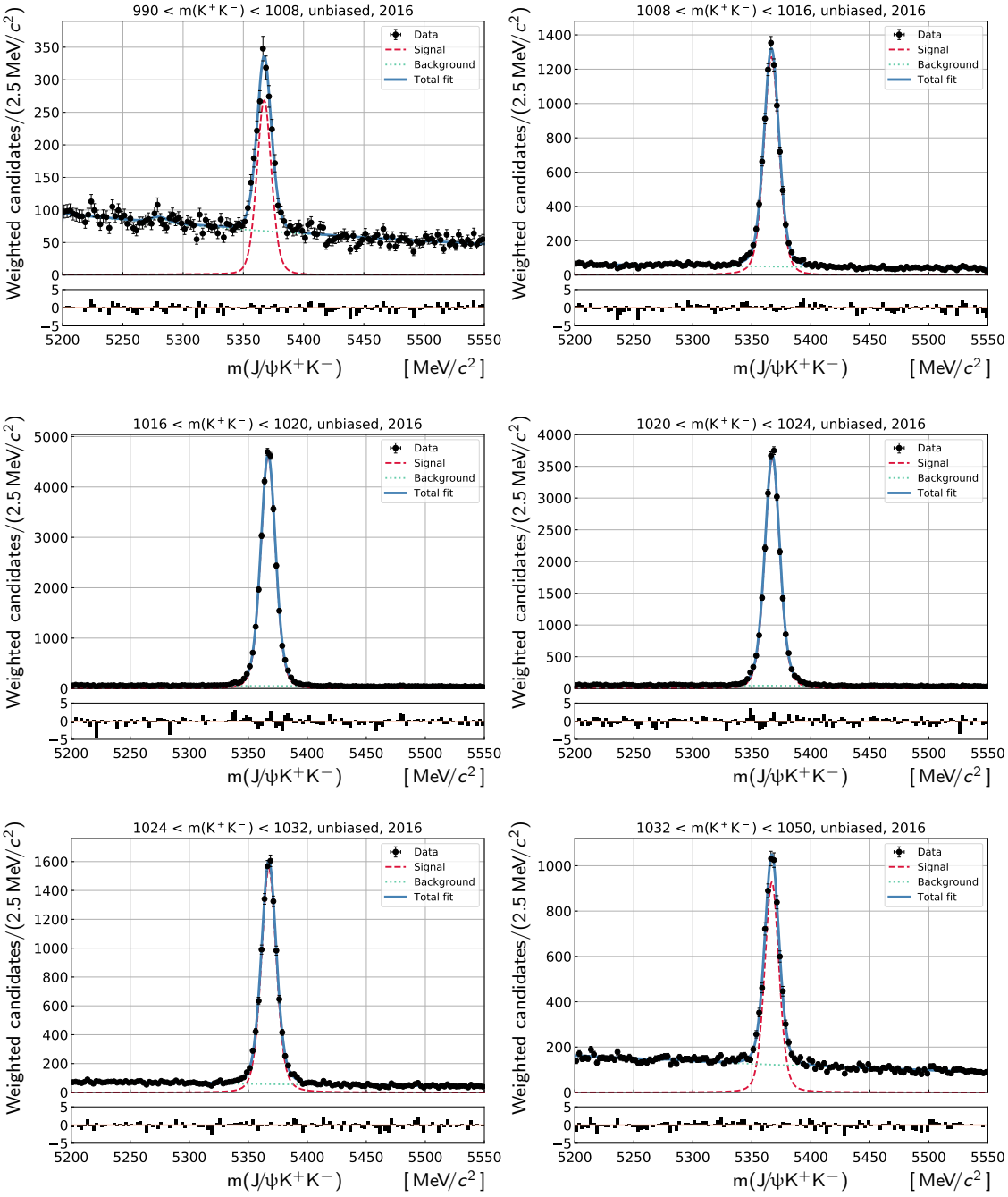

Figure 4.16: Fits to the $m(J/\psi K^+K^-)$ distribution divided into six bins in m_{KK}, namely [990, 1008, 1016, 1020, 1024, 1032, 1050] MeV/c^2, in the unbiased 2016 sample (solid blue line) and pull using a Crystal Ball shape for the signal (dashed blue line) and an exponential distribution for the background (dashed green line).

Table 4.1: Parameters from the mass fit to the biased (b) and unbiased (ub) 2015 and 2016 data sample performed in 6 m(KK) bins.

	Bin	N^{sig}	μ	s_1	s_2	N^{bkg}	f_{B_d}	γ_b
2015	1b	73 ± 11	5364.6 ± 1.0	0.71 ± 0.68	0.080 ± 0.120	227 ± 17	-0.018 ± 0.019	-0.0013 ± 0.0007
	2b	403 ± 22	5366.2 ± 0.4	1.22 ± 0.31	0.003 ± 0.050	210 ± 17	-0.009 ± 0.024	-0.0010 ± 0.0007
	3b	1382 ± 38	5366.7 ± 0.2	0.91 ± 0.18	0.052 ± 0.031	245 ± 18	-0.026 ± 0.017	-0.0031 ± 0.0007
	4b	1071 ± 34	5367.2 ± 0.2	0.82 ± 0.18	0.065 ± 0.031	197 ± 16	0.033 ± 0.027	-0.0009 ± 0.0008
	5b	461 ± 23	5367.4 ± 0.4	1.78 ± 0.14	-0.083 ± 0.017	212 ± 17	0.061 ± 0.029	-0.0006 ± 0.0008
	6b	257 ± 19	5367.2 ± 0.5	1.11 ± 0.36	0.015 ± 0.059	480 ± 24	0.024 ± 0.016	-0.0017 ± 0.0005
	1ub	237 ± 20	5366.7 ± 0.5	0.86 ± 0.47	0.050 ± 0.086	1111 ± 36	0.021 ± 0.011	-0.0019 ± 0.0003
	2ub	1269 ± 39	5366.5 ± 0.2	1.02 ± 0.16	0.034 ± 0.028	878 ± 33	0.012 ± 0.012	-0.0013 ± 0.0004
	3ub	4238 ± 67	5366.8 ± 0.1	0.92 ± 0.09	0.043 ± 0.015	870 ± 33	0.030 ± 0.012	-0.0011 ± 0.0004
	4ub	3554 ± 61	5367.5 ± 0.1	1.12 ± 0.09	0.009 ± 0.016	776 ± 32	-0.013 ± 0.010	-0.0019 ± 0.0004
	5ub	1570 ± 43	5367.4 ± 0.2	1.16 ± 0.13	0.004 ± 0.023	989 ± 35	0.011 ± 0.011	-0.0011 ± 0.0003
	6ub	804 ± 34	5367.1 ± 0.3	1.06 ± 0.20	0.001 ± 0.031	2166 ± 51	-0.001 ± 0.007	-0.0014 ± 0.0002
2016	1b	429 ± 26	5366.9 ± 0.4	0.93 ± 0.26	0.048 ± 0.047	1413 ± 42	0.006 ± 0.009	-0.0015 ± 0.0003
	2b	2130 ± 49	5366.7 ± 0.2	1.22 ± 0.13	-0.002 ± 0.023	1043 ± 37	0.014 ± 0.011	-0.0011 ± 0.0003
	3b	7371 ± 88	5366.8 ± 0.1	1.19 ± 0.07	0.000 ± 0.011	1159 ± 39	-0.003 ± 0.009	-0.0015 ± 0.0003
	4b	5856 ± 78	5367.4 ± 0.1	1.01 ± 0.08	0.036 ± 0.014	999 ± 36	0.018 ± 0.011	-0.0010 ± 0.0003
	5b	2494 ± 53	5367.2 ± 0.2	0.98 ± 0.13	0.044 ± 0.022	1235 ± 40	0.001 ± 0.009	-0.0016 ± 0.0003
	6b	1450 ± 45	5366.8 ± 0.2	0.63 ± 0.13	0.100 ± 0.022	2616 ± 57	0.005 ± 0.006	-0.0015 ± 0.0002
	1ub	1803 ± 57	5367.3 ± 0.2	1.09 ± 0.17	0.014 ± 0.029	9580 ± 110	0.006 ± 0.003	-0.0019 ± 0.0001
	2ub	8890 ± 100	5366.7 ± 0.1	1.09 ± 0.07	0.019 ± 0.012	6985 ± 93	0.009 ± 0.004	-0.0013 ± 0.0001
	3ub	30610 ± 180	5366.8 ± 0.1	1.02 ± 0.03	0.024 ± 0.006	7118 ± 94	0.001 ± 0.004	-0.0014 ± 0.0001
	4ub	24590 ± 160	5367.4 ± 0.1	0.99 ± 0.04	0.032 ± 0.006	6321 ± 89	0.007 ± 0.004	-0.0013 ± 0.0001
	5ub	10640 ± 110	5367.4 ± 0.1	0.99 ± 0.06	0.034 ± 0.010	8046 ± 100	0.003 ± 0.004	-0.0017 ± 0.0001
	6ub	6119 ± 95	5367.0 ± 0.1	1.00 ± 0.08	0.026 ± 0.014	17180 ± 140	0.001 ± 0.002	-0.0017 ± 0.0001

4.3 Decay time

In the LHCb detector a typical B_s^0 meson flies approximately 1 cm prior to its decay. The decay time, t, is then obtained from the measured momentum of the B_s^0 meson and its flight distance

$$t = \frac{m\,l}{p} \tag{4.12}$$

where l is the B_s^0 meson flight distance, p and m are the magnitude of its momentum and mass.

Some of the selection criteria explained in section 4.1, in particular those that explicitly require track displacement from the PV are called decay-time biasing since they introduce a non-uniform efficiency as a function of the decay time. The shape of the acceptance has to be modelled correctly to produce an accurate determination of any parameter which depends on the observed distribution of the decay time. Details on the acceptance determination are given in section 4.3.1.

The measurement of the decay time is affected by the resolution of the detector that dilutes any time-dependent asymmetry with a damping factor $e^{-\frac{\sigma_t{}^2 \Delta m^2}{2}}$ [73] and therefore has to be precisely studied. The decay time uncertainty is estimated on a event-by-event basis from the track fit and is usually underestimated since it does not include all possible detector effects. The estimated decay-time uncertainty thus requires calibration, and the details of the calibration procedure are given in section 4.3.3.

4.3.1 Acceptance

The displacement requirements on signal tracks introduced by the trigger reduce large amounts of background events, but at the same time introduce a non-trivial acceptance shape as function of decay time for lower lifetimes (around < 5 ps). A slight inefficiency at larger decay times (> 5 ps) is caused by reconstruction effect because tracks with large impact parameter with respect to the beam line are not fully efficiently reconstructed [86]. Both effects introduce a non-uniform acceptance as a function of decay time and thus have to be taken into account in the final fit. The shape of the acceptance is determined by studying $B^0 \to J/\psi K^{*0}$ ($K^{*0} \to K^+\pi^-$) decays, which are kinematically similar to the signal channel. The decay time distribution of these B^0 decays follows a pure exponential shape, since the decay-width difference, $\Delta\Gamma_d$, in the $B^0 - \overline{B}^0$ system is measured to be consistent with zero [7]. This method allows to correct simultaneously for both effects.

To describe the acceptance shape, cubic splines are used. A spline is a positive definite smooth function which makes it suitable for describing an efficiency. Moreover, the integrals of the exponential decay time distributions multiplied with a cubic spline can be evaluated analytically, as shown in reference [87], which is crucial for the PDF normalisation. The key properties of splines, and decay-time integrals including these splines are discussed in section 4.3.2.

The measured acceptance of the B^0 decay time is multiplied by the ratio of acceptances obtained from simulation, to correct for differences between the signal and control channels as

$$\varepsilon^{B^0_s}_{data}(t) = \varepsilon^{B^0}_{data}(t) \times \frac{\varepsilon^{B^0_s}_{sim}(t)}{\varepsilon^{B^0}_{sim}(t)}\,, \tag{4.13}$$

where $\varepsilon^{B^0}_{data}(t)$ is the efficiency of the control channel and $\varepsilon^{B^0_s}_{sim}(t)/\varepsilon^{B^0}_{sim}(t)$ is the ratio of efficiencies of the simulated signal and the simulated control channels after reconstruction and selection. For the $B^0_s \to J/\psi K^+K^-$ decay mode, a special sample is simulated with $\Delta\Gamma_s$ set to zero to simplify the extraction of the decay-time acceptance from simulated data. The PDF used to describe the decay-time distribution of the B^0 data, and of the B^0_s and B^0 simulated samples is composed of a single exponential function multiplied with the efficiency function, convolved with a single Gaussian resolution function centered at zero. The selection for the control channel $B^0 \to J/\psi K^{*0}$ closely follows the selection for the signal mode. To further increase the similarity between the signal and control channels, the kinematic distributions, i.e. p and p_T, of the B^0 meson in the $B^0 \to J/\psi K^{*0}$ data sample are matched to those of the B^0_s meson in the $B^0_s \to J/\psi K^+K^-$ data sample. Furthermore, both the B^0 and B^0_s simulated samples are weighted to match the kinematic distributions in the corresponding data samples. The simulated samples are also corrected according to the PDF ratio with respect to data with parameters found in reference [88, 89] to match the observed admixture of P- and S- waves in the $K^+\pi^-$ and K^+K^- final states.

The ratio of the B^0 to B^0_s efficiencies in simulation is parametrised as a spline, $s^{B^0/B^0_s}_{sim}$. Another spline is used to describe the acceptance found in the simulated $B^0_s \to J/\psi K^+K^-$ sample, $s^{B^0_s}_{sim}$, and the acceptance observed in the simulated $B^0 \to J/\psi K^{*0}$ sample is then described with $s^{B^0/B^0_s}_{sim} \times s^{B^0_s}_{sim}$. A third spline is used for the efficiency of the signal channel, $s^{B^0_s}_{data}$ and following equation 4.13, the acceptance in the $B^0 \to J/\psi K^{*0}$ data sample is parametrised by $s^{B^0_s}_{data} \times s^{B^0/B^0_s}_{sim}$. This allows the extraction of the overall uncertainties on the B^0_s data spline coefficients, which in turn allow for the determination of the related systematic uncertainty by varying them within their correlated uncertainties. Both for the B^0 simulation and the data a product of two splines is used to describe the acceptance shape. As a result, the computation of the integrals where the acceptance is represented by a product of two splines is required. The corresponding mathematical implementation is presented in section 4.3.2. The determination of the B^0_s data acceptance spline is repeated separately for 2015 and 2016, and the two trigger categories, i.e. biased and almost unbiased. The obtained splines are shown in figure 4.17.

Method validation

The procedure to extract the decay-time acceptance is validated using two B meson control samples of known lifetime. A test is performed using the $B^0 \to J/\psi K^{*0}$ decays both as the signal and the control modes. If the method to access the decay-time acceptance, described above, is valid then a null decay-width difference is measured

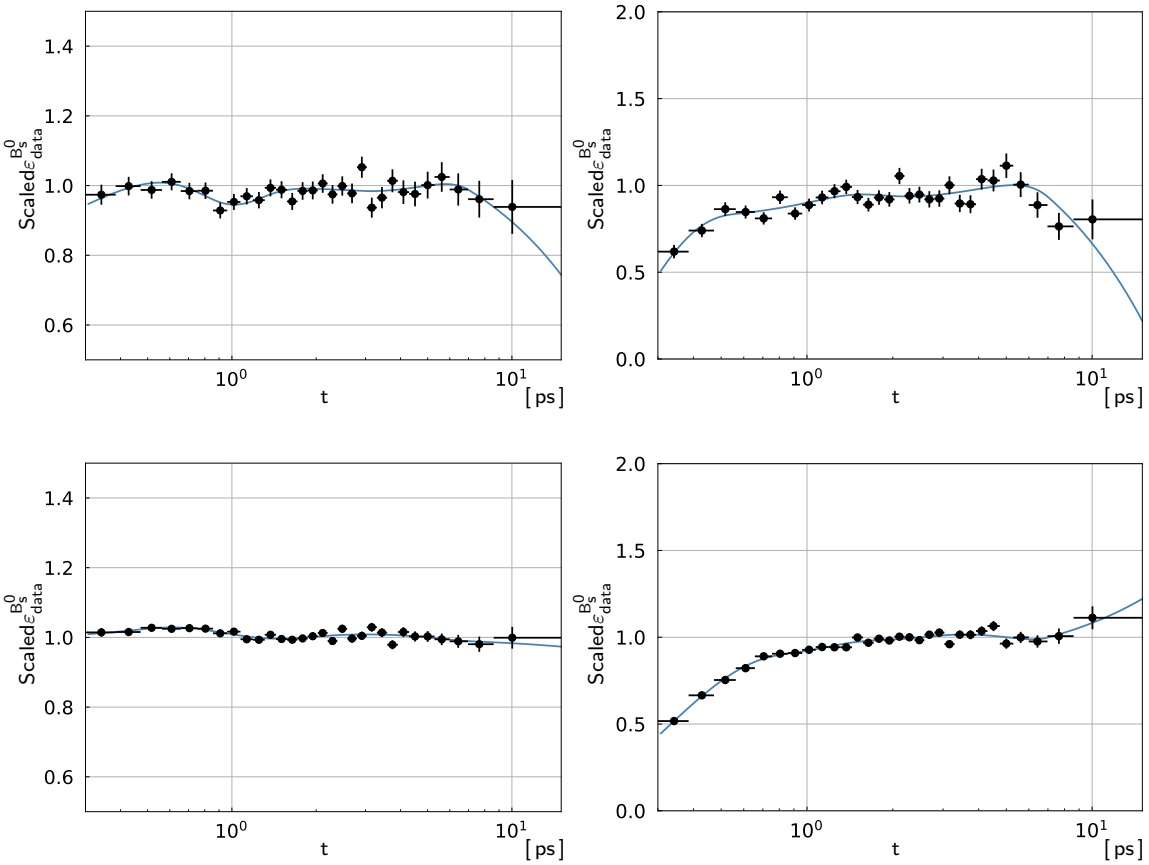

Figure 4.17: Decay-time efficiency for the unbiased (left) and biased (right) 2015 (top) and 2016 (bottom) $B_s^0 \to J/\psi K^+K^-$ data sample. The cubic spline function is shown with the blue line. For comparison the black points show the efficiency computed using histograms.

in the test. In order to do the test on the $B^0 \to J/\psi K^{*0}$ sample, it is split into two independent sets according to different selection criteria. One subsample is used as the signal and the other as control sample. The measured decay-width difference is found to be consistent with zero with a precision around $0.003\,\text{ps}^{-1}$.

Another test is performed with a data sample of around 1.6 million $B^+ \to J/\psi K^+$ candidates with $J/\psi \to \mu^+\mu^-$ with selection requirements similar to the signal mode. The ratio of the B^+ and B^0 decay widths, Γ_u/Γ_d, is measured. A simulated sample of B^+ decays is used in the calculation of the numerator of equation 4.13. This sample is corrected to match kinematic distributions in data. The measured ratio of decay widths is measured to be $\Gamma_u/\Gamma_d = 0.9276 \pm 0.0022$, where the uncertainty is only statistical. This is in a good agreement with the the world average value 0.9294 ± 0.0035 [7]. This test validates the measurement of Γ_s/Γ_d with a precision of 0.4%.

4.3.2 Cubic splines

A cubic spline, $S(x)$, is defined as a linear combination of so-called basis splines (b-splines), $S_i(x)$, on n consecutive intervals between a and b, $a = t_0 < t_1 < \cdots < t_n = b$, such that

$$S(x) = \begin{cases} S_0(x) = d_0 \left(\frac{x-t_0}{t_1-t_0} - a_0\right)\left(\frac{x-t_0}{t_1-t_0} - b_0\right)\left(\frac{x-t_0}{t_1-t_0} - c_0\right), \ t_0 < x < t_1 \\ \dots \\ S_{n-1}(x) = d_{n-1} \left(\frac{x-t_{n-1}}{t_n-t_{n-1}} - a_{n-1}\right)\left(\frac{x-t_{n-1}}{t_n-t_{n-1}} - b_{n-1}\right)\left(\frac{x-t_{n-1}}{t_n-t_{n-1}} - c_{n-1}\right), \\ t_{n-1} < x < t_n \end{cases} \tag{4.14}$$

where $S_i(x)$ are third-order polynomials defined between the two knot positions t_i and t_{i+1}. Continuity requires that the b-splines values at the knot positions, together with the first and second derivatives are equal

$$\begin{cases} S_{i-1}(x_i) = S_i(x_i) \\ S'_{i-1}(x_i) = S'_i(x_i) \\ S''_{i-1}(x_i) = S''_i(x_i) \end{cases} \tag{4.15}$$

where $i = 1, 2, \dots, n-1$. These continuity requirements, together with the requirement that b-splines form a partition of unity, i.e.

$$\sum_i S_i(x) = 1, \tag{4.16}$$

fully define a set of b-splines for a given vector of knots. In figure 4.18 an example of a cubic spline is shown together with the b-splines from which it is constructed.

The normalisation of the PDF, introduced in the beginning of Chapter 4, requires the computation of integrals with terms $a(\mathrm{t})f(\mathrm{t})$, where $a(\mathrm{t})$ is the acceptance function and $f(\mathrm{t})$ is time-dependent part of the PDF. For the case when $a(\mathrm{t})$ is represented as a cubic b-spline, the term for the each interval can be written as

$$\begin{aligned} h_i(\mathrm{t}) &= (\mathrm{t} - \alpha_i)(\mathrm{t} - \beta_i)(\mathrm{t} - \gamma_i) f(\mathrm{t}) \\ &= \left(\mathrm{t}^3 - (\alpha_i + \beta_i + \gamma_i)\mathrm{t}^2 + (\beta_i\gamma_i + \alpha_i\gamma_i + \alpha_i\beta_i)\mathrm{t} - \alpha_i\beta_i\gamma_i\right) f(\mathrm{t}). \end{aligned} \tag{4.17}$$

This spline parametrisation is chosen such that the α, β and γ parameters have the same units which improves numerical stability. The corresponding integral is given in reference [87]. The case described in the reference has to be extended for the case that the efficiency is described by the product of two cubic splines. The integral term

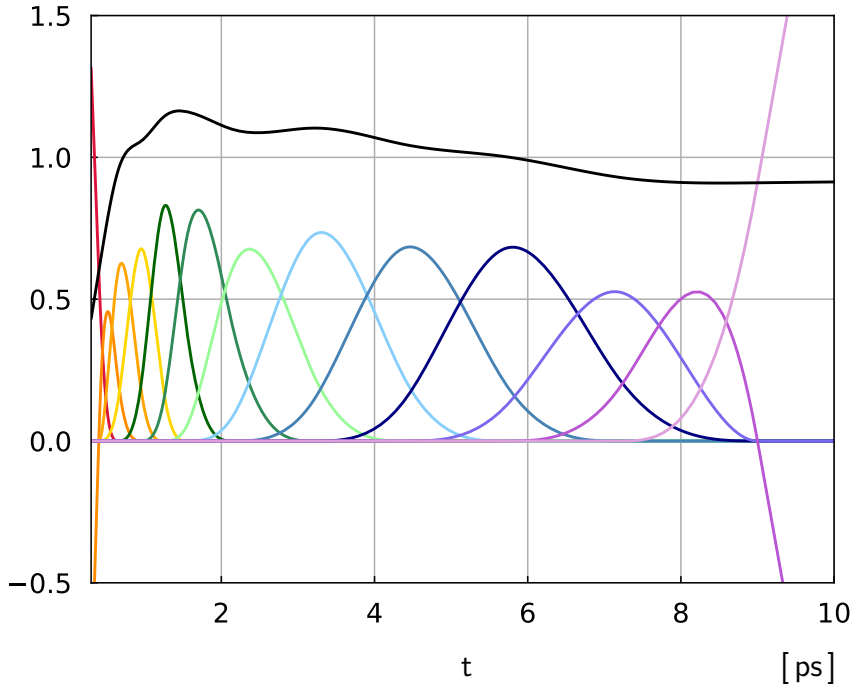

Figure 4.18: Example of a cubic spline (black line). Colourful lines show the b-splines from which the cubic spline is build.

becomes more complicated and can be denoted as follows

$$
\begin{aligned}
h_i(t) &= (t-\alpha_{1i})(t-\beta_{1i})(t-\gamma_{1i}) \times (t-\alpha_{2i})(t-\beta_{2i})(t-\gamma_{2i}) f(t) \qquad (4.18)\\
&= \Big[t^6 - [(\alpha_{1i}+\beta_{1i}+\gamma_{1i}) + (\alpha_{2i}+\beta_{2i}+\gamma_{2i})]t^5 \\
&+ [(\beta_{1i}\gamma_{1i} + \alpha_{1i}\gamma_{1i} + \alpha_{1i}\beta_{1i}) + (\beta_{2i}\gamma_{2i} + \alpha_{2i}\gamma_{2i} + \alpha_{2i}\beta_{2i}) \\
&+ (\alpha_{1i}+\beta_{1i}+\gamma_{1i})(\alpha_{2i}+\beta_{2i}+\gamma_{2i})]t^4 \\
&- [\alpha_{1i}\beta_{1i}\gamma_{1i} + (\alpha_{1i}+\beta_{1i}+\gamma_{1i})(\beta_{2i}\gamma_{2i} + \alpha_{2i}\gamma_{2i} + \alpha_{2i}\beta_{2i}) \\
&+ \alpha_{2i}\beta_{2i}\gamma_{2i} + (\alpha_{2i}+\beta_{2i}+\gamma_{2i})(\beta_{1i}\gamma_{1i} + \alpha_{1i}\gamma_{1i} + \alpha_{1i}\beta_{1i})]t^3 \\
&+ [(\alpha_{1i}+\beta_{1i}+\gamma_{1i})\alpha_{2i}\beta_{2i}\gamma_{2i} + (\alpha_{2i}+\beta_{2i}+\gamma_{2i})\alpha_{1i}\beta_{1i}\gamma_{1i} \\
&+ (\beta_{1i}\gamma_{1i} + \alpha_{1i}\gamma_{1i} + \alpha_{1i}\beta_{1i})(\beta_{2i}\gamma_{2i} + \alpha_{2i}\gamma_{2i} + \alpha_{2i}\beta_{2i})]t^2 \\
&- [\alpha_{2i}\beta_{2i}\gamma_{2i}(\beta_{1i}\gamma_{1i} + \alpha_{1i}\gamma_{1i} + \alpha_{1i}\beta_{1i}) + \alpha_{1i}\beta_{1i}\gamma_{1i}(\beta_{2i}\gamma_{2i} + \alpha_{2i}\gamma_{2i} + \alpha_{2i}\beta_{2i})]t \\
&+ \alpha_{1i}\beta_{1i}\gamma_{1i}\alpha_{2i}\beta_{2i}\gamma_{2i}\Big] f(t)
\end{aligned}
$$

The method described in reference [87] can be extended to include higher orders and the corresponding normalisation integrals can be written using the generalised

product rule as

$$
\begin{aligned}
I_4(x_{\min}, x_{\max}; z) &= \begin{pmatrix} M_0(x;z) \\ M_1(x;z) \\ M_2(x;z) \\ M_3(x;z) \\ M_4(x;z) \end{pmatrix} \cdot \begin{pmatrix} 0 & 0 & 0 & 0 & \frac{1}{16} \\ 0 & 0 & 0 & \frac{1}{4} & 0 \\ 0 & 0 & \frac{3}{8} & 0 & 0 \\ 0 & \frac{1}{4} & 0 & 0 & 0 \\ \frac{1}{16} & 0 & 0 & 0 & 0 \end{pmatrix} \begin{pmatrix} K_0(z) \\ K_1(z) \\ K_2(z) \\ K_3(z) \\ K_4(z) \end{pmatrix} \\
&= \sum_{i=0}^{4} M_i K_{4-i} \begin{pmatrix} 4 \\ i \end{pmatrix} 2^{-4} \qquad (4.19)
\end{aligned}
$$

$$
\begin{aligned}
I_5(x_{\min}, x_{\max}; z) &= \begin{pmatrix} M_0(x;z) \\ M_1(x;z) \\ M_2(x;z) \\ M_3(x;z) \\ M_4(x;z) \\ M_5(x;z) \end{pmatrix} \cdot \begin{pmatrix} 0 & 0 & 0 & 0 & 0 & \frac{1}{32} \\ 0 & 0 & 0 & 0 & \frac{5}{32} & 0 \\ 0 & 0 & 0 & \frac{5}{16} & 0 & 0 \\ 0 & 0 & \frac{5}{16} & 0 & 0 & 0 \\ 0 & \frac{5}{32} & 0 & 0 & 0 & 0 \\ \frac{1}{32} & 0 & 0 & 0 & 0 & 0 \end{pmatrix} \begin{pmatrix} K_0(z) \\ K_1(z) \\ K_2(z) \\ K_3(z) \\ K_4(z) \\ K_5(z) \end{pmatrix} \\
&= \sum_{i=0}^{5} M_i K_{5-i} \begin{pmatrix} 5 \\ i \end{pmatrix} 2^{-5} \qquad (4.20)
\end{aligned}
$$

$$
\begin{aligned}
I_6(x_{\min}, x_{\max}; z) &= \begin{pmatrix} M_0(x;z) \\ M_1(x;z) \\ M_2(x;z) \\ M_3(x;z) \\ M_4(x;z) \\ M_5(x;z) \\ M_6(x;z) \end{pmatrix} \cdot \begin{pmatrix} 0 & 0 & 0 & 0 & 0 & 0 & \frac{1}{64} \\ 0 & 0 & 0 & 0 & 0 & \frac{3}{32} & 0 \\ 0 & 0 & 0 & 0 & \frac{15}{64} & 0 & 0 \\ 0 & 0 & 0 & \frac{5}{16} & 0 & 0 & 0 \\ 0 & 0 & \frac{15}{64} & 0 & 0 & 0 & 0 \\ 0 & \frac{3}{32} & 0 & 0 & 0 & 0 & 0 \\ \frac{1}{64} & 0 & 0 & 0 & 0 & 0 & 0 \end{pmatrix} \begin{pmatrix} K_0(z) \\ K_1(z) \\ K_2(z) \\ K_3(z) \\ K_4(z) \\ K_5(z) \\ K_6(z) \end{pmatrix} . \\
&= \sum_{i=0}^{6} M_i K_{6-i} \begin{pmatrix} 6 \\ i \end{pmatrix} 2^{-6} \qquad (4.21)
\end{aligned}
$$

Therefore, the corresponding normalisation of the product of two cubic b-spines multiplied with $f(\mathrm{t})$ can be written as a linear combination of I_n:

$$
\sum_{j=0}^{6} \sum_{k=0}^{6-j} \left(M_j(x_{i+1}; z) - M_j(x_i; z) \right) S_{jk}(\alpha_{1i}, \beta_{1i}, \gamma_{1i}, \alpha_{2i}, \beta_{2i}, \gamma_{2i}) K_k(z) \qquad (4.22)
$$

In case of the product of two splines, the matrix S_{jk} becomes more complicated than for a single spline:

$$
\begin{pmatrix}
\mathrm{coef}(\mathrm{t}^0) & \frac{\mathrm{coef}(\mathrm{t}^1)}{2} & \frac{\mathrm{coef}(\mathrm{t}^2)}{4} & \frac{\mathrm{coef}(\mathrm{t}^3)}{8} & \frac{\mathrm{coef}(\mathrm{t}^4)}{16} & \frac{\mathrm{coef}(\mathrm{t}^5)}{32} & \frac{1}{64} \\
\frac{\mathrm{coef}(\mathrm{t}^1)}{2} & \frac{\mathrm{coef}(\mathrm{t}^2)}{2} & \frac{3\mathrm{coef}(\mathrm{t}^3)}{8} & \frac{\mathrm{coef}(\mathrm{t}^4)}{4} & \frac{5\mathrm{coef}(\mathrm{t}^5)}{32} & \frac{3}{32} & 0 \\
\frac{\mathrm{coef}(\mathrm{t}^2)}{4} & \frac{3\mathrm{coef}(\mathrm{t}^3)}{8} & \frac{3\mathrm{coef}(\mathrm{t}^4)}{8} & \frac{5\mathrm{coef}(\mathrm{t}^5)}{16} & \frac{15}{64} & 0 & 0 \\
\frac{\mathrm{coef}(\mathrm{t}^3)}{8} & \frac{\mathrm{coef}(\mathrm{t}^4)}{4} & \frac{5\mathrm{coef}(\mathrm{t}^5)}{16} & \frac{5}{16} & 0 & 0 & 0 \\
\frac{\mathrm{coef}(\mathrm{t}^4)}{16} & \frac{5\mathrm{coef}(\mathrm{t}^5)}{32} & \frac{15}{64} & 0 & 0 & 0 & 0 \\
\frac{\mathrm{coef}(\mathrm{t}^5)}{32} & \frac{3}{32} & 0 & 0 & 0 & 0 & 0 \\
\frac{1}{64} & 0 & 0 & 0 & 0 & 0 & 0
\end{pmatrix} \qquad (4.23)
$$

The coef(t^n) represent the coefficients appearing in front of the corresponding power n of t, and which are shown in the equation 4.19. The equations shown above are used in the evaluation of the decay time acceptance.

4.3.3 Resolution

The uncertainty on the decay-time measurement, σ_t, is propagated from the uncertainty on the measurement of the flight distance, σ_L, and of the B_s^0 momentum, σ_p, as

$$\sigma_t^2 = \left(\frac{m}{p}\right)^2 \sigma_L^2 + \left(\frac{t}{p}\right)^2 \sigma_p^2 \tag{4.24}$$

The main contribution to the decay-time resolution is σ_L. The decay-length measurement uncertainty is in turn dominated by the error on the measurement of the decay vertex of B_s^0 meson. The uncertainties, δ_t, are estimated on an event-by-event basis by propagating them from the underlying fit to the charged particle tracks. However, the δ_t is usually underestimated and thus has to be calibrated. This calibration is done using the so-called prompt sample, which is one of the background samples in the $B_s^0 \to J/\psi K^+K^-$ sample. These candidates are selected identically to the signal candidates, except no decay-time biasing selection criteria are applied.

The decay time of the prompt candidates is expected to be zero. If the measurement gives a non-zero value, this is mainly due to the detector resolution. By determining the spread in measured lifetimes of these prompt candidates one can determine the resolution. For the calibration procedure, the prompt sample is divided in eleven subsamples according to the value of δ_t. For each subsample, the resolution is determined.

The decay-time distribution of the prompt component is modelled with a Dirac delta function, convoluted with a resolution function that consists of three Gaussian distributions with a mean of zero and a width σ_i. A systematic uncertainty is assigned due to the assumption that the distribution of the resolution is centered at zero. An additional component of both short and long-lived candidates is used to model the contribution arising for positive decay times due to J/ψ mesons originating from the from decays of b hadrons. A double exponential component is added to the PDF to take this component into account, with decay time parameters of τ_s and τ_l, respectively. Another background component comes from wrong PV assignments, whose shape is obtained from a control sample in which the decay time is computed with respect to a primary vertex taken from a different event. The total PDF can be written as

$$\mathrm{PDF}(t|\sigma_t) = \mathcal{R}(t|\sigma_t) \otimes [N_{\mathrm{prompt}}\delta(t) + N_{ll}\left(f_{sl}e^{-t/\tau_s} + (1-f_{sl})e^{-t/\tau_l}\right)] + N_{wpv}W(t)$$

where N_{prompt} is the number of prompt J/ψ candidates, N_{ll} is the number of long-lived candidates, f_{sl} is the fraction of the long-lived background with the smaller lifetime, and N_{wpv} is the number of candidates which have been incorrectly associated to a PV. The resolution function, $\mathcal{R}(t)$, is the sum of three Gaussian distributions, each contributing with fraction f_i,

$$\mathcal{R}(t) = \sum_{i=1}^{3} f_i \frac{1}{\sqrt{2\pi}\sigma_i} \exp\left[-\frac{(t-\mu)^2}{2{\sigma_i}^2}\right], \tag{4.25}$$

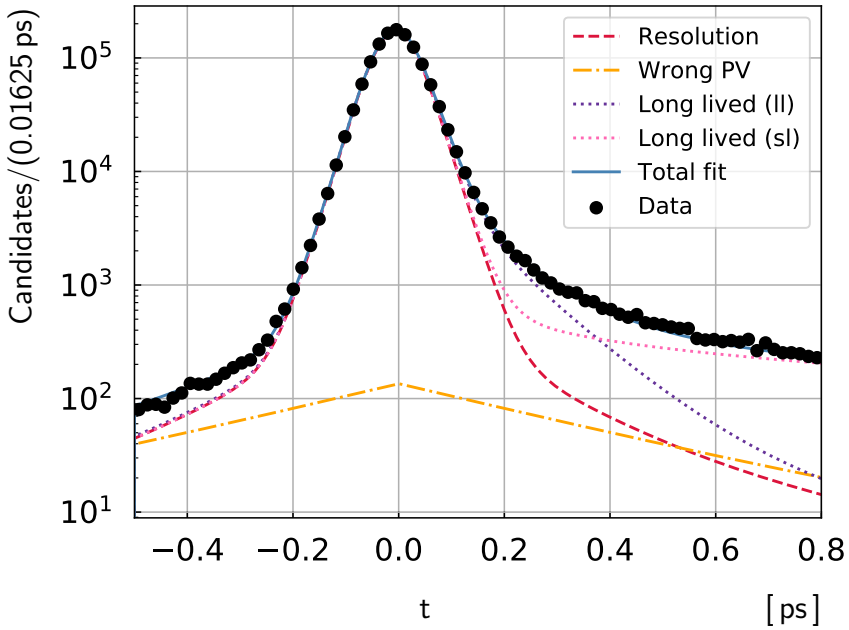

Figure 4.19: Decay-time distribution of the prompt $J/\psi K^+K^-$ calibration sample with the result of an unbinned maximum-likelihood fit overlaid in blue. The overall triple-Gaussian resolution is represented by the dashed red line, while the two long-lived and the wrong-PV components are shown by the dotted purple and pink lines and the long-dashed orange line, respectively.

with the constraint $\sum_i f_i = 1$. The dilution of the amplitude of the $B_s^0 - \overline{B}_s^0$ oscillation due to the resolution is then determined in each bin of δ_t as

$$\mathcal{D} = \sum_{i=1}^{3} f_i \exp\left[-{\sigma_i}^2 \Delta m_s^2/2\right], \tag{4.26}$$

and converted into an effective width of a single-Gaussian distribution

$$\sigma_{\text{eff}} = \sqrt{(-2/\Delta {m_s}^2)\ln \mathcal{D}} \tag{4.27}$$

where the value of Δm_s is fixed to 17.757 ps^{-1} [90]. The effective single-Gaussian resolution of width σ_{eff} introduces, by construction, the same damping effect on the magnitude of the B_s^0 meson oscillation as the resolution model that consists of three Gaussian functions. However, the use of a signal-Gaussian simplifies the procedure of evaluating the related systematic uncertainty.

The calibration curve is fitted with $\sigma_{\text{eff}}(\delta_t) = b_0 + b_1\delta_t$ and the calibration parameters, b_0 and b_1 are determined from the fit. The values obtained are $b_0 = 12.97 \pm 0.22$ fs and $b_1 = 0.846 \pm 0.006$.

The calibrated resolution averaged over the $B_s^0 \to J/\psi K^+K^-$ data sample is found to be $\sigma_{\text{eff}} = 45.54 \pm 0.04 \pm 0.05$ fs, where the first uncertainty is statistical, and the second is propagated from the uncertainties on the calibration parameters. This corresponds to a dilution $\mathcal{D} = 0.721 \pm 0.001$ assuming $\Delta m_s = 17.757 \pm 0.021\ \text{ps}^{-1}$ [90].

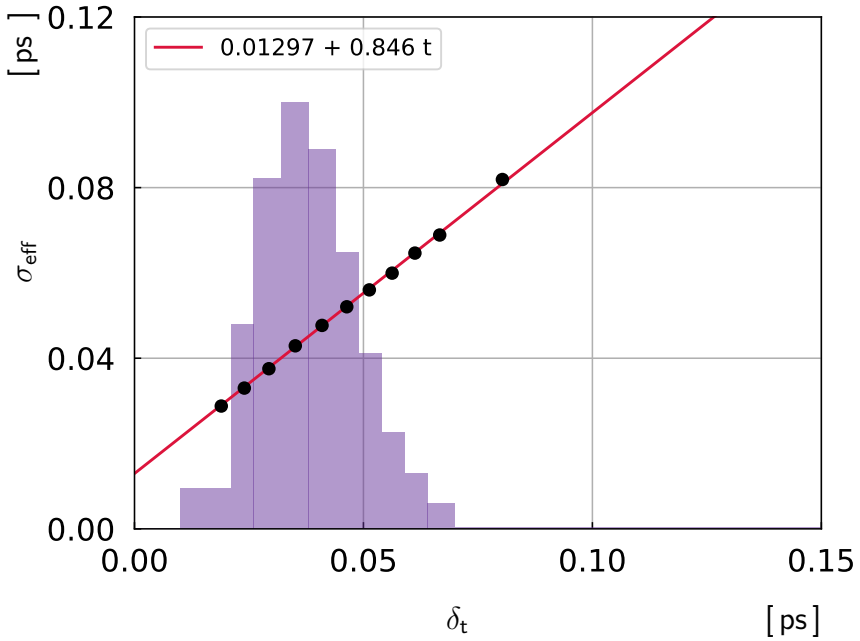

Figure 4.20: Variation of the effective single-Gaussian decay-time resolution, σ_{eff}, as a function of the estimated per-candidate decay-time uncertainty, δ_t, obtained from the prompt $J/\psi K^+K^-$ sample. The blue line shows the result when fitting a linear function. The shaded histogram shows the normalised distribution of δ_t in the background-subtracted $B_s^0 \to J/\psi K^+K^-$ sample. The data points are positioned at the barycentre of each δ_t bin.

4.4 Decay angles

To disentangle the contributions from different polarisation amplitudes, an angular analysis is performed. To describe the four-body system, three independent angles are required. The helicity formalism as shown in figure 1.4 is used to define these angles. Similar as for the decay time, the selection requirements together with the acceptance of the LHCb detector give rise to a non-uniform efficiency as a function of helicity angles. The three-dimensional angular-efficiency correction is discussed in section 4.4.1.

4.4.1 Acceptance

The acceptance function is evaluated on the simulated sample, separately for the two years of data taking, and two trigger categories. The simulation is corrected in a two-step procedure to match the data. The kinematic distributions, i.e. p_T, p of the B_s^0 meson, and m_{KK} are corrected to match the signal distributions in the data, using a boosted decision tree method [91]. A second step is required to correct the kinematic distributions of the final-state particles, and for the fact that the S-wave configuration of the K^+K^- pairs is not included in the simulated model. For this correction, an iterative weighting procedure is used which gradually matches the fraction of the S-wave contribution to the one in data. As a byproduct of this procedure, the matching of the

Table 4.2: Angular acceptance weights determined from all available simulated samples. The weights, used in the normalisation of the PDF are given with respect to the first weight f_k/f_1 separately for two years and for biased and unbiased trigger categories.

k		2015		2016	
		"Unbiased"	"Biased"	"Unbiased"	"Biased"
1	(00)	1 ± 0	1 ± 0	1 ± 0	1 ± 0
2	($\parallel\parallel$)	1.0270 ± 0.0019	1.0291 ± 0.0035	1.02497 ± 0.00065	1.02080 ± 0.00140
3	($\perp\perp$)	1.0270 ± 0.0018	1.0283 ± 0.0034	1.02469 ± 0.00064	1.02080 ± 0.00140
4	($\parallel\perp$)	-0.0019 ± 0.0015	-0.0096 ± 0.0029	-0.00063 ± 0.00052	0.00240 ± 0.00120
5	(0 $\parallel$)	0.0002 ± 0.0009	0.0039 ± 0.0017	0.00099 ± 0.00031	0.00321 ± 0.00067
6	(0 $\perp$)	0.0014 ± 0.0009	0.0020 ± 0.0017	0.00012 ± 0.00031	-0.00018 ± 0.00067
7	(SS)	1.0082 ± 0.0013	1.0137 ± 0.0024	1.00624 ± 0.00044	1.01130 ± 0.00100
8	(S$\parallel$)	-0.0007 ± 0.0011	-0.0033 ± 0.0022	0.00032 ± 0.00040	-0.00003 ± 0.00087
9	(S$\perp$)	0.0007 ± 0.0011	-0.0013 ± 0.0022	0.00024 ± 0.00041	-0.00003 ± 0.00088
10	(S0)	-0.0001 ± 0.0024	-0.0052 ± 0.0045	-0.00104 ± 0.00084	-0.00220 ± 0.00180

kinematic distributions of kaons in the simulation with respect to data is improved. The angular efficiency is included in the PDF through the normalisation weights, following the procedure described in reference [92]. The computation is done on the simulated sample, and the uncertainty due to the finite size of the simulated sample is propagated as a systematic uncertainty. The obtained normalisation weights are given in table 4.2. Projections of the angular efficiency for each of the three helicity angles are shown in figure 4.21.

Method validation

The procedure of assessing the angular acceptance is validated using two alternative samples. First, the $B^0 \to J/\psi K^{*0}$ data and simulation samples. The procedure described above for the signal mode is repeated: the simulation is corrected to match the kinematic distributions of the data using the iterative procedure and the normalisation weights are determined. The P- and S-wave polarisation amplitudes of the $B^0 \to J/\psi K^{*0}$ are measured by making an unbinned fit to the distribution of helicity angles of the final-state particles and found to be consistent with those in reference [88].

Another test is done using the large sample of $B^+ \to J/\psi K^+$ decays, described in section 4.3.1. The distribution for the helicity angle θ_μ in $B^+ \to J/\psi K^+$ decay is expected to exhibit a $1 - \cos^2\theta_\mu$ dependence. In order to check the large efficiency variation as a function of the pseudorapidity, the B^+ data sample is split into nine disjoint subsets according to the pseudorapidity of the B^+ meson. In each subset, the background subtraction is performed using the *sPlot* technique with the B^+ invariant mass as a discriminating variable. Prior to any angular acceptance correction, the distribution of the θ_μ angle in data shows approximately a 30% deviation from the expected shape. Using the normalisation weights evaluated on $B^+ \to J/\psi K^+$ simulation sample, the expected θ_μ distribution is recovered in each bin, with an overall precision of about 0.1%. The test is stable against variation of the splitting of the B^+ sample

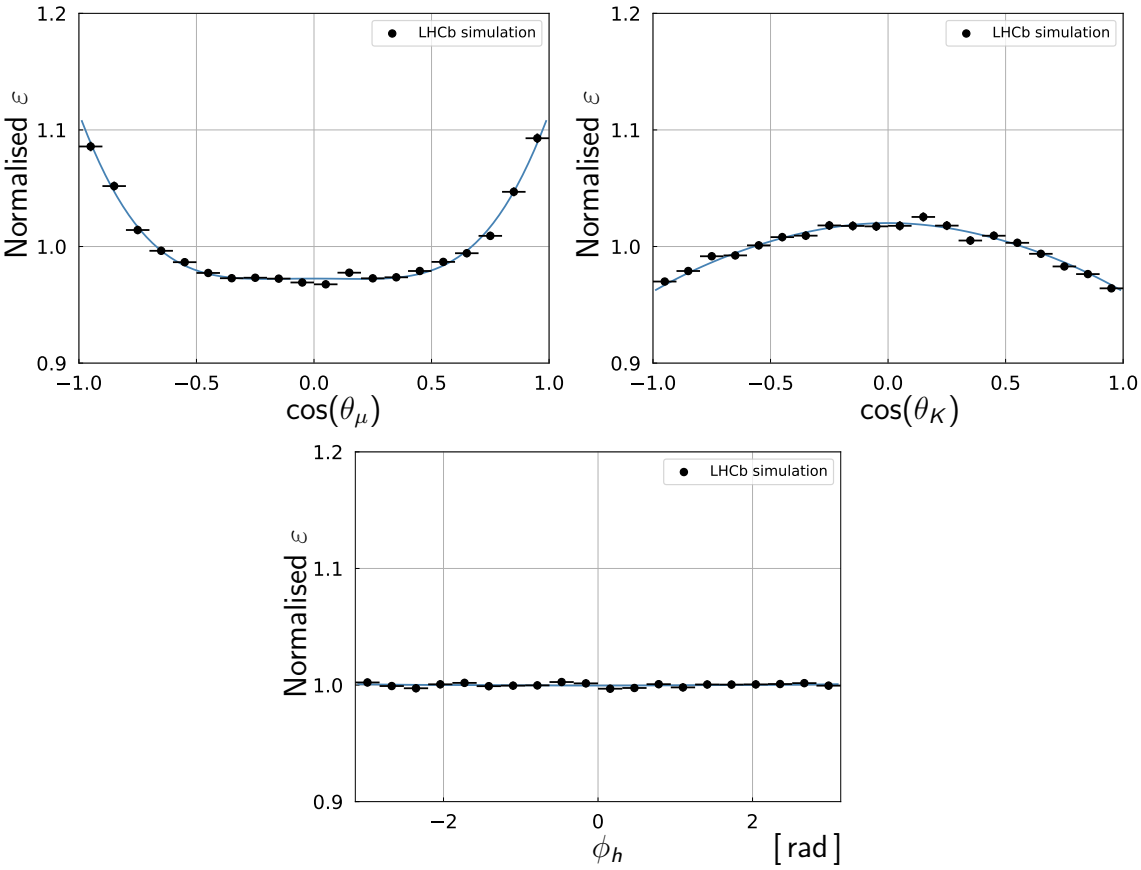

Figure 4.21: Normalised angular efficiency as a function of $\cos(\theta_K)$, $\cos(\theta_\mu)$ and ϕ_h, where in each case the efficiency is integrated over the other two angles. The points are obtained by dividing the angular distribution in the simulated sample by the distribution expected without any efficiency effect and the curves represent an even fourth-order polynomial parametrisation of each one-dimensional efficiency.

and choice of different variables used to correct the simulation to match the data with respect to the baseline strategy.

4.5 Flavour tagging

The differential decay-rate in equation 4.4 depends on the initial flavour of the B_s^0 meson, i.e. whether it was produced as B_s^0 or $\overline{B}_s^0$. The difference arises in the sign of terms proportional to $\sin(\Delta m_s t)$ or $\cos(\Delta m_s t)$ in the decay rate introduced in section 1.5.4. In case the flavour at production is not known, these contributions cancel and the measurement of the ϕ_s phase becomes almost impossible. Thus, to measure ϕ_s, the initial flavour of B_s^0 meson has to be determined. This is not trivial at pp colliders due to the large multiplicity of particles in the events. Two types of algorithms have been developed within the LHCb Collaboration to obtain the flavour tag of neutral B mesons at production. These are referred to as flavour tagging (FT) algorithms. Those

algorithms are applicable to all neutral B mesons, but in the following the focus is only on the $B_s^0 - \overline{B}_s^0$ system.

In pp collisions $b\overline{b}$ pairs are almost exclusively produced in pairs and information on the hadronised signal b-quark can be inferred from the flavour of the other b hadron in the event. The type of the algorithms relying on the flavour of the other quark in the pair are called Opposite Side (OS) flavour tagging algorithms. Information from several types of OS algorithms is combined to estimate the initial flavour of the signal B_s^0 meson. The observables related to the other b hadron decay are the charge of the muon or electron from semileptonic b decays, the charge of the kaon from the $b \to c \to s$ decay chain, the charge of a reconstructed secondary charm hadron and the charges of the tracks that form the secondary vertex of b hadron decay. These are combined into a weighted average, with weights depending on the transverse momenta of the particles. The probability of the opposite b quark to be hadronised in a flavour-specific state and inside the LHCb acceptance is not very large, thus only a small part of the candidates, approximately 10 %, in the sample has information from the OS tagger.

Another type of FT algorithm relies on the particles produced during the b-quark hadronisation and is called same-side (SS) tagging. In case of the B_s^0 meson there is usually a kaon (SSK) produced in the hadronisation. From the charge of the kaon the flavour of the signal B_s^0 can be inferred.

Together with the flavour estimate, both types of flavour-tagging algorithms provide information on how likely it is that the flavour is estimated incorrectly, the so-called mistag probability. This estimated mistag probability has to be calibrated. The calibration of OS mistag is done using the $B^+ \to J/\psi K^+$ sample, whereas the response of the SSK tagger is calibrated using the $B_s^0 \to D_s^- \pi^+$ sample. The details on the calibration procedure can be found elsewhere [81]. The calibrated and estimated mistag are assumed to be related linearly

$$\omega(\eta) = \left(p_0 + \frac{\Delta p_0}{2}\right) + \left(p_1 + \frac{\Delta p_1}{2}\right)(\eta - \langle\eta\rangle) \tag{4.28}$$

$$\overline{\omega}(\eta) = \left(p_0 - \frac{\Delta p_0}{2}\right) + \left(p_1 - \frac{\Delta p_1}{2}\right)(\eta - \langle\eta\rangle), \tag{4.29}$$

where $\omega(\eta)$ and $\overline{\omega}(\eta)$ are the calibrated mistag probabilities for B_s^0 and $\overline{B}_s^0$ mesons, respectively, and $\langle\eta\rangle$ is the average of the estimated mistag. The mistag asymmetries, $\Delta p_{0,1}$, allow for different calibrated probabilities for initial B_s^0, ω, and $\overline{B}_s^0$, $\overline{\omega}$. The resulting calibration curves are shown in figures 4.22 and 4.23 and the calibration parameters are given the table 4.3.

Due to the imperfect tagging, the total PDF for initial B_s^0 is a weighted sum of the PDF for B_s^0 and of the PDF for $\overline{B}_s^0$

$$\mathrm{PDF}^{\mathrm{meas}}(B_s^0) = (1-\omega)\mathrm{PDF}(B_s^0) + \omega\mathrm{PDF}(\overline{B}_s^0). \tag{4.30}$$

To determine what is the effect of an imperfect tagging on the ϕ_s measurement, the effect only on the terms that contain $\sin(\Delta m_s t)$ following equation 1.17, is checked

$$\begin{aligned}\mathrm{PDF}^{\mathrm{meas}}(B_s^0) &\propto (1-\omega)(1+\sin(\phi_s)\sin(\Delta m_s t)) + \omega(1-\sin(\phi_s)\sin(\Delta m_s t)) \\ &= 1 + (1-2\omega)\sin(\phi_s)\sin(\Delta m_s t),\end{aligned} \tag{4.31}$$

Table 4.3: Calibration parameters for the OS and SSK taggers. Where given, the first uncertainty is statistical and the second is systematic.

Tagger	OS	SSK
p_0	$0.389 \pm 0.001 \pm 0.003$	$0.433 \pm 0.011 \pm 0.003$
p_1	$0.849 \pm 0.006 \pm 0.027$	$0.92 \pm 0.13 \pm 0.02$
Δp_0	0.009 ± 0.001	0.00 ± 0.03
Δp_1	0.014 ± 0.012	0.00 ± 0.03
$\langle \eta \rangle$	0.360	0.417

so the sensitivity to ϕ_s is diluted by a dilution factor $\mathcal{D} \equiv (1 - 2\omega)$ in terms of $\sqrt{N}$, where N is the total number of events. Given that only the fraction, ε_{tag}, of all the candidates is tagged, the total dilution, the so-called tagging power, is defined as $\varepsilon_{tag}\mathcal{D}^2$. The tagging power characterizes the effective reduction in statistical power of the signal sample due to tagging. Table 4.4 summarises the tagging power obtained with both tagging algorithms.

Approximately 31% of the tagged candidates in the $B_s^0 \to J/\psi K^+K^-$ sample are tagged by both the OS and the SSK algorithms. Since the algorithms are uncorrelated, as they select mutually exclusive charged particles, the two tagging results are combined taking into account both decisions and their corresponding estimate of η. The calibration parameters are used in the time-dependent angular fit with a Gaussian constraint applied. Therefore the uncertainties on the parameters are propagated to the statistical uncertainty of the measured observables. The uncertainties in the calibration parameters are translated to an uncertainty of approximately 15 mrad on the ϕ_s measurement.

Table 4.4: Overall tagging performance for $B_s^0 \to J/\psi K^+K^-$. The uncertainty on $\varepsilon_{tag}\mathcal{D}^2$ is obtained by varying the tagging calibration parameters within their statistical and systematic uncertainties summed in quadrature.

Category	$\varepsilon_{tag}(\%)$	$\mathcal{D}^2$	$\varepsilon_{tag}\mathcal{D}^2(\%)$
OS only	11.4	0.078	0.88 ± 0.04
SSK only	42.6	0.032	1.38 ± 0.30
OS & SSK	23.8	0.104	2.47 ± 0.15
Total	77.8	0.061	4.73 ± 0.34

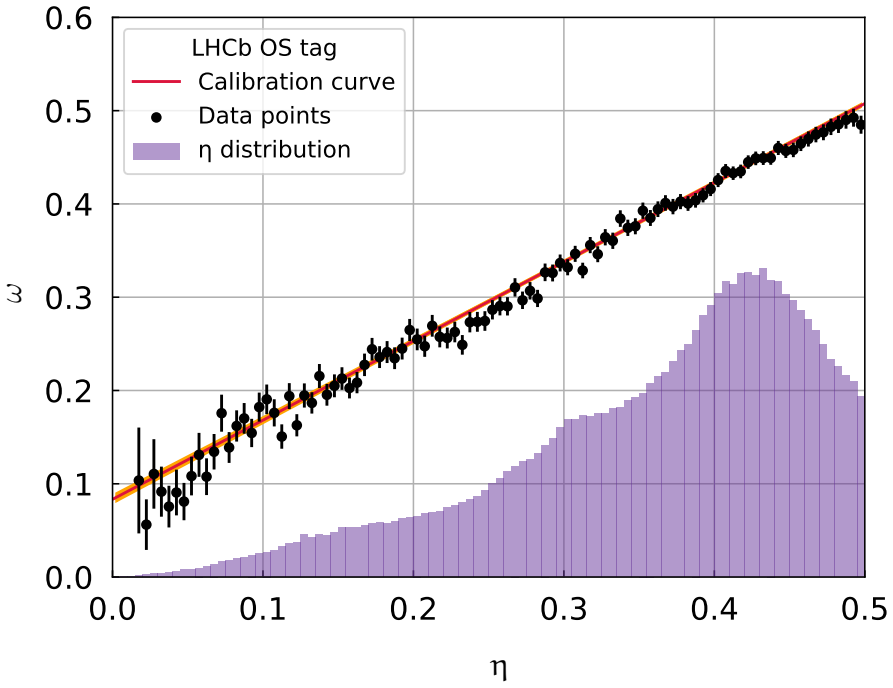

Figure 4.22: Calibration of the OS tagger using $B^+ \to J/\psi K^+$ decays. The black points show the average measured mistag probability, ω, in bins of predicted mistag, η, the red line shows the calibration and the orange area is the calibration uncertainty within one standard deviation. The shaded histogram shows the distribution, with arbitrary normalisation, of η in the background-subtracted $B_s^0 \to J/\psi K^+K^-$ sample, summing over candidates tagged as B_s^0 or $\overline{B}_s^0$.

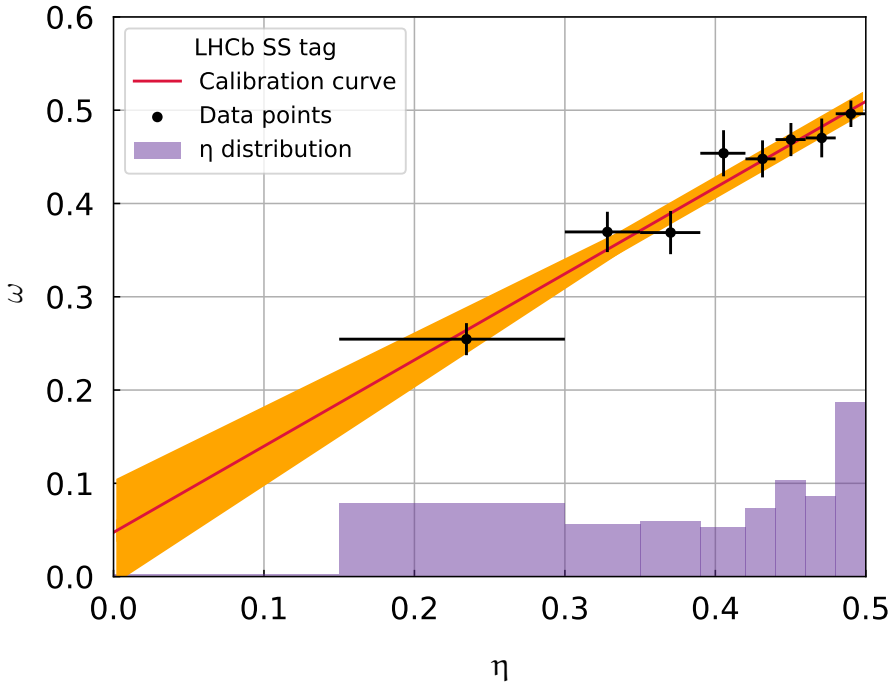

Figure 4.23: Calibration of the SSK tagger using $B_s^0 \to D_s^- \pi^+$ decays. The black points show the average measured mistag probability, ω, in bins of predicted mistag, η, the red line shows the calibration obtained from the fit, and the orange area is the calibration uncertainty within one standard deviation. The shaded histogram shows the distribution of η in the background-subtracted $B_s^0 \to J/\psi K^+ K^-$ sample.

Chapter 5

Systematic uncertainties

The analysis methods and approaches used in the analysis rely on some assumptions and on external samples with limited statistics. This can potentially introduce biases in the measurements and therefore has to be carefully studied. Any potential effect should be covered by an assigned systematic uncertainty. The sources of systematic uncertainties and their relative contributions are summarised in the tables 5.8 and 5.9 and explained below.

Mass fit: shape The per-event mass uncertainties are underestimated and this effect is corrected for. A quadratic calibration with two scale factors is chosen as the baseline, following the trend seen in the simulated sample. To test this, a linear parametrisation is used as alternative. It is checked that the tail parameters of the signal $m(J/\psi K^+K^-)$ distribution are almost uncorrelated with the scale factors (s_1 and s_2), therefore the mass fit with quadratic parametrisation is used. The full analysis procedure is then repeated, with a fit where a linear per-event uncertainty calibration is used, i.e. assuming $\sigma_{CB} = s_1 \times \sigma_i$. Table 5.1 summarises the difference in the fit parameters between this alternative and the baseline. The obtained difference is not significant and therefore no corresponding systematic uncertainty is assigned.

Mass fit: sample size The parameters of the $m(J/\psi K^+K^-)$ fit model are used to determine the *sWeights*, as explained in section 4.2. The parameters of the mass model are obtained from the fit with statistical uncertainties. To propagate these uncertainties, the parameters of the $m(J/\psi K^+K^-)$ fit model are varied within these uncertainties and new sets of event weights are calculated. Parameters that are allowed to vary in the fit are the mean of the distribution, two scale factors, the fraction of the B^0 contribution and the slope of the exponential background. Each parameter is shifted simultaneously by $+1\sigma$ or -1σ. The correlation between all parameters of the mass model, except for s_1 and s_2, is neglected. However these two scale factors are negatively correlated, because both would affect RMS in the same way. To take this into account the parameters are varied in opposite directions. For each of the two options, the new set of signal weights is calculated. Afterwards, the full decay time and angular fit

Table 5.1: Deviations in parameter estimates from the nominal result when using the mass model with linear parametrisation instead of quadratic. Differences with the baseline results are given in the second column in fractions of the statistical uncertainties (rel) and in the third column the absolute difference is given (abs).

	rel	abs
ϕ_s	-0.006	-0.0003
$\lvert\lambda\rvert$	-0.017	-0.0003
$\Gamma_s - \Gamma_d$	0.006	–
$\Delta\Gamma$	-0.033	-0.0002
Δm_s	-0.021	-0.0012
$\lvert A_\perp\rvert^2$	0.111	0.0004
$\lvert A_0\rvert^2$	-0.203	-0.0006
$\delta_\perp - \delta_0$	-0.004	-0.0005
$\delta_\parallel - \delta_0$	-0.042	-0.0033
F_{S1}	-0.113	-0.0049
F_{S2}	-0.082	-0.0006
F_{S3}	-0.064	-0.0001
F_{S4}	-0.152	-0.0008
F_{S5}	-0.232	-0.0031
F_{S6}	-0.274	-0.0050
$\delta_{S1} - \delta_\perp$	0.030	0.0054
$\delta_{S2} - \delta_\perp$	-0.005	-0.0014
$\delta_{S3} - \delta_\perp$	0.033	0.0141
$\delta_{S4} - \delta_\perp$	-0.076	-0.0140
$\delta_{S5} - \delta_\perp$	-0.101	-0.0097
$\delta_{S6} - \delta_\perp$	-0.081	-0.0117

is repeated using the new weights. The differences in parameter values with respect to the ones from the nominal fit are negligible in comparison to the statistical uncertainty and to other sources of systematic uncertainties, therefore no systematic uncertainty is assigned. Table 5.2 summarises the differences found when varying the parameters according to $\pm 1\sigma$.

Mass fit: factorisation In the previous version of this analysis [81], a large systematic uncertainty was assigned due to the fact that the correlation of the mass shape and one of the helicity angles, $\cos(\theta_\mu)$, was not properly taken into account. The mass model is now improved to use the per-candidate mass uncertainty in order to account for the observed correlation between the $m(J/\psi K^+K^-)$ shape and $\cos(\theta_\mu)$ observable. To check if the updated mass model properly accounts for the existing correlation, the data sample is split in the three following bins, $0 < |\cos(\theta_\mu)| < 0.25$, $0.25 < |\cos(\theta_\mu)| < 0.7$ and $0.7 < |\cos(\theta_\mu)| < 1$. In

Table 5.2: Deviations in parameter estimates from the nominal result when varying the mass model parameters according to $\pm 1\sigma$. Differences with the baseline results are given in fractions of the statistical uncertainties. In the last column (abs) the absolute difference is given.

	$+1\sigma$	-1σ	rel	abs
ϕ_s	0.014	−0.009	0.014	0.0006
$\lvert\lambda\rvert$	0.018	−0.008	0.018	0.0003
$\Gamma_s - \Gamma_d$	0.191	−0.184	0.191	0.0004
$\Delta\Gamma_s$	−0.025	0.024	0.025	0.0002
Δm_s	−0.032	0.030	0.032	0.0019
$\lvert A_\perp\rvert^2$	−0.012	−0.002	0.012	0.0
$\lvert A_0\rvert^2$	0.001	0.003	–	–
$\delta_\perp - \delta_0$	−0.020	0.021	0.021	0.0027
$\delta_\parallel - \delta_0$	−0.004	0.015	0.015	0.0012
F_{S1}	0.030	−0.044	0.044	0.0019
F_{S2}	0.036	−0.034	0.036	0.0003
F_{S3}	0.024	−0.022	0.024	0.0001
F_{S4}	0.042	−0.036	0.042	0.0002
F_{S5}	0.085	−0.071	0.085	0.0011
F_{S6}	0.093	−0.033	0.093	0.0017
$\delta_{S1} - \delta_\perp$	0.026	−0.009	0.026	0.0048
$\delta_{S2} - \delta_\perp$	−0.046	0.014	0.046	0.0138
$\delta_{S3} - \delta_\perp$	−0.016	0.014	0.016	0.0068
$\delta_{S4} - \delta_\perp$	0.021	−0.021	0.021	0.0039
$\delta_{S5} - \delta_\perp$	0.034	−0.031	0.034	0.0033
$\delta_{S6} - \delta_\perp$	0.038	−0.026	0.038	0.0055

each bin mass fit to the m($J/\psi K^+K^-$) is performed and the fit parameters are extracted, namely mean, slope of the background exponential, the per-event mass uncertainty scale factors (s_1, s_2) and fraction of B^0 contribution. For each set of these obtained parameters the mass fit to the full data sample is performed fixing the mean, slope of the background exponential, and per-event mass uncertainty scale factors to the values obtained from the fit to the corresponding bin in $\cos(\theta_\mu)$. The number of signal and background events are left free, and the *sWeights* are re-calculated. For each set of alternative *sWeights*, the full time-dependent fit is performed. The deviations from the baseline result are summarised in table 5.3 and are found negligible in comparison to the statistical uncertainty and to other sources of systematic uncertainties. Therefore, it is concluded that the mass model that makes use of the per-event mass uncertainty properly accounts for the correlation between the m($J/\psi K^+K^-$) shape and $\cos(\theta_\mu)$ observable, eliminating

Table 5.3: Deviations in parameter estimates from the nominal polarisation independent results when using the mass model from each of the 3 $\cos(\theta_\mu)$ bins as nominal. Differences with the baseline results are given in fractions of the statistical uncertainties. In the last column (abs) the absolute difference is given.

	0-0.25	0.7-1	0.25-0.7	max	abs
ϕ_s	0.001	−0.019	−0.025	0.03	0.0010
$\lvert\lambda\rvert$	−0.032	−0.009	−0.009	0.03	0.0005
$\Gamma_s - \Gamma_d$	0.155	−0.057	0.034	0.15	0.0004
$\Delta\Gamma_s$	−0.039	0.025	−0.002	0.04	0.0003
Δm_s	0.053	0.008	0.005	0.05	0.0031
$\lvert A_\perp\rvert^2$	0.044	−0.060	0.051	0.06	0.0002
$\lvert A_0\rvert^2$	−0.042	0.082	−0.094	0.09	0.0003
$\delta_\perp - \delta_0$	0.022	−0.053	0.012	0.05	0.0068
$\delta_\parallel - \delta_0$	−0.010	−0.014	–	–	–
F_{S1}	0.416	0.097	0.039	0.42	0.0178
F_{S2}	0.084	0.025	−0.048	0.08	0.0007
F_{S3}	−0.022	0.034	−0.052	0.05	0.0001
F_{S4}	0.001	−0.023	−0.046	0.05	0.0002
F_{S5}	0.168	−0.043	−0.106	0.17	0.0022
F_{S6}	−0.122	0.288	0.217	0.29	0.0053
$\delta_{S1} - \delta_\perp$	−0.173	−0.146	0.016	0.17	0.0318
$\delta_{S2} - \delta_\perp$	0.026	0.028	0.001	0.03	0.0084
$\delta_{S3} - \delta_\perp$	0.016	−0.018	0.030	0.03	0.0128
$\delta_{S4} - \delta_\perp$	0.004	−0.021	−0.030	0.03	0.0055
$\delta_{S5} - \delta_\perp$	0.091	−0.014	−0.040	0.09	0.0087
$\delta_{S6} - \delta_\perp$	−0.040	0.165	0.088	0.17	0.0238

the corresponding systematic uncertainty.

The same procedure is repeated for the other two helicity angles, $\cos(\theta_K)$ and ϕ_h. The corresponding results are summarised in tables 5.4 and 5.5. The deviations from the baseline results for the angles are found negligible in comparison to the statistical uncertainty and to other sources of systematic uncertainties and as a result no systematic uncertainty is assigned.

The only observable that has a visible correlation with the $m(J/\psi K^+K^-)$ shape is the decay time. The slope of the combinatorial background varies as a function of the decay time of the B_s^0 meson. This effect is visible when the full sample is fitted with the slope of the exponential fixed to the value found when fitting one of the three time intervals: $t < 0.6$ ps, $0.6 < t < 1.3$ ps and $1.3 < t$ ps. The corresponding mass fit projections, for three intervals in decay time, are shown in figure 5.1. The variation of the slope of the combinatorial

Table 5.4: Deviations in parameter estimates from the nominal polarisation-independent results when using the mass model from each of the 3 $\cos(\theta_K)$ bins as nominal. Differences with the baseline results are given in fractions of the statistical uncertainties. In the last column (abs) the absolute difference is given.

	0-0.25	0.7-1	0.25-0.7	max	abs
ϕ_s	-0.002	-0.005	-0.019	0.02	0.0008
$\lvert\lambda\rvert$	-0.019	0.026	-0.009	0.03	0.0004
$\Gamma_s - \Gamma_d$	-0.134	0.011	0.029	0.13	0.0003
$\Delta\Gamma_s$	0.062	-0.001	0.002	0.06	0.0005
Δm_s	0.017	0.049	0.008	0.05	0.0028
$\lvert A_\perp\rvert^2$	-0.036	-0.050	0.005	0.05	0.0002
$\lvert A_0\rvert^2$	0.016	0.079	0.012	0.08	0.0002
$\delta_\perp - \delta_0$	$-$	0.033	-0.006	0.03	0.0043
$\delta_\parallel - \delta_0$	-0.006	0.017	0.005	0.02	0.0013
F_{S1}	-0.017	0.606	0.053	0.61	0.0260
F_{S2}	-0.043	0.227	-0.025	0.23	0.0018
F_{S3}	-0.036	0.023	0.010	0.04	0.0001
F_{S4}	0.024	0.029	-0.012	0.03	0.0002
F_{S5}	-0.116	0.165	0.002	0.17	0.0022
F_{S6}	-0.214	0.086	0.242	0.24	0.0044
$\delta_{S1} - \delta_\perp$	-0.065	-0.077	-0.033	0.08	0.0141
$\delta_{S2} - \delta_\perp$	0.007	0.018	0.015	0.02	0.0054
$\delta_{S3} - \delta_\perp$	0.019	-0.012	-0.006	0.02	0.0081
$\delta_{S4} - \delta_\perp$	0.003	0.004	-0.007	$-$	$-$
$\delta_{S5} - \delta_\perp$	-0.060	0.103	0.005	0.1	0.0099
$\delta_{S6} - \delta_\perp$	-0.032	-0.001	0.094	0.1	0.0135

background as a function of time is not taken into account in the baseline mass fit model. The corresponding systematic effect is evaluated by dividing the data sample in several decay-time bins prior to evaluating the *sWeights*. Several binning schemes are chosen, i.e. $[0.3, 0.4, 0.7, 15]$, $[0.3, 0.37, 0.5, 0.8, 15]$ and $[0.3, 0.35, 0.43, 0.56, 0.9, 15]$. A larger number of bins is not possible due to the limited size of the sample. The binning, used to calculate the alternative signal weights is only performed on 2016 data since 2015 data has an insufficient sample size to be divided. Table 5.6 summarises the maximum deviations for each of the fit parameters between the three alternative binning schemes. Those numbers are then assigned as systematic uncertainties due to the factorisation of the mass and the decay-time observable.

Mass fit: per-event uncertainty as a function of mass Since the distributions of the per-event mass uncertainty changes in the sideband region as a function

Table 5.5: Deviations in parameter estimates from the nominal polarisation independent results when using the mass model from each of the 3 ϕ_h angle bins as nominal. Differences with the baseline results are given in fractions of the statistical uncertainties. In the last column (abs) the absolute difference is given.

	[-π;-1]	[-1;1]	[1;π]	max	abs
ϕ_s	−0.019	0.001	0.010	0.02	0.0008
$\lvert\lambda\rvert$	−0.012	–	−0.001	–	–
$\Gamma_s - \Gamma_d$	0.089	−0.002	−0.1	0.10	0.0002
$\Delta\Gamma_s$	−0.021	0.018	0.042	0.04	0.0003
Δm_s	–	0.037	0.025	0.04	0.0021
$\lvert A_\perp\rvert^2$	−0.002	−0.011	−0.021	0.02	0.0001
$\lvert A_0\rvert^2$	0.016	0.016	0.027	0.03	0.0001
$\delta_\perp - \delta_0$	−0.015	0.034	0.006	0.03	0.0044
$\delta_\parallel - \delta_0$	–	0.016	0.010	0.02	0.0013
F_{S1}	0.259	0.055	0.097	0.26	0.0111
F_{S2}	0.063	0.050	−0.020	0.06	0.0005
F_{S3}	0.007	0.011	−0.005	–	–
F_{S4}	0.060	−0.031	−0.013	0.06	0.0003
F_{S5}	0.065	0.047	−0.008	0.07	0.0009
F_{S6}	0.039	0.024	−0.083	0.08	0.0015
$\delta_{S1} - \delta_\perp$	−0.096	−0.012	−0.009	0.10	0.0176
$\delta_{S2} - \delta_\perp$	0.012	0.007	0.016	0.02	0.0048
$\delta_{S3} - \delta_\perp$	−0.003	−0.007	0.002	–	–
$\delta_{S4} - \delta_\perp$	0.023	−0.021	−0.012	0.02	0.0042
$\delta_{S5} - \delta_\perp$	0.030	0.028	0.004	0.03	0.0029
$\delta_{S6} - \delta_\perp$	0.004	0.017	−0.033	0.03	0.0048

of the invariant mass, a corresponding systematic uncertainty is determined. The possible contribution from this so-called Punzi effect [93] is studied by generating background in the $B_s^0 \to J/\psi K^+K^-$ simulated sample. The details on the generating procedure can be found in reference [94]. Two different options are used for the background generation, including and excluding a dependence of the distribution of the per-event mass uncertainty on the mass. The analysis is repeated with the two different setups and no difference in the final results is observed. Therefore, no systematic uncertainty due to this effect is assigned.

Mass fit: peaking backgrounds As described in section 4.1, using a combination of data sidebands and simulation, two resonant backgrounds, $B^0 \to J/\psi K^{*0}$ and $\Lambda_b^0 \to J/\psi p K^-$, are identified and quantified, where the $K^+\pi^-$ and pK^- pairs are mis-identified as K^+K^- candidates. The contribution from $B^0 \to J/\psi K^{*0}$ decays is found to be relatively small and after the veto explained in section 4.1.1, this

contribution is negligible. If any event survives the veto, its effect is accounted for by the combinatorial background description. The systematic uncertainty due to the knowledge on the normalisation of the $\Lambda_b^0 \to J/\psi p K^-$ contribution is estimated by repeating the fit, varying the amount of this background by one standard deviation of its measured yield. The deviation from the baseline results is found to be negligible as shown in table 5.7 and therefore no systematic uncertainty is assigned.

Concerning the $B^0 \to J/\psi K^+ K^-$ background, a different model is used to fit this contribution leaving the resolution free in the fit. The corresponding systematic uncertainty is evaluated as the difference with respect to the nominal result and is found to be negligible.

Multiple candidates Some events contain multiple reconstructed candidates after the full selection has been applied as explained in section 4.1.2. One of the type of multiple candidates arising both in the signal $B_s^0 \to J/\psi K^+ K^-$ and the control

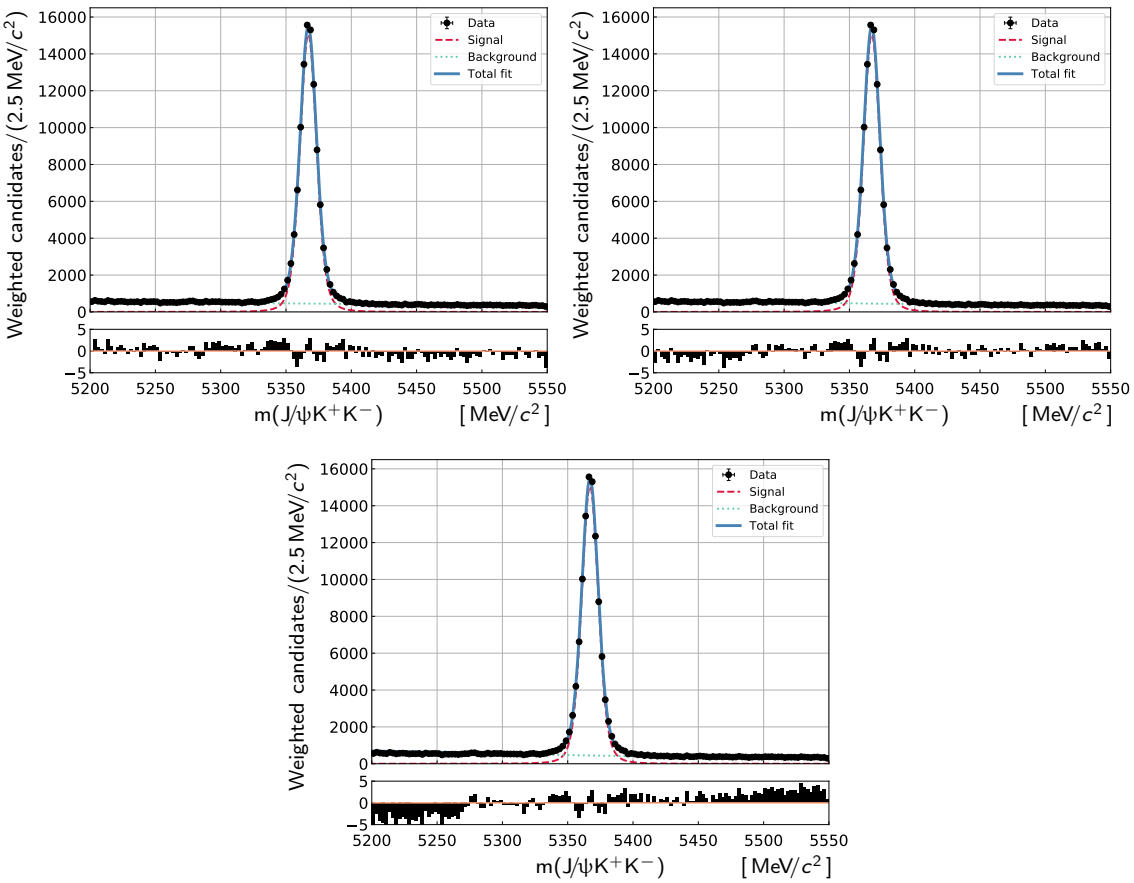

Figure 5.1: Fit (solid blue line) to the $m(J/\psi K^+ K^-)$ distribution for data using the mass shape from the decay time bins as nominal. Top left plot: $t < 0.6$ ps, top right: $0.6 < t < 1.3$ ps and bottom: $1.3 < t$ ps.

Table 5.6: Maximum deviations in parameter estimates from the baseline result when using the decay-time binning schemes. Differences with the baseline results are given in fractions of the statistical uncertainties (rel). In the last column (abs) the absolute difference is given.

	rel	abs
ϕ_s	-0.097	-0.004
$\lvert\lambda\rvert$	0.24	0.0037
$\Gamma_s - \Gamma_d$	0.317	0.0007
$\Delta\Gamma_s$	-0.287	-0.0022
Δm_s	0.267	0.0156
$\lvert A_\perp\rvert^2$	0.118	0.0005
$\lvert A_0\rvert^2$	0.078	0.0002
$\delta_\perp - \delta_0$	0.36	0.0465
$\delta_\parallel - \delta_0$	0.119	0.0093
F_{S1}	-0.132	-0.0056
F_{S2}	0.074	0.0006
F_{S3}	0.021	$-$
F_{S4}	0.076	0.0004
F_{S5}	0.137	0.0018
F_{S6}	0.137	0.0025
$\delta_{S1} - \delta_\perp$	-0.438	-0.0803
$\delta_{S2} - \delta_\perp$	-0.083	-0.0252
$\delta_{S3} - \delta_\perp$	-0.044	-0.0186
$\delta_{S4} - \delta_\perp$	-0.05	-0.0091
$\delta_{S5} - \delta_\perp$	-0.079	-0.0075
$\delta_{S6} - \delta_\perp$	-0.231	-0.0333

$B^0 \to J/\psi K^{*0}$ channels appear to be clones, i.e. the tracks of their daughter particles are separated by angles smaller than 5 mrad. To check the effect of these candidates, the analysis procedure is repeated on the sample where only one, randomly selected, candidate is used for any given event. The multiple candidates are removed both for the control and the signal modes. The removed fractions are around 0.35 % and 0.2 % with respect to the selected B_s^0 and B^0 candidates, respectively. The maximum difference in the parameters with respect to the nominal result is assigned as systematic uncertainty.

Fit bias The fitting procedure itself can potentially introduce bias in the measurements. In order to check whether this is the case, eight thousand pseudoexperiments are generated. Each sample has a size equivalent to the size of the data sample. The fit is performed for each of the generated samples and the resulting pull distributions are studied. Those resulting biases that are significantly different from zero are assigned as systematic uncertainties.

Table 5.7: Deviations in parameter estimates from the nominal result when subtracting plus or minus one σ of the nominal Λ_b^0 yield. Differences with the baseline results are given in fractions of the statistical uncertainties. Third column (max) is a maximum of first two and is used to assign the final systematics. In the last column (abs) the absolute difference is given.

	yield+	yield-	max	abs
ϕ_s	−0.006	0.013	0.013	0.0005
$\lvert\lambda\rvert$	0.004	0.009	–	–
$\Gamma_s - \Gamma_d$	−0.003	0.003	–	–
$\Delta\Gamma_s$	−0.001	0.002	–	–
Δm_s	−0.001	−0.01	–	–
$\lvert A_\perp\rvert^2$	0.004	−0.008	–	–
$\lvert A_0\rvert^2$	−0.007	0.01	–	–
$\delta_\perp - \delta_0$	−0.014	−0.043	0.043	0.0056
$\delta_\parallel - \delta_0$	0.001	0.007	–	–
F_{S1}	−0.024	0.058	0.058	0.0025
F_{S2}	−0.001	0.003	–	–
F_{S3}	0.004	−0.001	–	–
F_{S4}	−0.007	0.001	–	–
F_{S5}	−0.002	0.013	0.013	0.0002
F_{S6}	−0.004	0.017	0.017	0.0003
$\delta_{S1} - \delta_\perp$	0.005	−0.009	–	–
$\delta_{S2} - \delta_\perp$	−0.007	−0.016	0.016	0.0048
$\delta_{S3} - \delta_\perp$	−0.008	0.001	–	–
$\delta_{S4} - \delta_\perp$	–	0.002	–	–
$\delta_{S5} - \delta_\perp$	−0.001	0.004	–	–
$\delta_{S6} - \delta_\perp$	0.002	−0.004	–	–

C_{SP} factors The computation of the coupling C_{SP} factors, explained in detail in reference [72], relies on the parametrisation of the S-wave shape. To evaluate the systematic uncertainty, different models from [95] are used to evaluate the values of C_{SP} in each m_{KK} bin. The maximum difference in the fit parameters obtained with these alternative S-wave models is assigned as systematic uncertainty.

Time resolution The calibration of the decay time resolution model is determined on the prompt sample and then applied to the signal sample. The systematic uncertainty related to the assumption that the calibration parameters obtained for the prompt sample are valid for the signal sample is evaluated using simulated samples. For the simulated samples, the decay time resolution can be determined since both generated and reconstructed decay times are known. The calibration curves for the decay-time resolution are determined both on the signal and control

simulated samples. The resolution in the signal prompt sample is scaled with ratio of the calibration curves in the signal and control simulated samples. The difference between the results obtained using the baseline control sample and that where the resolution is scaled with the ratios of calibration curves is assigned as systematic uncertainty.

A third source is a possible bias of the mean of the Gaussian resolution model, which is assumed to be zero in the baseline model. As an alternative, the mean of the Gaussian function is parametrised to depend quadratically on the per-event decay time uncertainty. The analysis procedure is repeated with this alternative calibration and the difference in the parameters with respect to the nominal result is assigned as systematic uncertainty.

Another source of systematic uncertainty arises from varying the contribution of the candidates with an associated wrong origin vertex in the determination of the resolution model. The fraction of this contribution is varied between 0 and 1.5 %, around three times the fraction that is measured in the prompt sample. The fit is repeated with the updated calibration and the maximum difference between the results obtained using the baseline and the alternative fraction of wrong-PV contribution is assigned as systematic uncertainty.

Angular efficiency The systematic uncertainty due to the limited size of the simulated sample used to determine the angular acceptance weights is estimated by varying the acceptance weights within their uncertainty and repeating the full analysis procedure with the new weights for the time acceptance. The resulting RMS for each physics parameter is assigned as a systematic uncertainty.

Prior to the evaluation of the acceptance weights, the simulated sample is weighted to match data as closely as possible. The gradient-boost tree method is used to perform a multidimensional weighting [91]. The effect of this weighting is studied by repeating the full analysis procedure with one hundred different configurations of the reweighter. The maximum difference relative to the nominal result is assigned as a systematic uncertainty.

As alternative to the nominal procedure of separating the uniform component in the ghost background category of the simulated sample, this category is removed by matching reconstructed and generated particles in the simulated sample by comparing the magnitudes and direction of their momenta. A new set of angular weights is determined with this alternative way of treating the ghost background category and the fit procedure is repeated. The maximum difference with respect to the nominal result is assigned as systematic uncertainty.

The analysis assumes that the parts of the selection and reconstruction efficiency dependent on the decay time and decay angles are uncorrelated. The possible bias is estimated by splitting the simulated sample in data-sized samples and performing the fit on them. The parameter estimations are compared with the generated values, and the difference is assigned as systematic uncertainty.

Decay time efficiency A systematic uncertainty arises due to the statistical uncertainty of the coefficients of the spline functions that are used to describe the time acceptance. These coefficients are varied within their uncertainty and the resulting RMS of the parameters are taken as their systematic uncertainties.

In addition, both the simulated signal and simulated control samples are weighted to match the data sample. The weighting is performed in a two-step procedure, matching the kinematic distributions and matching the fraction of S-wave for the simulated samples. To estimate the systematic uncertainty due to this weighting procedure, the analysis is repeated without applying one of the weighting steps. The difference with the nominal result is then assigned as systematic uncertainty.

Another source of systematic uncertainty is the differences observed in decay-time acceptance obtained using the simulated samples with $\Delta\Gamma_s$ equal to or different from zero. The difference between the results obtained using these two simulated samples is assigned as systematic uncertainty.

Length scale The uncertainty on the LHCb length scale is estimated to be 0.022% [96], as determined from metrology and track-based alignment. This translates directly into an uncertainty on $\Gamma_s - \Gamma_d$, $\Delta\Gamma_s$ and Δm_s, which is non-negligible only in the case of Δm_s. Other parameters are unaffected. The precision on the track momentum scale is 0.03%. Its effect largely cancels in the computation of the decay time, leading to negligible uncertainties on all observables.

Table 5.8: Summary of the systematic uncertainties.

Source	ϕ_s [rad]	$\lvert\lambda\rvert$	$\Gamma_s - \Gamma_d$ [ps^{-1}]	$\Delta\Gamma_s$ [ps^{-1}]	Δm_s [ps^{-1}]	$\lvert A_\perp\rvert^2$	$\lvert A_0\rvert^2$	$\delta_\perp - \delta_0$ [rad]	$\delta_\parallel - \delta_0$ [rad]
Mass fit: shape	0.0003	0.0003	-	0.0002	0.001	0.0004	0.0006	-	0.003
Mass fit: factorisation	0.004	0.0037	0.0007	0.0022	0.016	0.0005	0.0002	0.05	0.009
Multiple candidates	0.0011	0.0011	0.0003	0.0001	0.001	0.0001	0.0001	0.01	0.002
Fit bias	0.0010	-	-	0.0003	0.001	0.0006	0.0001	0.02	0.033
C_{SP} factors	0.0010	0.0010	-	0.0001	0.002	0.0001	-	0.01	0.005
Time resolution: model applicability	-	-	-	-	0.001	-	-	-	0.001
Time resolution: t bias	0.0032	0.0010	0.0002	0.0003	0.005	-	-	0.08	0.001
Time resolution: wrong PV	-	-	-	-	0.001	-	-	-	0.001
Angular efficiency: simulated sample size	0.0011	0.0018	-	-	0.001	0.0004	0.0003	-	0.004
Angular efficiency: weighting	0.0022	0.0043	0.0001	0.0002	0.001	0.0011	0.0020	0.01	0.008
Angular efficiency: clone candidates	0.0005	0.0014	0.0002	0.0001	-	0.0001	0.0002	-	0.002
Angular efficiency: t & σ_t dependence	0.0012	0.0007	0.0002	0.0010	0.003	0.0012	0.0008	0.03	0.006
Decay-time efficiency: statistical	-	-	0.0012	0.0008	-	0.0003	0.0002	-	-
Decay-time efficiency: kinematic weighting	-	-	0.0002	-	-	-	-	-	-
Decay-time efficiency: PDF weighting	-	-	0.0001	0.0001	-	-	-	-	-
Decay-time efficiency: $\Delta\Gamma_s = 0$ simulation	-	-	0.0003	0.0005	-	0.0002	0.0001	-	-
Length scale	-	-	-	-	0.004	-	-	-	-
Quadratic sum of systematic contributions	0.0061	0.0064	0.0015	0.0026	0.018	0.0019	0.0023	0.10	0.036

Table 5.9: Summary of the systematic uncertainties for the S-wave contribution. Sources of the systematic uncertainties is in the same order as in table 5.8.

F_{S1}	F_{S2}	F_{S3}	F_{S4}	F_{S5}	F_{S6}	$\delta_S^1 - \delta_\perp$ [rad]	$\delta_S^2 - \delta_\perp$ [rad]	$\delta_S^3 - \delta_\perp$ [rad]	$\delta_S^4 - \delta_\perp$ [rad]	$\delta_S^5 - \delta_\perp$ [rad]	$\delta_S^6 - \delta_\perp$ [rad]
0.0049	0.0006	0.0001	0.0008	0.0031	0.0050	0.005	0.001	0.014	0.014	0.010	0.012
0.0056	0.0006	-	0.0004	0.0018	0.0025	0.080	0.025	0.019	0.009	0.008	0.033
0.0017	0.0012	0.0002	0.0007	0.0014	0.0006	0.011	-	0.024	0.007	0.004	0.007
0.0008	0.0042	0.0013	0.0007	0.0002	0.0007	0.050	0.020	0.080	0.110	0.010	0.040
0.0010	0.0031	0.0004	0.0004	0.0010	0.0070	0.180	0.020	0.030	0.010	0.010	0.100
0.0001	0.0001	-	0.0001	0.0003	-	-	-	-	0.002	0.001	0.001
0.0001	-	-	0.0001	0.0001	-	-	0.003	0.002	0.003	0.006	0.002
0.0001	0.0001	-	0.0001	0.0002	-	-	0.001	0.001	0.001	0.001	0.001
0.0007	0.0003	0.0001	0.0003	0.0006	0.0006	0.003	0.006	0.013	0.012	0.004	0.004
0.0023	0.0003	0.0001	0.0006	0.0012	0.0014	0.005	0.016	0.031	0.011	0.005	0.004
-	0.0002	0.0001	0.0002	0.0006	0.0005	-	-	-	0.004	0.002	0.002
0.0063	0.0007	0.0002	0.0002	0.0010	0.0016	0.013	0.022	0.027	0.032	0.010	0.010
-	-	-	-	-	-	-	-	-	-	-	-
-	-	-	-	-	-	-	-	-	-	-	-
-	-	-	-	-	-	-	-	-	-	-	-
-	-	-	-	-	-	-	-	-	-	-	-
-	-	-	-	-	-	-	-	-	-	-	-
0.010	0.0055	0.0014	0.0016	0.0044	0.009	0.20	0.047	0.101	0.117	0.023	0.114

Chapter 6

Results

After the selection of the signal candidates, as described in section 4.1, each candidate i is given a signal weight w_i using the *sPlot* method with m ($J/\psi K^+K^-$) as a discriminating variable and σ_m as a conditional variable as explained in section 4.2. The resulting, background subtracted sample contains approximately 117k candidates. A weighted fit is then performed to the B_s^0 decay time and helicity-angle distributions using a PDF from equation 4.4. The log-likelihood in each of the 24 data subsamples is scaled by a per-sample factor

$$\alpha = \frac{\sum_i w_i}{\sum_i w_i^2} \tag{6.1}$$

to account for the effect of the weights in the determination of the parameter uncertainties [97].

The non-uniform efficiency as a function of decay time is accounted for in the PDF with the cubic spline. The parameters of the cubic splines, representing the time acceptance separately for unbiased and biased subsamples are obtained as described in section 4.3.1 and are fixed in the fit. In the decay time resolution part of the PDF, the calibrated decay-time error is used as a per-event conditional observable, with the calibration parameters obtained as explained in section 4.3.3. The non-uniform efficiency as a function of helicity angles is accounted for in the PDF using the normalisation weights, the evaluation of which is described in section 4.4.1. The response of the flavour-tagging algorithms is calibrated with the procedure outlined in section 4.5. In the fit, the calibration parameters for mistag probabilities are Gaussian-constrained, which allows them to vary within their estimated uncertainties.

6.1 Baseline result

The time-dependent angular fit is performed independently by five fit implementations for cross-validation purposes. The fit result from one of these fitters (the one based on GPU technology and which evaluates faster than the others) is quoted as a baseline

result in reference [72] to be

$$\begin{aligned}
\phi_s &= -0.083 \pm 0.041 \pm 0.006\,\text{rad} \\
|\lambda| &= 1.012 \pm 0.016 \pm 0.006 \\
\Gamma_s - \Gamma_d &= -0.0041 \pm 0.0024 \pm 0.0015\,\text{ps}^{-1} \\
\Delta\Gamma_s &= 0.077 \pm 0.008 \pm 0.003\,\text{ps}^{-1} \\
\Delta m_s &= 17.703 \pm 0.059 \pm 0.018\,\text{ps}^{-1} \\
|A_\perp|^2 &= 0.2456 \pm 0.0040 \pm 0.0019 \\
|A_0|^2 &= 0.5186 \pm 0.0029 \pm 0.0023 \\
\delta_\perp - \delta_0 &= 2.64 \pm 0.13 \pm 0.10\,\text{rad} \\
\delta_\parallel - \delta_0 &= 3.06\,^{+\,0.08}_{-\,0.07} \pm 0.04\,\text{rad}
\end{aligned} \tag{6.2}$$

where the first uncertainty is statistical and the second is systematic uncertainty. This result is obtained with the assumption that the penguin-to-tree ratio is independent of the polarisation, this assumption is shown to be a good approximation in section 6.2. The fit projections of the PDF on the background-subtracted distributions of the observables in data are shown in figures 6.1 and 6.2. The correlation parameters obtained from the fit are reported in the table 6.1. The value of ϕ_s is consistent within its uncertainty with the value expected in the SM. The parameter $|\lambda|$ is consistent with one, which means no evidence for direct CP violation in the $B_s^0 \to J/\psi K^+K^-$ decay. The values of the lifetime parameters of the B_s^0 system, Γ_s and $\Delta\Gamma_s$, are consistent with expectations from HQE models.

The observed CP asymmetry in data is shown in figure 6.3, where the asymmetry is defined as $\Gamma(B_s^0(t)) - \Gamma(\overline{B}_s^0(t))$ divided by the sum. Since the CP-even components have a $+\sin(\phi_s)$ factor, while the CP-odd have a $-\sin(\phi_s)$ factor, the sum of the terms can be positive or negative depending on the position of the angular variables. To

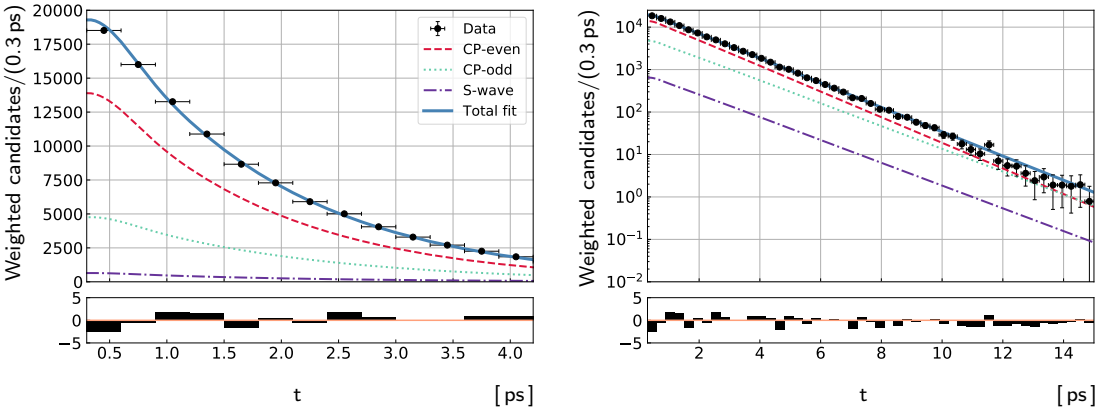

Figure 6.1: Decay-time distributions for background-subtracted $B_s^0 \to J/\psi K^+K^-$ decays (data points) with one-dimensional projections of the PDF at the maximum-likelihood point. The solid blue line shows the total signal contribution, which consists of (long-dashed red) CP-even, (short-dashed green) CP-odd and (dotted-dashed purple) S-wave contributions.

enhance the review of the asymmetry distribution, an event-by-event angular-dependent weight is applied to the data sample. The weight is defined as CP-even fraction minus CP-odd fraction

$$w(\Omega) = \frac{(f_1(\Omega)\cdot N_1 + f_2(\Omega)\cdot N_2) - (f_3(\Omega)\cdot N_3 + f_7(\Omega)\cdot N_7)}{(f_1(\Omega)\cdot N_1 + f_2(\Omega)\cdot N_2) + (f_3(\Omega)\cdot N_3 + f_7(\Omega)\cdot N_7)}. \tag{6.3}$$

where the individual terms are defined in reference [98]. The weight can correct the sign of the sum of the terms to be always the same and can give higher weight to the event that has larger asymmetry.

The PDF, shown in figure 6.3, is produced by means of pseudoexperiments with inputs from the baseline fit result, where the angular efficiency, decay-time efficiency and time-resolution effects are taken into account and perfect tagging is assumed. To account for tagging effects, the resulting distribution is multiplied by the average dilution factor, $(1 - 2\langle\omega_{\text{tag}}\rangle)$, obtained by applying the tagging calibration on the data sample.

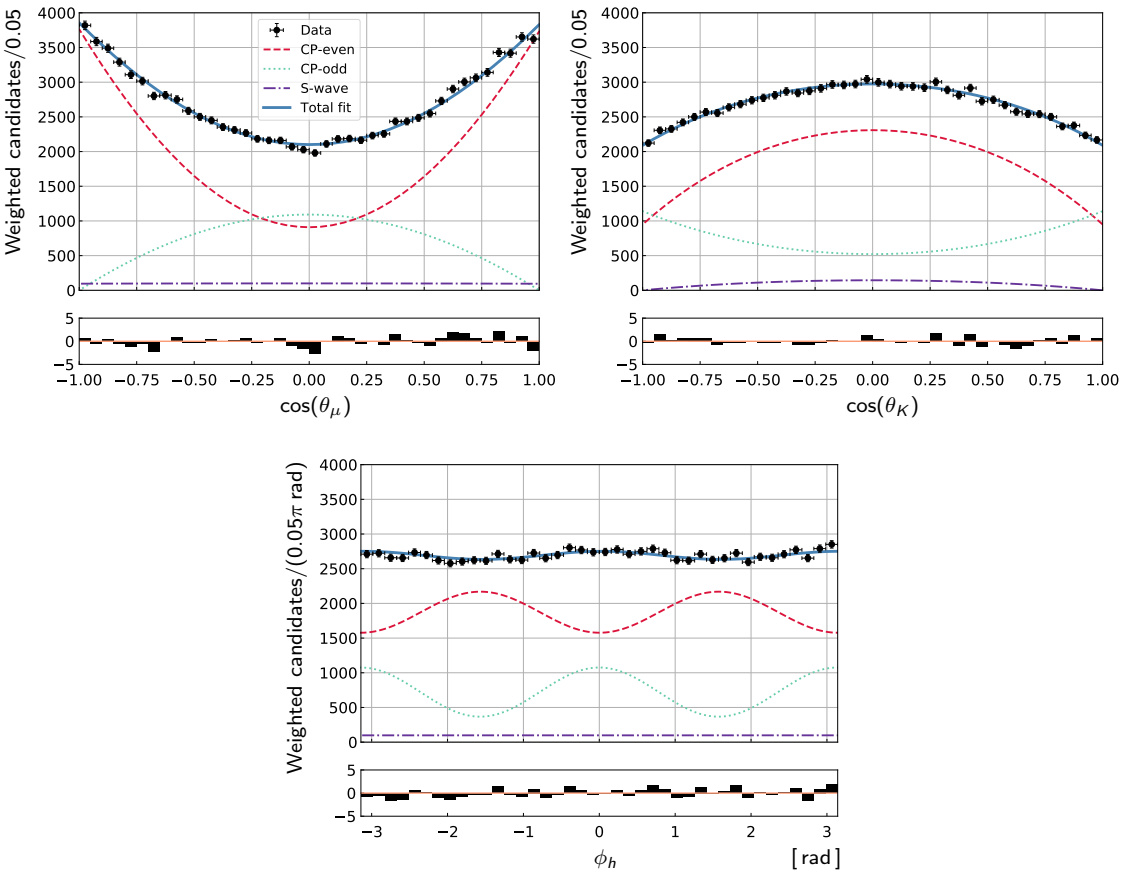

Figure 6.2: Helicity-angle distributions for background-subtracted $B_s^0 \to J/\psi K^+K^-$ decays (data points) with one-dimensional projections of the PDF at the maximum-likelihood point. The solid blue line shows the total signal contribution, which consists of (long-dashed red) CP-even, (short-dashed green) CP-odd and (dotted-dashed purple) S-wave contributions.

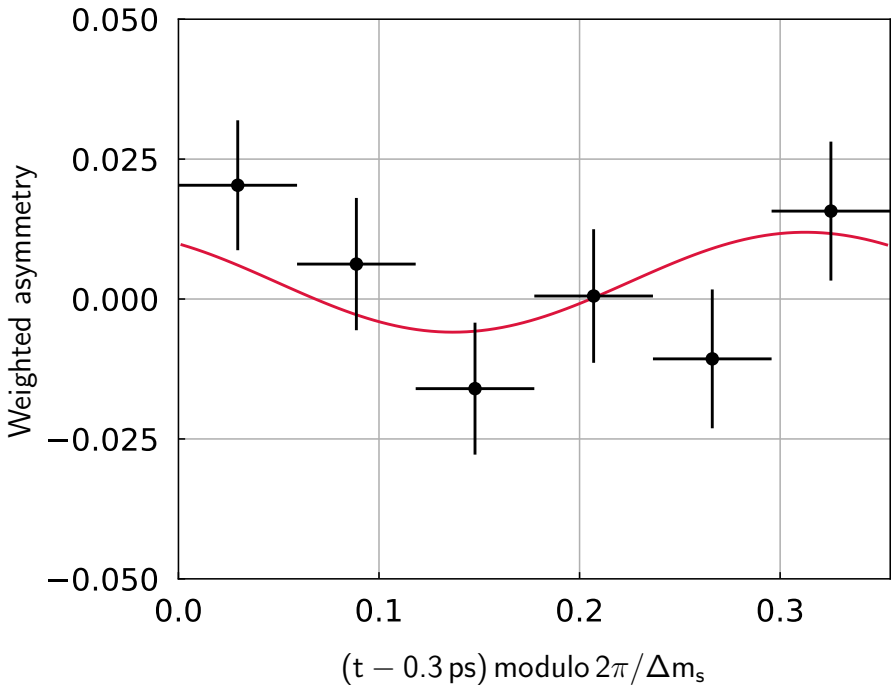

Figure 6.3: Observed CP asymmetry in data (black points) folded in one B_s^0 oscillation period. The PDF is shown with red line.

6.2 Polarisation dependent result

The fit is repeated allowing for different ϕ_s and $|\lambda|$ values for each possible polarisation of the final state in order to allow for the possible polarisation dependence of the amount of the penguin contribution. The results obtained assuming both polarisation (in)dependence are shown in table 6.2. The results are consistent with no polarisation dependence.

Table 6.1: Correlation matrix including the statistical and systematic correlations between the parameters.

	ϕ_s	$\lvert\lambda\rvert$	$\Gamma_s - \Gamma_d$	$\Delta\Gamma_s$	Δm_s	$\lvert A_\perp\rvert^2$	$\lvert A_0\rvert^2$	$\delta_\perp - \delta_0$	$\delta_\parallel - \delta_0$
ϕ_s	1.00	0.10	−0.02	−0.03	0.02	0.01	−0.01	0.07	0.00
$\lvert\lambda\rvert$		1.00	0.04	−0.04	−0.05	0.03	−0.02	−0.04	0.03
$\Gamma_s - \Gamma_d$			1.00	−0.35	0.04	0.28	−0.17	0.01	0.01
$\Delta\Gamma_s$				1.00	−0.01	−0.62	0.40	−0.05	−0.01
Δm_s					1.00	0.01	−0.01	0.62	0.02
$\lvert A_\perp\rvert^2$						1.00	−0.67	0.03	0.01
$\lvert A_0\rvert^2$							1.00	−0.06	−0.06
$\delta_\perp - \delta_0$								1.00	0.28
$\delta_\parallel - \delta_0$									1.00

Table 6.2: Parameter estimates obtained for the fit with polarisation-dependent and -independent ϕ_s and $|\lambda|$. Only statistical uncertainties are shown.

	Polarisation	
	independent	dependent
ϕ_s^0[rad]	-0.083 ± 0.041	-0.081 ± 0.043
$\phi_s^{\parallel} - \phi_s^0$[rad]		-0.045 ± 0.047
$\phi_s^{\perp} - \phi_s^0$[rad]		-0.077 ± 0.059
$\phi_s^S - \phi_s^0$[rad]		0.021 ± 0.042
$\lvert\lambda^0\rvert$	1.012 ± 0.016	0.96 ± 0.05
$\lvert\lambda^{\parallel}/\lambda^0\rvert$		0.98 ± 0.08
$\lvert\lambda^{\perp}/\lambda^0\rvert$		1.23 ± 0.16
$\lvert\lambda^S/\lambda^0\rvert$		1.27 ± 0.16
$\Delta\Gamma_d^s$[ps^{-1}]	-0.0041 ± 0.0024	-0.0043 ± 0.0024
$\Delta\Gamma_s$[ps^{-1}]	0.077 ± 0.008	0.078 ± 0.008
Δm_s[ps^{-1}]	17.703 ± 0.059	17.713 ± 0.060
$\lvert A_{\perp}\rvert^2$	0.246 ± 0.004	0.206 ± 0.025
$\lvert A_0\rvert^2$	0.519 ± 0.003	0.542 ± 0.018
$\delta_{\perp} - \delta_0$[rad]	2.64 ± 0.13	2.60 ± 0.15
$\delta_{\parallel} - \delta_0$[rad]	3.06 ± 0.08	3.03 ± 0.08
F_{S1}	0.492 ± 0.043	0.437 ± 0.053
F_{S2}	0.041 ± 0.008	0.033 ± 0.008
F_{S3}	0.004 ± 0.002	0.004 ± 0.002
F_{S4}	0.007 ± 0.005	0.004 ± 0.004
F_{S5}	0.073 ± 0.013	0.058 ± 0.014
F_{S6}	0.152 ± 0.018	0.129 ± 0.020
$\delta_{S1} - \delta_{\perp}$[rad]	2.21 ± 0.18	2.31 ± 0.18
$\delta_{S2} - \delta_{\perp}$[rad]	1.56 ± 0.30	1.56 ± 0.29
$\delta_{S3} - \delta_{\perp}$[rad]	1.09 ± 0.45	1.10 ± 0.39
$\delta_{S4} - \delta_{\perp}$[rad]	-0.28 ± 0.18	-0.30 ± 0.25
$\delta_{S5} - \delta_{\perp}$[rad]	-0.54 ± 0.09	-0.50 ± 0.11
$\delta_{S6} - \delta_{\perp}$[rad]	-1.10 ± 0.14	-0.99 ± 0.14
p_0^{os}	0.3892 ± 0.0028	0.3892 ± 0.0028
Δp_0^{os}	0.0090 ± 0.0014	0.0090 ± 0.0014
p_1^{os}	0.846 ± 0.027	0.846 ± 0.027
Δp_1^{os}	0.015 ± 0.012	0.015 ± 0.012
p_0^{ss}	0.443 ± 0.007	0.442 ± 0.007
Δp_0^{ss}	0.002 ± 0.029	0.002 ± 0.029
p_1^{ss}	0.609 ± 0.088	0.614 ± 0.088
Δp_1^{ss}	0.000 ± 0.030	0.000 ± 0.030

6.3 Combination

To improve the statistical precision, the obtained results are combined with related Run 1 and Run 2 measurements performed on data collected in the LHCb experiment. The combination of results is performed taking into account all statistical correlations, all systematic errors and their correlations, and correlations between different run periods.

The results used in the combination are Run 2 result with $B_s^0 \to J/\psi\pi^+\pi^-$ [99] decays, and the Run 1 results from $B_s^0 \to J/\psi K^+K^-$ [89] decays, $B_s^0 \to J/\psi\pi^+\pi^-$ [100] decays, $B_s^0 \to J/\psi K^+K^-$ for the m_{KK} region above 1.05 GeV/c^2 [101], $B_s^0 \to \psi(2S)\phi$ [102] and $B_s^0 \to D_s^+D_s^-$ [103] decays. The technical details about the combination can be found in reference [104]. The combined values for the physics parameters are

$$\begin{aligned} \phi_s &= -0.042 \pm 0.025\,\text{rad} \\ |\lambda| &= 0.993 \pm 0.010 \\ \Gamma_s &= 0.6563 \pm 0.0021\,\text{ps}^{-1} \\ \Delta\Gamma_s &= 0.0813 \pm 0.0048\,\text{ps}^{-1} \end{aligned} \tag{6.4}$$

The results and their combined value for ϕ_s and $\Delta\Gamma_s$, and the corresponding SM expectations, are shown in figure 6.4.

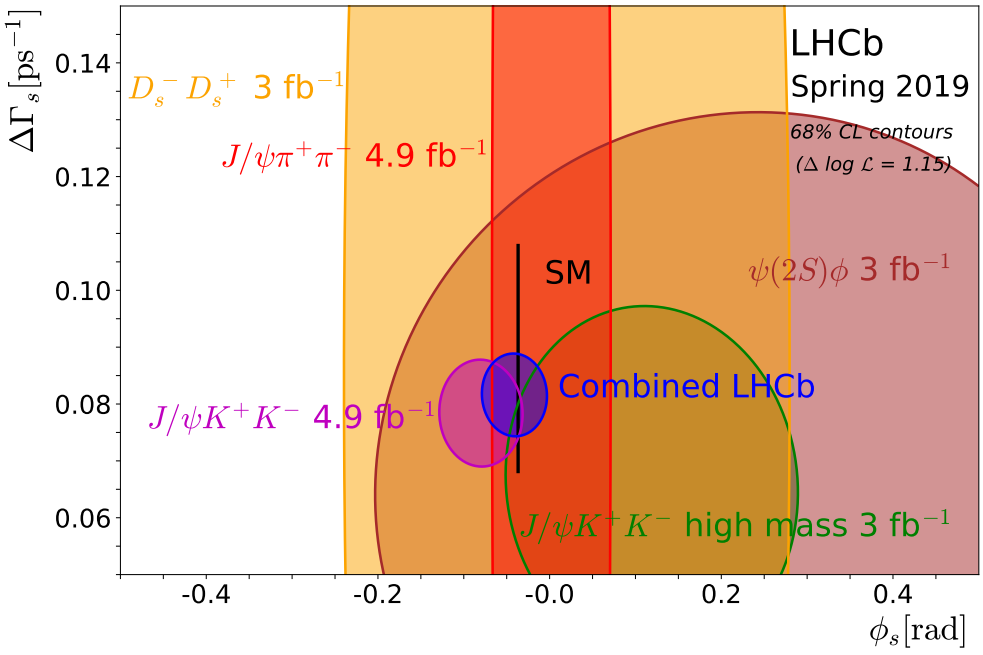

Figure 6.4: Regions of 68% confidence level in the ϕ_s-$\Delta\Gamma_s$ plane for the individual LHCb measurements and a combined contour (in blue). The prediction for the ϕ_s and $\Delta\Gamma_s$ values is indicated by the thin black rectangle.

Conclusions and outlook

A flavour-tagged decay-time-dependent angular analysis of $B_s^0 \to J/\psi K^+K^-$ decays has been performed, using $1.9\,\text{fb}^{-1}$ of pp collision data recorded by the LHCb experiment during the 2015 and 2016 runs of the LHC. Approximately 117 000 signal decays are selected, with a decay-time resolution of about 45 fs and a tagging power of 4.7%. The CP-violating phase ϕ_s is measured to be $-0.083 \pm 0.041 \pm 0.006$ rad, the decay width difference of the B_s^0 mass eigenstates, $\Delta\Gamma_s = 0.077 \pm 0.008 \pm 0.003\,\text{ps}^{-1}$, and the difference of the average decay widths of the B_s^0 and B^0 mesons, $\Gamma_s - \Gamma_d = -0.0041 \pm 0.0024 \pm 0.0015\,\text{ps}^{-1}$. Using the known value for the B^0 meson lifetime 1.520 ± 0.004 ps [90], the ratio of B_s^0 and B^0 meson decay widths is measured to be $\Gamma_s/\Gamma_d = 0.9938 \pm 0.0036 \pm 0.0023$. All results are shown with first the statistical and second the systematic uncertainty. These are the single most precise measurements of these quantities to date. In addition, the mass difference between the B_s^0 mass eigenstates is measured to be $\Delta m_s = 17.703 \pm 0.059 \pm 0.018\,\text{ps}^{-1}$. All results are consistent with theoretical predictions based on the SM [8, 9]. The CP-violating parameters are also determined assuming that they are not the same for all $B_s^0 \to J/\psi K^+K^-$ polarisation states and no polarisation dependence is observed.

The measurements presented here for the parameters ϕ_s, $|\lambda|$, $\Gamma_s - \Gamma_d$, $\Delta\Gamma_s$, Δm_s, $|A_\perp|^2$, $|A_0|^2$, $\delta_\perp - \delta_0$ and $\delta_\parallel - \delta_0$ are consistent with those from $B_s^0 \to J/\psi K^+K^-$ decays obtained using data collected by the LHCb experiment during Run 1 of the LHC [89]. The two sets of measurements are combined accounting for the statistical and systematic correlations between parameters in each and the systematic correlations between the two run periods. The combined values are $\phi_s = -0.081 \pm 0.032$ rad, $|\lambda| = 0.994 \pm 0.013$, $\Gamma_s = 0.6572 \pm 0.0023\,\text{ps}^{-1}$, $\Delta\Gamma_s = 0.0777 \pm 0.0062\,\text{ps}^{-1}$ and $\Delta m_s = 17.694 \pm 0.042\,\text{ps}^{-1}$. The value of ϕ_s is 2.5 standard deviations from zero and consistent with theoretical predictions based on the SM [8, 9]. Assuming the central value of ϕ_s remains the same, the statistical power of the full Run 2 dataset will be such that is is expected to provide the first evidence of CP violation in the $B_s^0 \to J/\psi K^+K^-$ decay.

The results are further combined with the recent results from $B_s^0 \to J/\psi\pi^+\pi^-$ [99], and the Run 1 results from $B_s^0 \to J/\psi\pi^+\pi^-$ [100], $B_s^0 \to J/\psi K^+K^-$ for the K^+K^- invariant mass region above $1.05\,\text{GeV}/c^2$ [101], $B_s^0 \to \psi(2S)\phi$ [102] and $B_s^0 \to D_s^+D_s^-$ [103]. The combined values are $\phi_s = -0.042 \pm 0.025$ rad, $|\lambda| = 0.993 \pm 0.010$, $\Gamma_s = 0.6563 \pm 0.0021\,\text{ps}^{-1}$ and $\Delta\Gamma_s = 0.0813 \pm 0.0048\,\text{ps}^{-1}$. These values are consistent with theoretical predictions based on the SM [8, 9]. In particular, the value of ϕ_s is consistent with the non-zero CP-violating phase predicted within the SM, but also with

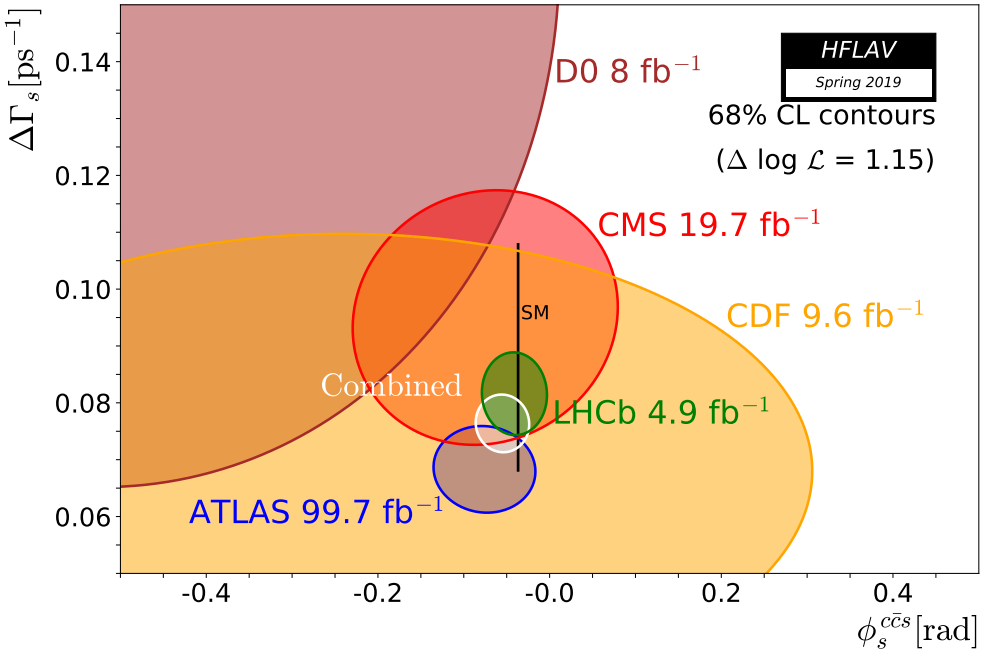

Figure 6.5: Regions of 68% confidence level in the ϕ_s-$\Delta\Gamma_s$ plane for measurements from various experiments and a combined contour (in white). The prediction for the ϕ_s and $\Delta\Gamma_s$ values is indicated by the thin black rectangle.

the hypothesis of no CP-violation in the interference of B_s^0 meson mixing and decay. The parameter $|\lambda|$ is consistent with unity, implying no evidence for direct CP violation in $B_s^0 \to J/\psi K^+K^-$ decays.

Measurements of ϕ_s and $\Delta\Gamma_s$ has been performed by various experiments, apart from LHCb, namely by the ATLAS [105], the CMS [106], the D0 [107] and CDF [108] collaborations. The results from all these experiments are combined and shown in white in figure 6.5.

The measurement of ϕ_s with the full Run 2 (2015–2018) data collected by the LHCb detector is currently in progress. The approximate statistical precision of the measurement is expected to be around 1.7 times smaller than the current measurement based on 2015–2016 data only. This approximation only takes into account the linear scaling of the event yield with the recorded integrated luminosity. However, with the development of the new inclusive flavour tagging algorithm [109], the statistical improvement can be made larger. Apart from the flavour tagging, there are several analysis techniques that can be potentially improved. For instance, the current measurement relies on binning in m_{KK} for the estimation of the S-wave coupling factors. The m_{KK} mass can instead be used as one of the observables in the fit, eliminating the arbitrary choice of the binning scheme. Another point is the determination of the non-uniform decay-time acceptance shape, which for lower decay times is caused by the decay-time biasing selection criteria and for higher decay-times is caused by the VELO reconstruction inefficiency. Currently, both effects are assessed simultaneously and the acceptance shape is determined using the control channel in data. However, the VELO

reconstruction efficiency is directly dependent on the distance of the closest approach to the z-axis of final state tracks rather than on the decay time itself. Therefore, one could define a parametrisation for the upper decay time as a function of the distances of closest approach to the z-axis of the B_s^0 daughter particles. The parametrisation can be determined from a control channel, such as $B^0 \to J/\psi K^{*0}$ and then the signal can be corrected correspondingly. The other potential effect that can start playing a role with growing statistics is finite resolution of the helicity angles. Current measurement assumes perfect angular resolution, which is not the case. The author is in the process of developing a method to include the finite angular resolution in the total PDF to perform a more accurate measurement.

In the upcoming years with the growing precision it might become possible to observe a deviation of the ϕ_s value from the SM expectation and to indirectly discover New Physics. Whether there is NP or not, it is up to nature to decide. What is in the power of experimentalists is to constantly improve experimental techniques and to have all systematic effects under control.

Appendix A

Mass fit to simulated sample

The results of the mass fit to only signal and FSR events, that is used to determine the tail parameters of the signal distribution, are shown in figures A.1 to A.4. Table A.1 summarises the obtained fit parameters. The resulting tail parameters of the double-sided CB function, α_1, α_2, n_1, n_2, are fixed when performing the fit on the full simulated sample (that includes signal, FSR and ghost events), with an exponential introduced as background PDF. The corresponding plots are shown in figures A.5 to A.8.

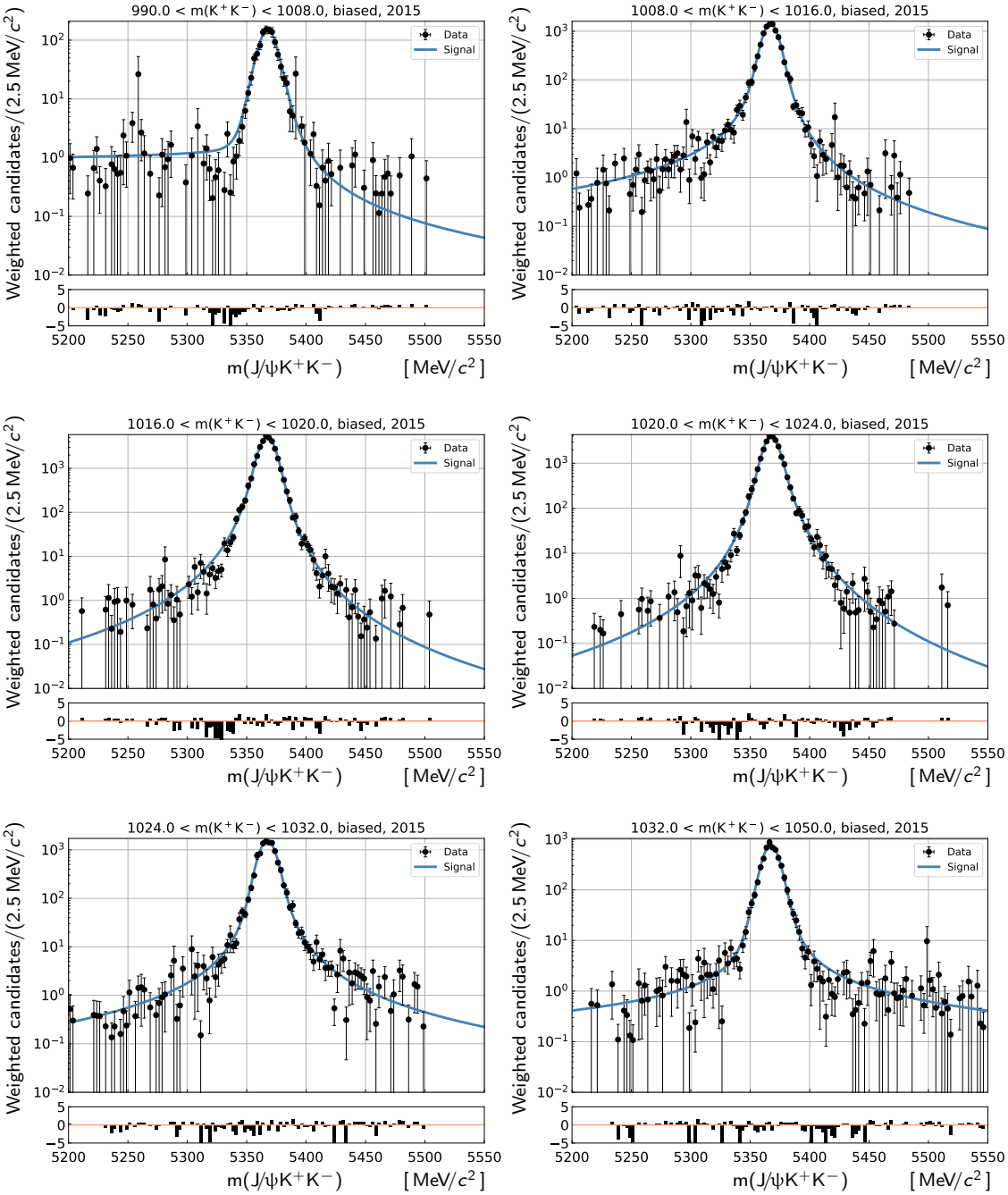

Figure A.1: Fits to the $m(J/\psi K^+K^-)$ distribution divided into six bins in m_{KK}, namely [990, 1008, 1016, 1020, 1024, 1032, 1050] MeV/c^2, obtained in the biased signal and FSR categories of the 2015 simulation sample (solid blue line) and pull plot.

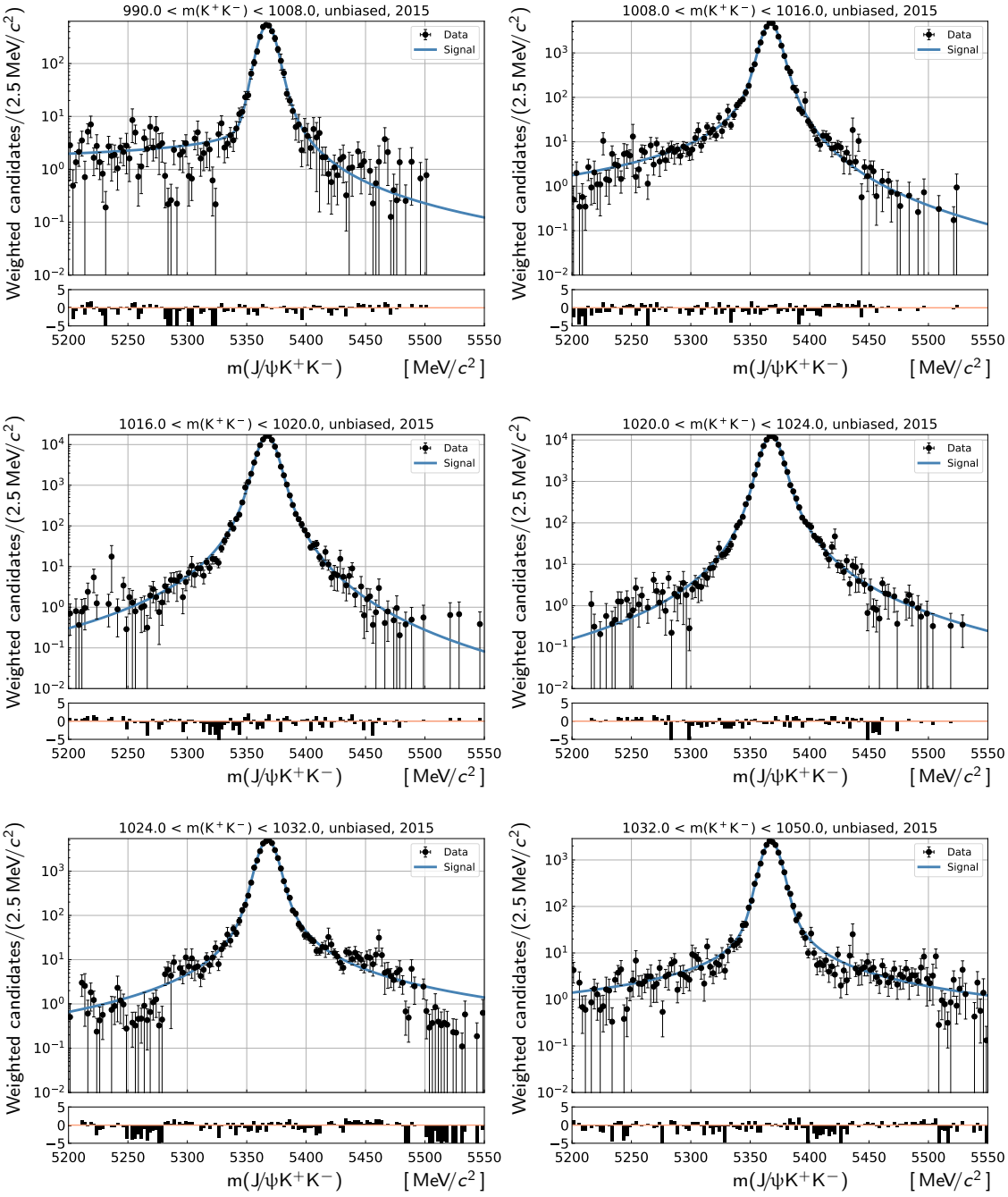

Figure A.2: Fit to the $m(J/\psi K^+K^-)$ distribution divided into six bins in m_{KK}, namely [990, 1008, 1016, 1020, 1024, 1032, 1050] MeV/c^2, obtained in unbiased signal and FSR category of the 2015 simulation sample (solid blue line) and pull plot.

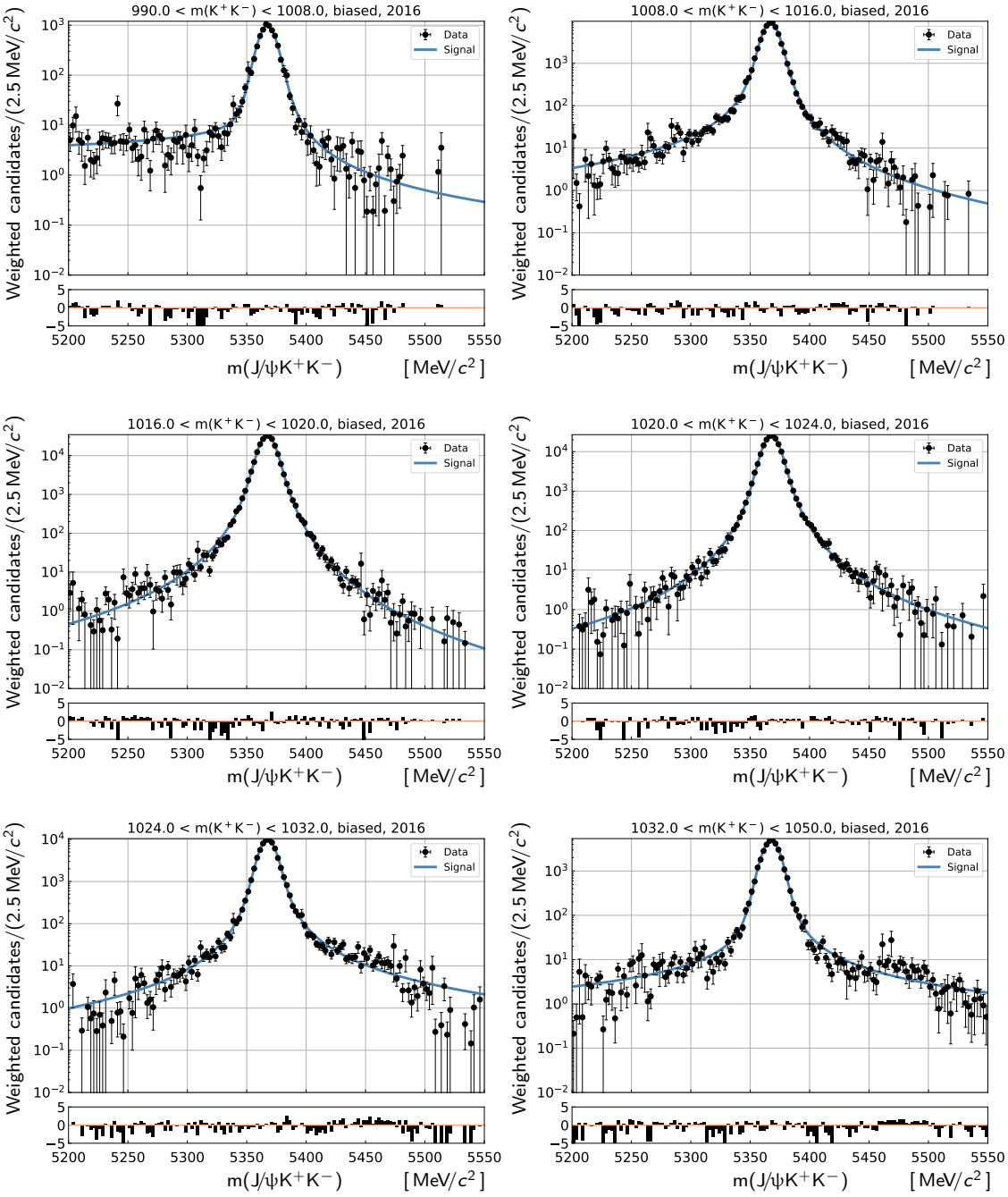

Figure A.3: Fit to the m(J/ψK$^+$K$^-$) distribution divided into six bins in m_{KK}, namely [990, 1008, 1016, 1020, 1024, 1032, 1050] MeV/c^2, obtained in biased signal and FSR category of the 2016 simulation sample (solid blue line) and pull plot.

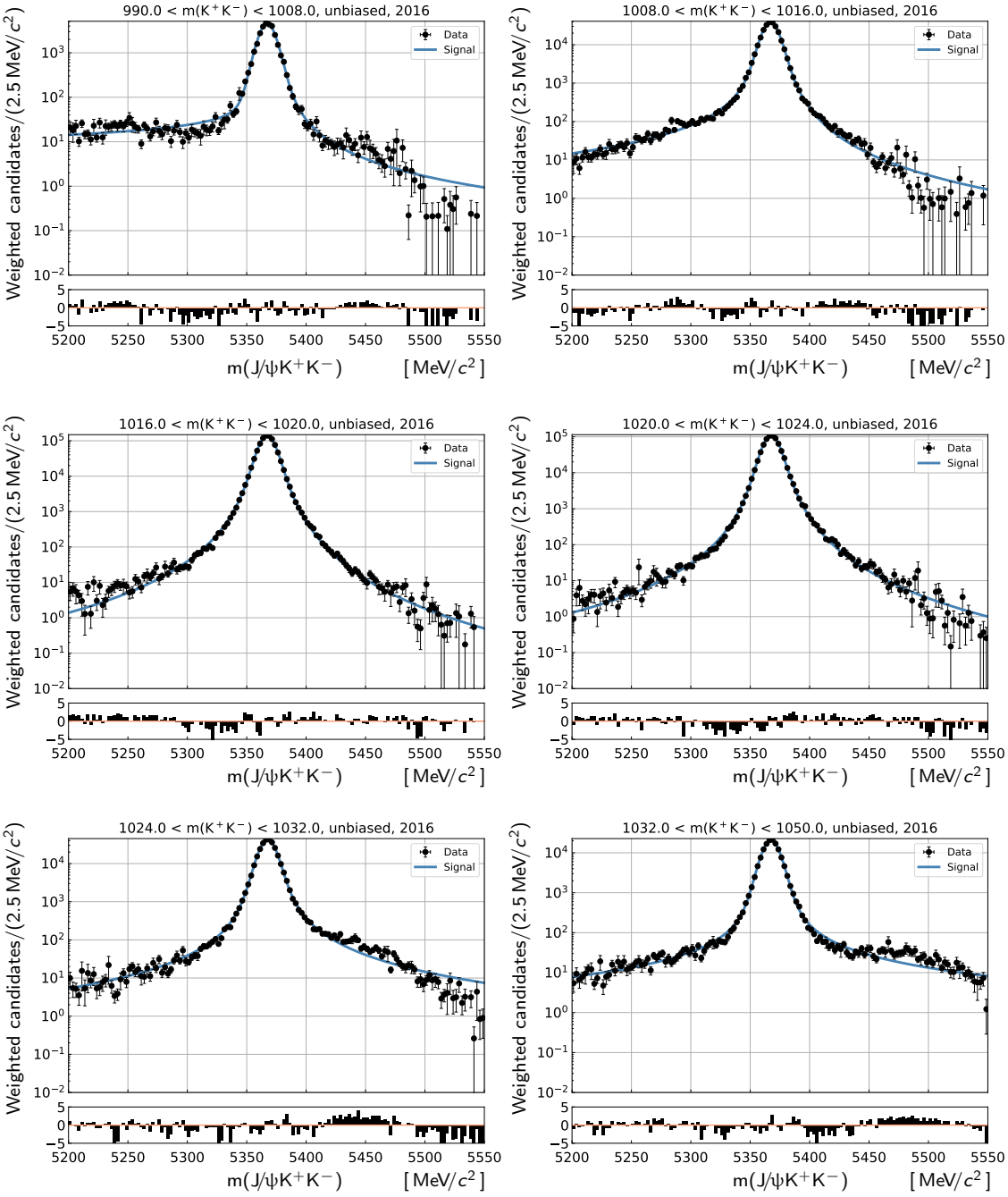

Figure A.4: Fits to the $m(J/\psi K^+K^-)$ distribution divided into six bins in m_{KK}, namely [990, 1008, 1016, 1020, 1024, 1032, 1050] MeV/c^2, obtained in unbiased signal and FSR category of the 2016 simulation sample (solid blue line) and pull plot.

Table A.1: Parameters from the mass fit to the 2015 and 2016 simulated biased (b) and unbiased (ub) samples.

	Bins	α_1	α_2	n_1	n_2	s_1	s_2
2015	1b	2.90 ± 1.30	0.13 ± 0.93	2.23 ± 0.38	1.64 ± 0.84	0.69 ± 0.41	0.115 ± 0.082
	2b	2.08 ± 0.17	1.63 ± 0.33	2.09 ± 0.26	2.35 ± 0.71	0.88 ± 0.50	0.047 ± 0.090
	3b	1.98 ± 0.12	3.21 ± 0.51	2.14 ± 0.22	3.50 ± 1.20	0.95 ± 0.10	0.036 ± 0.018
	4b	2.06 ± 0.14	3.33 ± 0.80	1.77 ± 0.14	4.13 ± 0.93	0.79 ± 0.20	0.062 ± 0.036
	5b	2.19 ± 0.19	1.88 ± 0.48	2.04 ± 0.21	2.09 ± 0.56	1.11 ± 0.17	0.015 ± 0.025
	6b	2.59 ± 0.52	1.02 ± 0.75	2.35 ± 0.26	1.22 ± 0.41	0.59 ± 0.78	0.100 ± 0.140
	1ub	2.77 ± 0.13	0.33 ± 0.09	2.06 ± 0.27	1.83 ± 0.59	0.95 ± 0.38	0.042 ± 0.071
	2ub	2.09 ± 0.10	1.65 ± 0.21	1.92 ± 0.13	3.00 ± 0.52	0.84 ± 0.20	0.056 ± 0.035
	3ub	2.10 ± 0.13	3.09 ± 0.51	2.04 ± 0.13	3.78 ± 0.75	0.87 ± 0.02	0.051 ± 0.005
	4ub	2.17 ± 0.14	3.20 ± 0.63	2.01 ± 0.10	3.09 ± 0.44	0.93 ± 0.02	0.042 ± 0.003
	5ub	2.22 ± 0.11	1.96 ± 0.27	2.12 ± 0.09	1.69 ± 0.18	0.95 ± 0.20	0.037 ± 0.036
	6ub	2.47 ± 0.14	1.11 ± 0.21	2.28 ± 0.13	1.30 ± 0.20	0.89 ± 0.29	0.045 ± 0.052
2016	1b	2.66 ± 0.15	0.40 ± 0.14	2.23 ± 0.21	1.57 ± 0.43	0.68 ± 0.11	0.103 ± 0.018
	2b	2.03 ± 0.12	1.74 ± 0.24	2.05 ± 0.09	2.50 ± 0.37	0.93 ± 0.25	0.044 ± 0.044
	3b	2.02 ± 0.04	3.37 ± 0.23	1.97 ± 0.06	4.17 ± 0.44	0.86 ± 0.05	0.052 ± 0.009
	4b	2.11 ± 0.08	3.28 ± 0.36	2.01 ± 0.06	3.28 ± 0.29	0.92 ± 0.06	0.047 ± 0.011
	5b	2.17 ± 0.07	2.14 ± 0.20	2.06 ± 0.05	1.87 ± 0.11	0.87 ± 0.08	0.053 ± 0.014
	6b	2.52 ± 0.08	1.12 ± 0.13	2.33 ± 0.08	1.38 ± 0.14	0.96 ± 0.09	0.044 ± 0.016
	1ub	2.63 ± 0.03	0.47 ± 0.02	2.22 ± 0.10	1.71 ± 0.22	0.92 ± 0.17	0.050 ± 0.031
	2ub	2.09 ± 0.03	1.68 ± 0.06	2.08 ± 0.04	2.57 ± 0.14	0.90 ± 0.04	0.049 ± 0.008
	3ub	2.03 ± 0.03	3.60 ± 0.16	2.02 ± 0.03	4.05 ± 0.20	0.89 ± 0.02	0.047 ± 0.003
	4ub	2.12 ± 0.05	3.33 ± 0.24	1.95 ± 0.05	3.64 ± 0.27	0.89 ± 0.01	0.048 ± 0.002
	5ub	2.24 ± 0.03	1.97 ± 0.08	2.05 ± 0.03	1.98 ± 0.07	0.86 ± 0.03	0.056 ± 0.005
	6ub	2.34 ± 0.05	1.37 ± 0.08	2.31 ± 0.04	1.37 ± 0.07	0.85 ± 0.07	0.059 ± 0.012

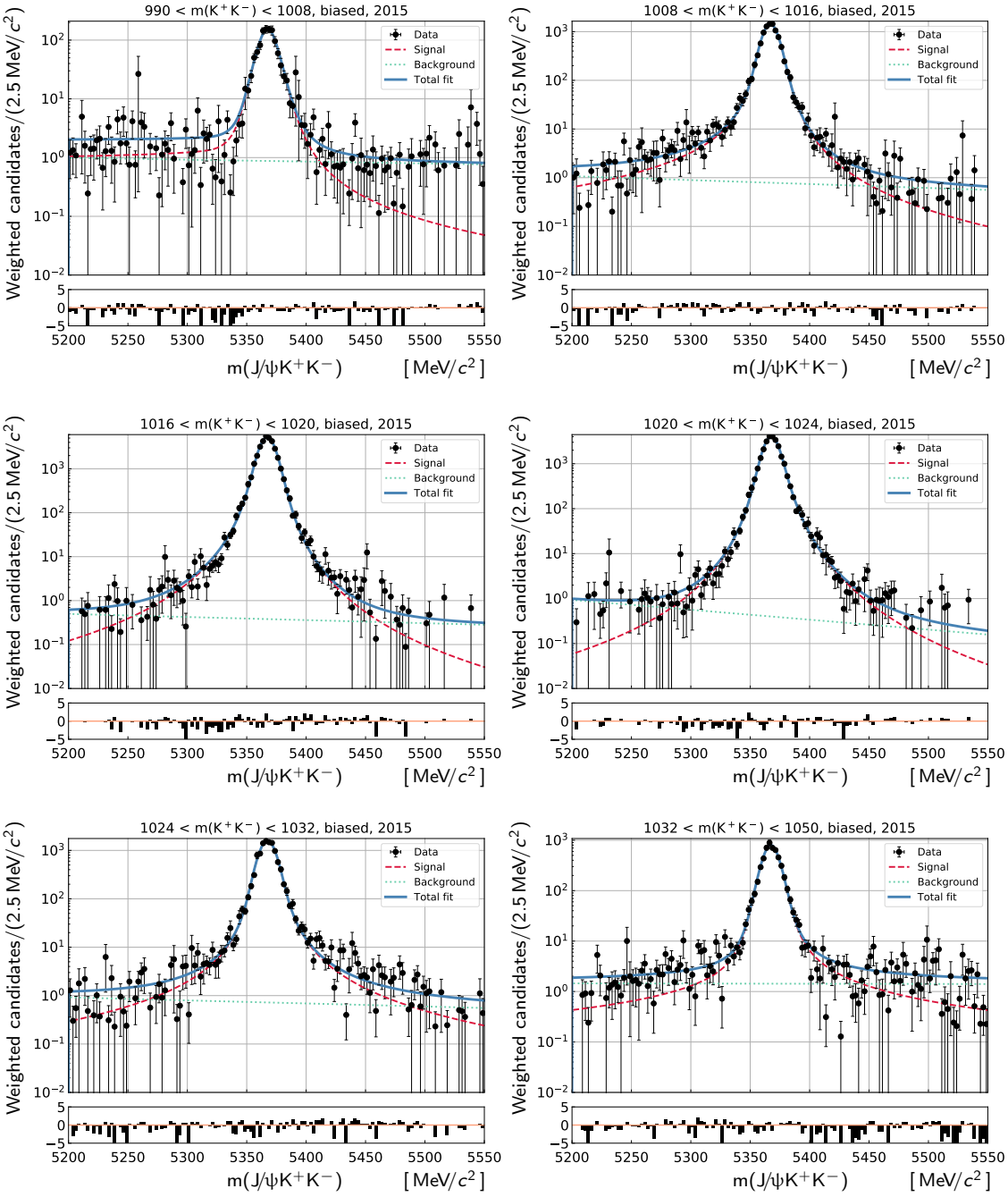

Figure A.5: Fits to the $m(J/\psi K^+K^-)$ distribution divided into six bins in m_{KK}, namely [990, 1008, 1016, 1020, 1024, 1032, 1050] MeV/c^2, obtained in biased 2015 simulation sample (solid blue line) and pull plot using a Crystal Ball (dashed blue line) for the signal and an exponential distribution for the background (dashed green line).

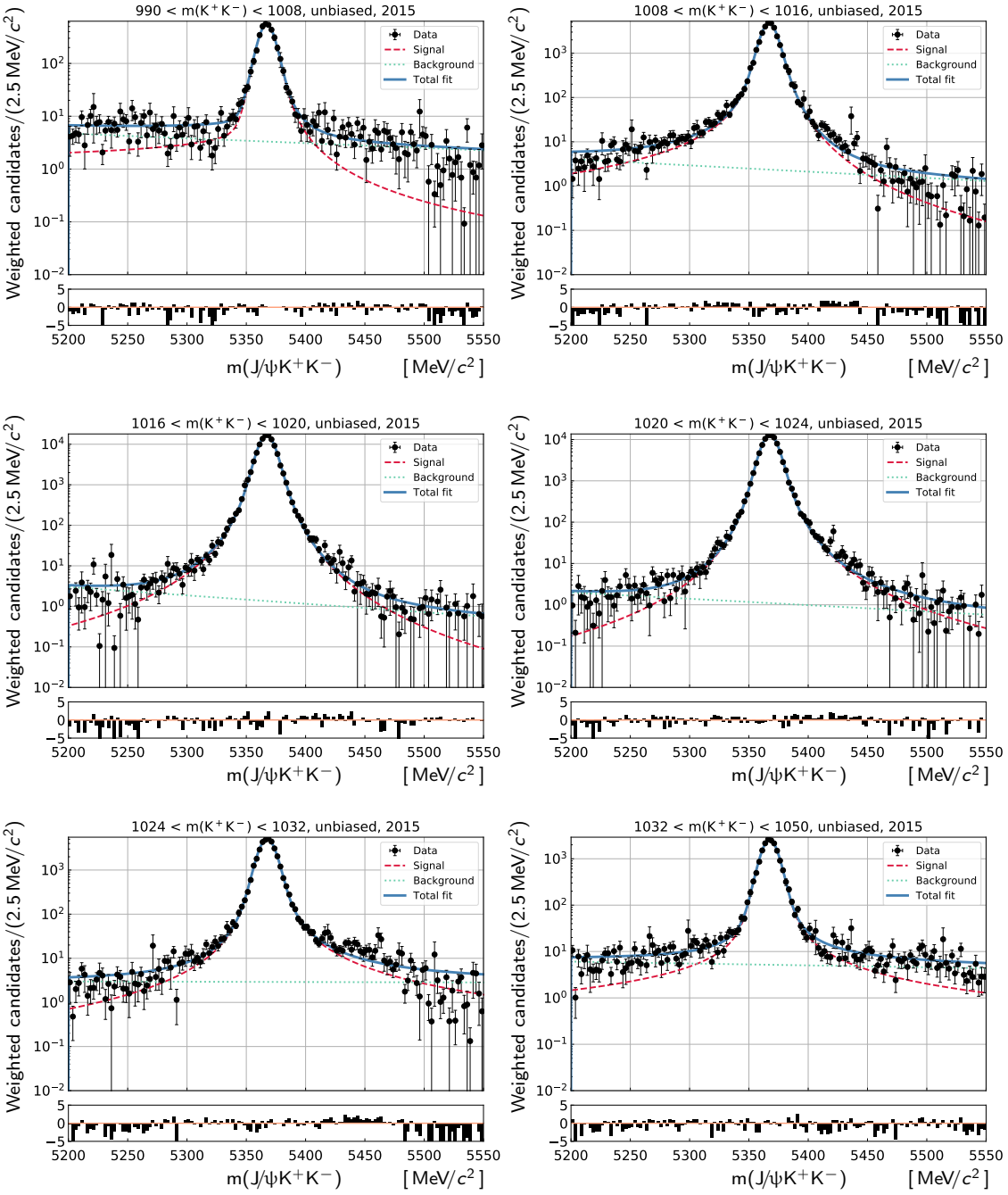

Figure A.6: Fits to the $m(J/\psi K^+K^-)$ distribution divided into six bins in m_{KK}, namely [990, 1008, 1016, 1020, 1024, 1032, 1050] MeV/c^2, obtained in unbiased 2015 simulation sample (solid blue line) and pull plot using a Crystal Ball (dashed blue line) for the signal.

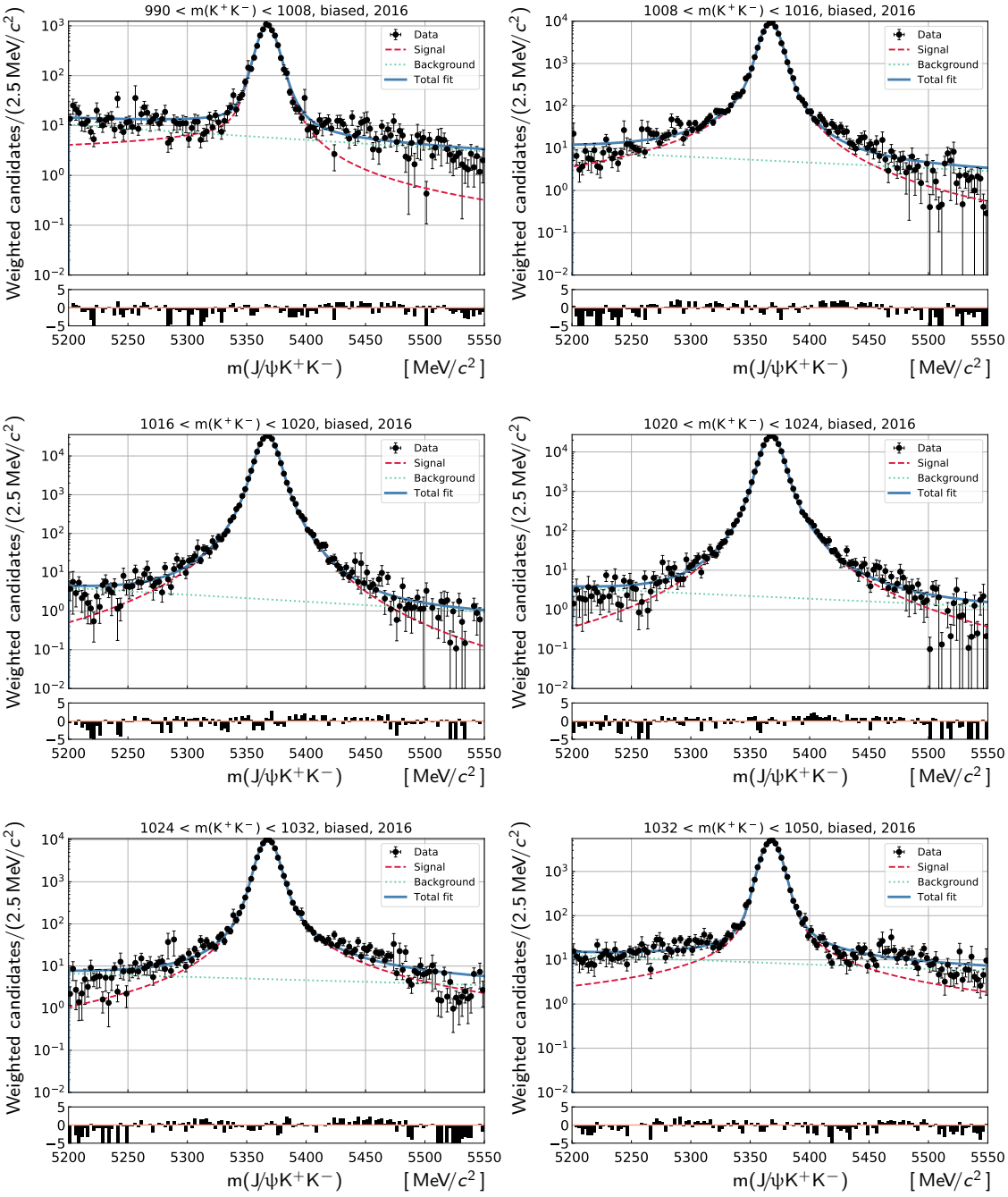

Figure A.7: Fits to the $m(J/\psi K^+K^-)$ distribution divided into six bins in m_{KK}, namely [990, 1008, 1016, 1020, 1024, 1032, 1050] MeV/c^2, obtained in biased 2016 simulation sample (solid blue line) and pull plot using a Crystal Ball (dashed blue line) for the signal and an exponential distribution for the background (dashed green line).

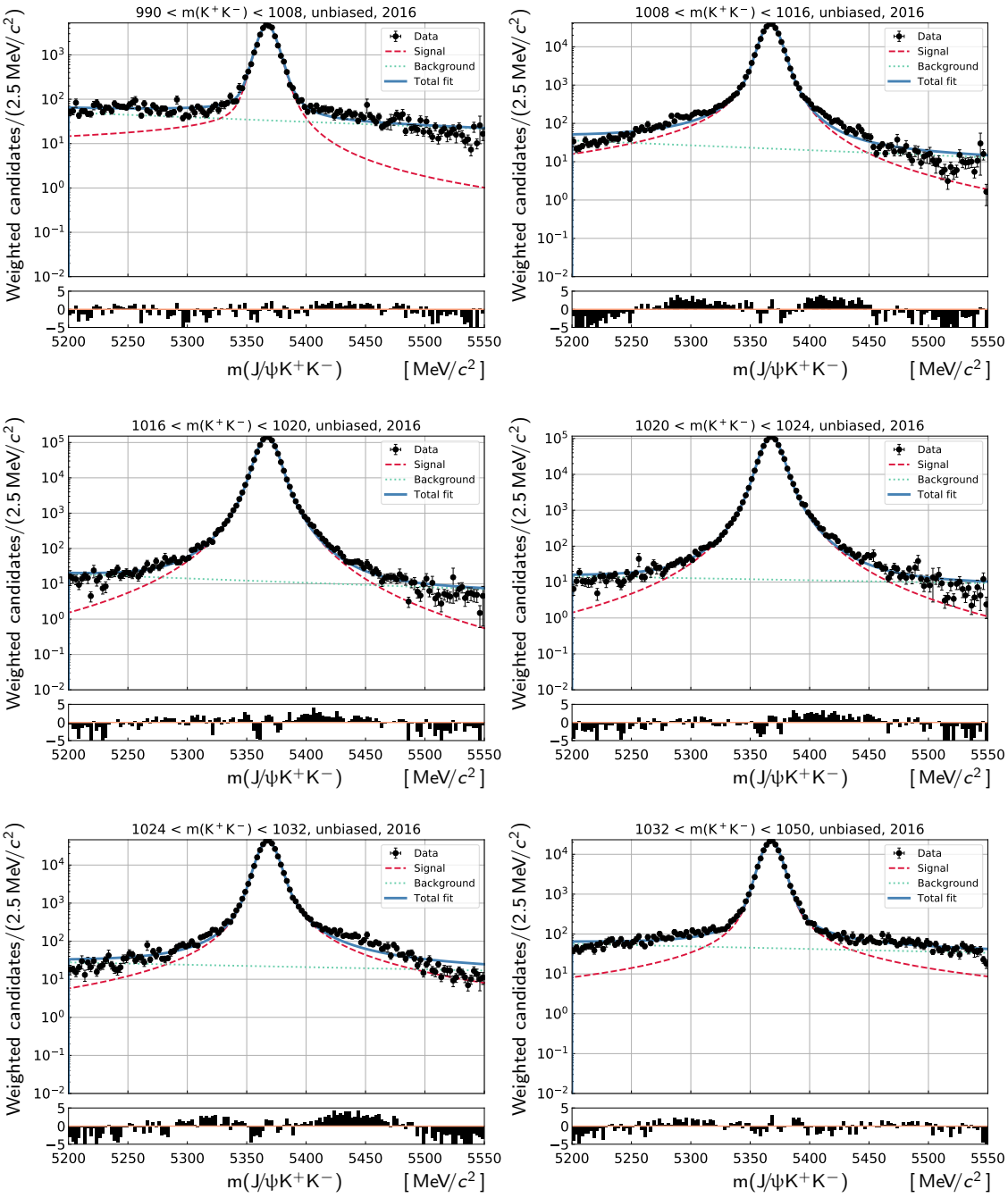

Figure A.8: Fits to the $m(J/\psi K^+K^-)$ distribution divided into six bins in m_{KK}, namely [990, 1008, 1016, 1020, 1024, 1032, 1050] MeV/c^2, obtained in unbiased 2016 simulation sample (solid blue line) and pull plot using a Crystal Ball (dashed blue line) for the signal and an exponential distribution for the background (dashed green line).

Bibliography

[1] T. P. Cheng and L. F. Li, *Gauge theory of elementary particle physics*, 1984.

[2] T. L. Chow, *Gravity, Black Holes, and the Very Early Universe: An Introduction to General Relativity and Cosmology*, Springer New York, 2007.

[3] A. D. Sakharov, *Violation of CP Invariance, C asymmetry, and baryon asymmetry of the universe*, Pisma Zh. Eksp. Teor. Fiz. **5** (1967) 32, [JETP Lett.5,24(1967); Sov. Phys. Usp.34,no.5,392(1991); Usp. Fiz. Nauk161,no.5,61(1991)].

[4] J. Schwinger, *The theory of quantized fields*, Phys. Rev. **82** (1951) 914.

[5] P. Huet and E. Sather, *Electroweak baryogenesis and standard model CP violation*, Phys. Rev. **D51** (1995) 379, arXiv:hep-ph/9404302.

[6] S. L. Glashow, J. Iliopoulos, and L. Maiani, *Weak Interactions with Lepton-Hadron Symmetry*, Phys. Rev. **D2** (1970) 1285.

[7] Particle Data Group, M. Tanabashi *et al.*, *Review of particle physics*, Phys. Rev. D **98** (2018) 030001.

[8] CKMfitter Group, J. Charles *et al.*, *CP violation and the CKM matrix: Assessing the impact of the asymmetric B factories*, Eur. Phys. J. **C41** (2005) 1, arXiv:hep-ph/0406184.

[9] UTfit collaboration, M. Bona *et al.*, *The unitarity triangle fit in the standard model and hadronic parameters from lattice QCD: A reappraisal after the measurements of* Δm_s *and* $BR(B \to \tau\nu_\tau)$, JHEP **10** (2006) 081, arXiv:hep-ph/0606167, updated results and plots available at http://www.utfit.org/.

[10] LHCb collaboration, R. Aaij *et al.*, *LHCb detector performance*, Int. J. Mod. Phys. **A30** (2015) 1530022, arXiv:1412.6352.

[11] L. Evans and P. Bryant, *LHC Machine*, JINST **3** (2008) S08001.

[12] KTeV collaboration, A. Alavi-Harati *et al.*, *Observation of direct CP violation in* $K_{S,L} \to \pi\pi$ *decays*, Phys. Rev. Lett. **83** (1999) 22, arXiv:hep-ex/9905060.

[13] Belle collaboration, K. Abe *et al.*, *Observation of large CP violation in the neutral B meson system*, Phys. Rev. Lett. **87** (2001) 091802, arXiv:hep-ex/0107061.

[14] LHCb collaboration, R. Aaij *et al.*, *First observation of CP violation in the decays of* B_s^0 *mesons*, Phys. Rev. Lett. **110** (2013) 221601, arXiv:1304.6173.

[15] LHCb collaboration, R. Aaij *et al.*, *Observation of CP violation in charm decays*, Phys. Rev. Lett. **122** (2019) 211803, arXiv:1903.08726.

[16] N. Cabibbo, *Unitary symmetry and leptonic decays*, Phys. Rev. Lett. **10** (1963) 531.

[17] M. Kobayashi and T. Maskawa, *CP Violation in the Renormalizable Theory of Weak Interaction*, Prog. Theor. Phys. **49** (1973) 652.

[18] L. Wolfenstein, *Parametrization of the Kobayashi-Maskawa matrix*, Phys. Rev. Lett. **51** (1983) 1945.

[19] G. Antonius, *The feynman package*, http://gkantonius.github.io/feynman/index.html.

[20] I. Dunietz, R. Fleischer, and U. Nierste, *In pursuit of new physics with* B_s^0 *decays*, Phys. Rev. **D63** (2001) 114015, arXiv:hep-ph/0012219.

[21] I. Dunietz and J. L. Rosner, *Time Dependent CP Violation Effects in* B^0 *anti-*B^0 *Systems*, Phys. Rev. **D34** (1986) 1404.

[22] LHCb collaboration, R. Aaij *et al.*, *Determination of the sign of the decay width difference in the* B_s^0 *system*, Phys. Rev. Lett. **108** (2012) 241801, arXiv:1202.4717.

[23] J. van Leerdam, *Measurement of CP violation in mixing and decay of strange beauty mesons*, PhD thesis, 2016, presented 18 May 2016.

[24] P. Frings, U. Nierste, and M. Wiebusch, *Penguin contributions to CP phases in* $B_{d,s}$ *decays to charmonium*, Phys. Rev. Lett. **115** (2015) 061802, arXiv:1503.00859.

[25] K. De Bruyn, *Searching for penguin footprints: Towards high precision CP violation measurements in the B meson systems*, PhD thesis, Vrije U., Amsterdam, 2015-04-16.

[26] LHCb collaboration, R. Aaij *et al.*, *Measurement of the CP-violating phase* β *in* $\overline{B}^0 \to J/\psi\pi^+\pi^-$ *decays and limits on penguin effects*, Phys. Lett. **B742** (2015) 38, arXiv:1411.1634.

[27] LHCb collaboration, R. Aaij *et al.*, *Measurement of CP violation parameters and polarisation fractions in* $B_s^0 \to J/\psi\overline{K}^{*0}$ *decays*, JHEP **11** (2015) 082, arXiv:1509.00400.

[28] R. Fleischer, *Extracting CKM phases from angular distributions of B(d,s) decays into admixtures of CP eigenstates*, Phys. Rev. **D60** (1999) 073008, arXiv:hep-ph/9903540.

[29] S. Faller, R. Fleischer, and T. Mannel, *Precision Physics with* $B_s^0 \to J/\psi\phi$ *at the LHC: The Quest for New Physics*, Phys. Rev. **D79** (2009) 014005, arXiv:0810.4248.

[30] X. Liu, W. Wang, and Y. Xie, *Penguin pollution in* $B \to J/\psi V$ *decays and impact on the extraction of the* $B_s^0 - \overline{B}_s^0$ *mixing phase*, Phys. Rev. **D89** (2014) 094010, arXiv:1309.0313.

[31] Y. Xie, P. Clarke, G. Cowan, and F. Muheim, *Determination of* $2\beta_s$ *in* $B_s^0 \to J/\psi K^+K^-$ *Decays in the Presence of a* K^+K^- *S-Wave Contribution*, JHEP **09** (2009) 074, arXiv:0908.3627.

[32] C.-W. Chiang *et al.*, *New Physics in* $B_s^0 \to J/\psi\phi$*: A General Analysis*, JHEP **04** (2010) 031, arXiv:0910.2929.

[33] R. Lindner, *LHCb layout*, LHCb-PHO-GENE-2008-002, 2008.

[34] R. Aaij *et al.*, *Performance of the LHCb Vertex Locator*, JINST **9** (2014) P09007, arXiv:1405.7808.

[35] LHCb Collaboration, *Comparison of the decay time resolution in Run1 and Run2*, LHCB-FIGURE-2019-014, 2019.

[36] M. Adinolfi *et al.*, *Performance of the LHCb RICH detector at the LHC*, Eur. Phys. J. **C73** (2013) 2431, arXiv:1211.6759.

[37] R. Arink *et al.*, *Performance of the LHCb Outer Tracker*, JINST **9** (2014) P01002, arXiv:1311.3893.

[38] LHCb collaboration, *LHCb inner tracker: Technical Design Report*, CERN-LHCC-2002-029, 2002.

[39] LHCb collaboration, *LHCb magnet: Technical Design Report*, CERN-LHCC-2000-007, 2000.

[40] LHCb collaboration, *LHCb outer tracker: Technical Design Report*, CERN-LHCC-2001-024, 2001.

[41] P. d'Argent *et al.*, *Improved performance of the LHCb Outer Tracker in LHC Run 2*, JINST **12** (2017) P11016, arXiv:1708.00819.

[42] LHCb collaboration, *LHCb dimuon and charm mass distributions*, LHCb-CONF-2016-005, 2016.

[43] R. Aaij *et al.*, *Performance of the LHCb calorimeters*, LHCb-DP-2013-004, in preparation.

[44] LHCb collaboration, *LHCb trigger system: Technical Design Report*, CERN-LHCC-2003-031, 2003.

[45] A. A. Alves Jr. *et al.*, *Performance of the LHCb muon system*, JINST **8** (2013) P02022, arXiv:1211.1346.

[46] F. Archilli *et al.*, *Performance of the muon identification at LHCb*, JINST **8** (2013) P10020, arXiv:1306.0249.

[47] R. Aaij *et al.*, *The LHCb trigger and its performance in 2011*, JINST **8** (2013) P04022, arXiv:1211.3055.

[48] T. Sjöstrand, S. Mrenna, and P. Skands, *A brief introduction to PYTHIA 8.1*, Comput. Phys. Commun. **178** (2008) 852, arXiv:0710.3820; T. Sjöstrand, S. Mrenna, and P. Skands, *PYTHIA 6.4 physics and manual*, JHEP **05** (2006) 026, arXiv:hep-ph/0603175.

[49] I. Belyaev *et al.*, *Handling of the generation of primary events in Gauss, the LHCb simulation framework*, J. Phys. Conf. Ser. **331** (2011) 032047.

[50] D. J. Lange, *The EvtGen particle decay simulation package*, Nucl. Instrum. Meth. **A462** (2001) 152.

[51] P. Golonka and Z. Was, *PHOTOS Monte Carlo: A precision tool for QED corrections in Z and W decays*, Eur. Phys. J. **C45** (2006) 97, arXiv:hep-ph/0506026.

[52] Geant4 collaboration, J. Allison *et al.*, *Geant4 developments and applications*, IEEE Trans. Nucl. Sci. **53** (2006) 270; Geant4 collaboration, S. Agostinelli *et al.*, *Geant4: A simulation toolkit*, Nucl. Instrum. Meth. **A506** (2003) 250.

[53] M. Clemencic *et al.*, *The LHCb simulation application, Gauss: Design, evolution and experience*, J. Phys. Conf. Ser. **331** (2011) 032023.

[54] R. Aaij *et al.*, *Performance of the LHCb trigger and full real-time reconstruction in Run 2 of the LHC*, JINST **14** (2019) P04013, arXiv:1812.10790.

[55] R. Aaij *et al.*, *A comprehensive real-time analysis model at the LHCb experiment*, JINST **14** (2019) P04006, arXiv:1903.01360.

[56] A. Alfonso Albero *et al.*, *Upgrade trigger selection studies*, LHCb-PUB-2019-013, CERN, Geneva, 2019.

[57] K. Govorkova *et al.*, *A new scheduling algorithm for the LHCb upgrade trigger application*, LHCb-PROC-2020-003, 2020.

[58] K. Govorkova, *Enabling Real-Time Analysis at LHCb*, CERN-Poster-2017-579, 2017.

[59] R. Aaij *et al.*, *Tesla: an application for real-time data analysis in High Energy Physics*, Comput. Phys. Commun. **208** (2016) 35, arXiv:1604.05596.

[60] P. Koppenburg, *CP violation and CKM studies*, PoS **EPS-HEP2015** (2015) 028, arXiv:1510.01923.

[61] I. Komarov, *Measurement of* J/ψ *production cross-section in* pp *collisions at* $\sqrt{s} = 13$ *TeV at LHCb*, PoS **EPS-HEP2015** (2015) 436.

[62] LHCb collaboration, R. Aaij *et al.*, *Measurement of forward* J/ψ *production cross-sections in* pp *collisions at* $\sqrt{s} = 13$ *TeV*, JHEP **10** (2015) 172, Erratum ibid. **05** (2017) 063, arXiv:1509.00771.

[63] LHCb collaboration, R. Aaij *et al.*, *Measurements of prompt charm production cross-sections in* pp *collisions at* $\sqrt{s} = 13$ *TeV*, JHEP **03** (2016) 159, Erratum ibid. **09** (2016) 013, Erratum ibid. **05** (2017) 074, arXiv:1510.01707.

[64] LHCb collaboration, *Computing Model of the Upgrade LHCb experiment*, CERN-LHCC-2018-014, 2018.

[65] LHCb collaboration, R. Aaij *et al.*, *Observation of five new narrow* Ω_c^0 *states decaying to* $\Xi_c^+ K^-$, Phys. Rev. Lett. **118** (2017) 182001, arXiv:1703.04639.

[66] LHCb collaboration, R. Aaij *et al.*, *Observation of the doubly charmed baryon* Ξ_{cc}^{++}, Phys. Rev. Lett. **119** (2017) 112001, arXiv:1707.01621.

[67] LHCb collaboration, R. Aaij *et al.*, *Search for dark photons produced in 13 TeV*pp *collisions*, Phys. Rev. Lett. **120** (2018) 061801, arXiv:1710.02867.

[68] LHCb collaboration, R. Aaij *et al.*, *Study of* J/ψ *production in jets*, Phys. Rev. Lett. **118** (2017) 192001, arXiv:1701.05116.

[69] N. Nolte, *to be published*, PhD thesis, TU Dortmund.

[70] S. Benson and K. Gizdov, *NNDrone: a toolkit for the mass application of machine learning in High Energy Physics*, Comput. Phys. Commun. **240** (2019) 15, arXiv:1712.09114.

[71] G. Cowan, *Statistical data analysis*, Clarendon Press, Oxford, 1998.

[72] LHCb collaboration, R. Aaij *et al.*, *Updated measurement of time-dependent CP-violating observables in* $B_s^0 \to J/\psi K^+ K^-$ *decays*, Eur. Phys. J. **C79** (2019) 706, arXiv:1906.08356.

[73] H. G. Moser and A. Roussarie, *Mathematical methods for* B^0 *anti-*B^0 *oscillation analyses*, Nucl. Instrum. Meth. **A384** (1997) 491.

[74] M. Pivk and F. R. Le Diberder, *SPlot: A Statistical tool to unfold data distributions*, Nucl. Instrum. Meth. **A555** (2005) 356, arXiv:physics/0402083.

[75] W. D. Hulsbergen, *Decay chain fitting with a Kalman filter*, Nucl. Instrum. Meth. **A552** (2005) 566, arXiv:physics/0503191.

[76] L. Breiman, J. H. Friedman, R. A. Olshen, and C. J. Stone, *Classification and regression trees*, Wadsworth international group, Belmont, California, USA, 1984.

[77] R. E. Schapire and Y. Freund, *A decision-theoretic generalization of on-line learning and an application to boosting*, Jour. Comp. and Syst. Sc. **55** (1997) 119.

[78] LHCb collaboration, R. Aaij *et al.*, *Observation of* $J/\psi p$ *resonances consistent with pentaquark states in* $\Lambda_b^0 \to J/\psi p K^-$ *decays*, Phys. Rev. Lett. **115** (2015) 072001, arXiv:1507.03414.

[79] D. Martínez Santos and F. Dupertuis, *Mass distributions marginalized over per-event errors*, Nucl. Instrum. Meth. **A764** (2014) 150, arXiv:1312.5000.

[80] P. Koppenburg, *Statistical biases in measurements with multiple candidates*, arXiv:1703.01128.

[81] LHCb collaboration, R. Aaij *et al.*, *Measurements of indirect CP asymmetries in* $D^0 \to K^-K^+$ *and* $D^0 \to \pi^-\pi^+$ *decays*, Phys. Rev. Lett. **112** (2014) 041801, arXiv:1310.7201.

[82] R. Barlow, *Extended maximum likelihood*, Nuclear Instruments and Methods in Physics Research Section A: Accelerators, Spectrometers, Detectors and Associated Equipment **297** (1990) 496 .

[83] K. Govorkova, *Shape of the combinatorial background in* $B_s^0 \to J/\psi\phi$ *decay*, LHCb-INT-2019-023, CERN, Geneva, 2019.

[84] R. P. Feynman, *Very high-energy collisions of hadrons*, Phys. Rev. Lett. **23** (1969) 1415.

[85] T. Skwarnicki, *A study of the radiative cascade transitions between the* Υ' *and* Υ *resonances*, PhD thesis, Institute of Nuclear Physics, Krakow, 1986, DESY-F31-86-02.

[86] LHCb collaboration, R. Aaij *et al.*, *Measurements of the* B^+, B^0, B_s^0 *meson and* Λ_b^0 *baryon lifetimes*, JHEP **04** (2014) 114, arXiv:1402.2554.

[87] T. M. Karbach, G. Raven, and M. Schiller, *Decay time integrals in neutral meson mixing and their efficient evaluation*, arXiv:1407.0748.

[88] LHCb collaboration, R. Aaij *et al.*, *Measurement of the polarization amplitudes in* $B^0 \to J/\psi K^*(892)^0$ *decays*, Phys. Rev. **D88** (2013) 052002, arXiv:1307.2782.

[89] LHCb collaboration, R. Aaij *et al.*, *Precision measurement of CP violation in* $B_s^0 \to J/\psi K^+K^-$ *decays*, Phys. Rev. Lett. **114** (2015) 041801, arXiv:1411.3104.

[90] Heavy Flavor Averaging Group, Y. Amhis *et al.*, *Averages of b-hadron, c-hadron, and τ-lepton properties as of summer 2016*, Eur. Phys. J. **C77** (2017) 895, arXiv:1612.07233, updated results and plots available at https://hflav.web.cern.ch.

[91] A. Rogozhnikov, *Reweighting with Boosted Decision Trees*, J. Phys. Conf. Ser. **762** (2016) 012036, arXiv:1608.05806.

[92] T. du Pree, *Search for a Strange Phase in Beautiful Oscillations*, PhD thesis, Vrije U., Amsterdam, 2010.

[93] G. Punzi, *Comments on likelihood fits with variable resolution*, eConf **C030908** (2003) WELT002, arXiv:physics/0401045.

[94] D. Martinez Santos, *Study of the very rare decay $B_s^0 \to \mu^+\mu^-$ in LHCb*, PhD thesis, Santiago de Compostela U., 2010.

[95] LHCb collaboration, R. Aaij *et al.*, *Measurement of resonant and CP components in $\overline{B}{}_s^0 \to J/\psi\pi^+\pi^-$ decays*, Phys. Rev. **D89** (2014) 092006, arXiv:1402.6248.

[96] LHCb collaboration, R. Aaij *et al.*, *Precision measurement of the B_s^0–$\overline{B}{}_s^0$ oscillation frequency in the decay $B_s^0 \to D_s^-\pi^+$*, New J. Phys. **15** (2013) 053021, arXiv:1304.4741.

[97] Y. Xie, *sFit: A method for background subtraction in maximum likelihood fit*, arXiv:0905.0724.

[98] LHCb collaboration, R. Aaij *et al.*, *Measurement of CP violation and the B_s^0 meson decay width difference with $B_s^0 \to J/\psi K^+K^-$ and $B_s^0 \to J/\psi\pi^+\pi^-$ decays*, Phys. Rev. **D87** (2013) 112010, arXiv:1304.2600.

[99] LHCb collaboration, R. Aaij *et al.*, *Measurement of the CP-violating phase ϕ_s from $B_s^0 \to J/\psi\pi^+\pi^-$ decays in 13 TeV* pp *collisions*, Phys. Lett. **B797** (2019) 134789, arXiv:1903.05530.

[100] LHCb collaboration, R. Aaij *et al.*, *Measurement of the CP-violating phase ϕ_s in $\overline{B}{}_s^0 \to J/\psi\pi^+\pi^-$ decays*, Phys. Lett. **B736** (2014) 186, arXiv:1405.4140.

[101] LHCb collaboration, R. Aaij *et al.*, *Resonances and CP-violation in B_s^0 and $\overline{B}{}_s^0 \to J/\psi K^+K^-$ decays in the mass region above the $\phi(1020)$*, JHEP **08** (2017) 037, arXiv:1704.08217.

[102] LHCb collaboration, R. Aaij *et al.*, *Measurement of the CP violating phase and decay-width difference in $B_s^0 \to \psi(2S)\phi$ decays*, Phys. Lett. **B762** (2016) 253, arXiv:1608.04855.

[103] LHCb collaboration, R. Aaij *et al.*, *Measurement of the CP-violating phase ϕ_s in $\overline{B}{}_s^0 \to D_s^+D_s^-$ decays*, Phys. Rev. Lett. **113** (2014) 211801, arXiv:1409.4619.

[104] J. B. Zonneveld, *to be published*, PhD thesis, The University of Edinburgh.

[105] ATLAS collaboration, G. Aad *et al.*, *Measurement of the CP-violating phase* ϕ_s *in* $B_s^0 \to J/\psi\phi$ *decays in ATLAS at 13 TeV*, arXiv:2001.07115.

[106] CMS collaboration, V. Khachatryan *et al.*, *Measurement of the CP-violating weak phase* ϕ_s *and the decay width difference* $\Delta\Gamma_s$ *using the* $B_s^0 \to J/\psi\phi$ *decay channel in pp collisions at* $\sqrt{s} = 8$ *TeV*, Phys. Lett. **B757** (2016) 97, arXiv:1507.07527.

[107] D0 collaboration, V. M. Abazov *et al.*, *Measurement of the CP-violating phase* ${\phi_s}^{J/\psi\phi}$ *using the flavor-tagged decay* $B_s^0 \to J/\psi\phi$ *in 8* fb^{-1} *of* $p\bar{p}$ *collisions*, Phys. Rev. **D85** (2012) 032006, arXiv:1109.3166.

[108] CDF collaboration, T. Aaltonen *et al.*, *Measurement of the Bottom-Strange Meson Mixing Phase in the Full CDF Data Set*, Phys. Rev. Lett. **109** (2012) 171802, arXiv:1208.2967.

[109] T. Likhomanenko, D. Derkach, and A. Rogozhnikov, *Inclusive Flavour Tagging Algorithm*, J. Phys. Conf. Ser. **762** (2016) 012045, arXiv:1705.08707.

Summary

WHAT?

This thesis is dedicated to the measurement of the CP violating phase ϕ_s which arises in $B_s^0 \to J/\psi\phi$ and $\overline{B}_s^0 \to J/\psi\phi$ decays. Sounds complicated, so let's first start with a brief overview of the universe and what we know about it. Everything we see around is made of several types of fundamental particles of different masses and charges. They interact with each other by means of fundamental forces. Under the C (charge)-transformation, each particle converts into an associated anti-particle, which has the same mass but opposite charges. The P (parity)-transformation inverts all space coordinates and therefore reverts the direction of particle momentum. If we look in a special mirror, which reverts both C and P, then the reflection in such a mirror would behave slightly differently from the original. This is what is called CP violation.

Elementary particles are bound together to form other particles, such as B_s^0 mesons which are combinations of two quarks, namely bottom, $\overline{b}$, and strange, s. The B_s^0 particle is unstable with a lifetime of only around 1.5×10^{-12} seconds! It can decay to various other particles, but the ones that we will search for are the J/ψ and ϕ mesons. The J/ψ is made of charm, c, and anti-charm, $\overline{c}$, quarks; it is also an unstable particle. Among other possibilities, it can decay to two leptons, μ^+ and μ^-, and that's what is looked for. The ϕ is made of s, and $\overline{s}$ quarks, and is an unstable particle as well. The decay $\phi \to K^+K^-$ is of interest, where $K^\pm$ is a hadron composed of up, u ($\overline{u}$), and $\overline{s}$ (s) quarks. An additional complication arises due to the fact that B_s^0 meson during its lifetime can transition into $\overline{B}_s^0$ meson and vice-versa. This interchange happens on average 27 times before the decay. So, there are two possible processes that can happen, a B_s^0 meson can decay to $J/\psi\phi$ or it first transitions into its anti-particle, $\overline{B}_s^0$, and then decays to J/ψ and ϕ particles. If we look at the $B_s^0 \to J/\psi\phi$ decay in our special CP mirror, we will see the $\overline{B}_s^0$ decaying to J/ψ and ϕ particles, which are their own anti-particles. A $\overline{B}_s^0$ meson can also either decay directly to $J/\psi\phi$ or first turn into a B_s^0 meson. After having a careful look, we will be able to tell if the mirror image is different from the original, e.g. if the probabilities for the processes and anti-processes are the same. The parameter which characterises this difference is called ϕ_s. In the Standard Model of elementary particles, this parameter is expected to be very small, $-0.03698^{+0.00081}_{-0.00070}$ rad, meaning that the $B_s^0 \to J/\psi\phi$ and $\overline{B}_s^0 \to J/\psi\phi$ decays proceed in an almost identical way.

WHY?

Why is the measurement of ϕ_s important? If the measured value for ϕ_s would be different from the expected one, then it would mean that there are new, unknown effects appearing in the $B_s^0 \to J/\psi\phi$ and $\overline{B}_s^0 \to J/\psi\phi$ decays. In particular, there can be a new fundamental particle that enters the processes of B_s^0-$\overline{B}_s^0$ transition and which modifies the prediction of ϕ_s. Such an approach to search for new particles is called an indirect search, where only the consequences of a particle are observed rather then the particle itself. If the mass of a new particle is much larger than the energies accessible experimentally, then it cannot be produced and detected in a direct search. However, this new particle will most likely modify a number of distinct processes and therefore can be observed indirectly and some of its properties can be derived. This increased reach is a great advantage of the indirect approach.

HOW?

How can one possibly measure the value of ϕ_s? First of all, particles such as B_s^0 are not present in the usual matter around us, so they have to be created. One of the main factories for particle production is the LHC accelerator at CERN, where protons are accelerated to speeds approximately 0.999999997 times the speed of light. They are then collided with each other and some of the energy of the collision is transformed into particles. In some of these collisions a B_s^0 meson is produced, which decays shortly after. To catch it and its decay products, detectors are build around the collision points. The detector that is specifically designed to look at particles containing bottom quarks is LHCb. The unique design of the experiment is chosen to maximally cover the forward region, thus catching most of the decay products of the b quark. Inside LHCb, proton collisions happen around 30 million times every second. A dedicated system of the experiment, the trigger, is designed to select "interesting" events from the enormous amount of pp collisions. In this particular case, "interesting" events are those that contain the $B_s^0 \to J/\psi\phi$ or $\overline{B}_s^0 \to J/\psi\phi$ decay. The trigger system is a sophisticated architecture that has to operate extremely fast and efficiently select interesting events. The more relevant events are selected, the more precise the measurement of ϕ_s will be.

Detecting all the decay products, $J/\psi \to \mu^+\mu^-$ and $\phi \to K^+K^-$, allows the reconstruction of the original B_s^0 or $\overline{B}_s^0$ meson. Specific algorithms distinguish whether this meson was a B_s^0 or $\overline{B}_s^0$. The meson travels, on average, a distance of approximately 1 cm inside the LHCb detector. The measurement of this distance allows the calculation of the decay time for each found B_s^0 ($\overline{B}_s^0$) particle. Comparing the probability of their decays to the same $J/\psi\phi$ final state then leads to the measurement of ϕ_s. In case the processes in the CP mirror is identical, ϕ_s would be exactly zero. The more different the CP image is, the larger the value of ϕ_s would be.

RESULT

What's is the result of the measurement? For the measurement of the CP violation described in this thesis, proton-proton collisions which happened at LHCb in 2015 and 2016 are used. In around 117 000 events out of these collisions either a $B_s^0 \to J/\psi\phi$ or $\overline{B}_s^0 \to J/\psi\phi$ decay was found. These are used to determine ϕ_s, which is measured to be

$$\phi_s = -0.083 \pm 0.041 \pm 0.006\,\text{rad}$$

where the first uncertainty is due to the limited number of B_s^0 decays found and the second one is due to the imperfect methods used to perform the measurement. Within uncertainties, the result is consistent with the expected value. The ϕ_s parameter describes CP violation not only in the decays of B_s^0-$\overline{B}_s^0$ system to the $J/\psi\phi$ final state, but also in other decays such as $B_s^0 \to J/\psi\pi^+\pi^-$, $B_s^0 \to J/\psi K^+K^-$ for the m_{KK} region above $1.05\,\text{GeV}/c^2$, $B_s^0 \to \psi(2S)\phi$ and $B_s^0 \to D_s^+D_s^-$. The results of the ϕ_s measurements using all of these decays performed at LHCb are combined, yielding the following value:

$$\phi_s = -0.042 \pm 0.025\,\text{rad}$$

where uncertainty reflects both the limited number of B_s^0 decays found and the imperfect tools for the measurements.

WHAT'S NEXT?

The indirect determination, assuming the validity of the Standard Model, of the value of ϕ_s is much more precise than the current experimental determination, which means that there is still possibility for new particles to show up. To catch them or to make sure that they are not there, it is essential to decrease the uncertainty on the measurement, which means to collect more data, while keeping improving the methods and tools of the measurement. In the following years, the data collected in LHCb in 2017 and 2018 will be analysed and the statistical uncertainty on the measured value of ϕ_s will decrease by a factor of around 1.7, bringing us closer to unravelling possible sources of New Physics. This measurement will be followed with one performed on data that will be collected at the upgraded version of the LHCb experiment, where major parts of the detector will be replaced to get an optimal performance. The hunt for New Physics with $B_s^0 \to J/\psi\phi$ decays will continue until it will become clear whether there are, or are not, new particles hiding in the process.

Samenvatting

WAT?

Deze dissertatie is toegewijd aan de meting van de CP-schendende fase ϕ_s die voortkomt uit $B_s^0 \to J/\psi\phi$ en $\overline{B}_s^0 \to J/\psi\phi$ vervallen. Dit klinkt ingewikkeld, dus laten we eerst beginnen met een kort overzicht van het universum en wat we er over weten. Alles wat we om ons heen zien bestaat uit verscheidene types van fundamentele deeltjes met verschillende massa's en ladingen. Zij gaan interacties met elkaar aan door middel van fundamentele krachten. Onder de C-transformatie ('charge', *i.e.* lading) converteert elk deeltje in een geassocieerd anti-deeltje dat dezelfde massa, maar tegenovergestelde lading heeft. De P-transformatie (pariteit) inverteert alle ruimtecoördinaten en daarom keert ook de richting van de impuls van het deeltje om. Wanneer we in een speciale spiegel kijken die zowel de C- als P-transformatie toepast, zou de reflectie in zo een spiegel er een beetje anders uitzien dan het origineel. Dit wordt CP-schending genoemd.

Fundamentele deeltjes kunnen aan elkaar binden om andere deeltjes te vormen zoals B_s^0-mesonen, die combinaties zijn van twee quarks, in dit geval, 'bottom' ofwel $\bar{b}$, en 'strange', ofwel s. Het B_s^0-deeltje is instabiel met een levensduur van rond de 1.5×10^{-12} seconden, miljoenste van een miljoenste van een seconde! Het B_s^0-meson kan vervallen naar allerlei deeltjes, maar de vervalsproducten waar wij naar zoeken zijn J/ψ- en ϕ-mesonen. De J/ψ bestaat uit een 'charm'-, ofwel c, en een 'anti-charm'-quark; het is zelf ook instabiel. Het kan onder andere vervallen naar twee leptonen, μ^+ en μ^-, en daar zoeken wij naar. De ϕ bestaat uit een s- en een $\bar{s}$-quark en is ook instabiel. Voor ons is het vervalsproces $\phi \to K^+K^-$ van belang, waar $K^\pm$-hadronen bestaan uit een u ($\bar{u}$) en een $\bar{s}$ (s)-quark. Tijdens de levensduur van een B_s^0-meson kan het overgaan naar een $\overline{B}_s^0$-meson en vice versa. Deze overgang gebeurt gemiddeld 27 keer voordat het deeltje vervalt. Daarom kunnen B_s^0-mesonen ófwel direct vervallen naar $J/\psi\phi$, ófwel eerst overgaan naar een $\overline{B}_s^0$-meson om vervolgens te vervallen naar J/ψ- en ϕ-deeltjes. Wanneer we kijken naar het verval van $B_s^0 \to J/\psi\phi$ in onze speciale CP-spiegel, zullen we zien dat in de reflectie het $\overline{B}_s^0$-meson ook naar J/ψ- en ϕ-deeltjes vervalt, aangezien de laatste twee hun eigen anti-deeltjes zijn. Omgekeerd kan een $\overline{B}_s^0$-meson ook direct vervallen naar $J/\psi\phi$ of eerst overgaan naar een B_s^0-meson. Na een zorgvuldige blik is het mogelijk om te bepalen of het spiegelbeeld verschilt van het origineel, *i.e.* of de kansen van het verval of het anti-verval hetzelfde zijn. De

parameter die dit verschil karakteriseert wordt ϕ_s genoemd. In het Standaard Model van de fundamentele deeltjes wordt verwacht dat deze parameter erg klein is, $-0.03698^{+0.00081}_{-0.00070}$ rad, wat betekent dat de vervallen van $B_s^0 \to J/\psi\phi$ en $\overline{B}_s^0 \to J/\psi\phi$ op een bijna identieke wijze gebeuren.

WAAROM?

Waarom is een meting van ϕ_s belangrijk? Als de gemeten waarde van ϕ_s anders zou zijn dan de verwachte waarde, betekent het dat er nieuwe, onbekende effecten tevoorschijn komen in de $B_s^0 \to J/\psi\phi$ en $\overline{B}_s^0 \to J/\psi\phi$ vervallen. In het bijzonder zou er een nieuw fundamenteel deeltje kunnen bijdragen aan de B_s^0-$\overline{B}_s^0$-transities en zodoende de waarde van ϕ_s kunnen veranderen. Een dergelijke aanpak om te zoeken naar nieuwe deeltjes wordt ook wel een indirecte zoektocht genoemd, waar de consequenties van een deeltje worden waargenomen in tegenstelling tot het deeltje zelf. Als de massa van het nieuwe deeltje veel groter is dan de energieën die experimenteel toegankelijk zijn, zou die niet geproduceerd kunnen worden en niet waargenomen worden met een directe zoektocht. Tegelijkertijd zou zo een nieuw deeltje waarschijnlijk wel processen zoals $B_s^0 \to J/\psi\phi$ beinvloeden en daarmee indirect waargenomen kunnen worden. Vervolgens zouden sommige eigenschappen van het deeltje kunnen worden bepaald. Dit toegenomen bereik is een groot voordeel van de indirecte aanpak.

HOE?

Hoe kan men de waarde van ϕ_s bepalen? Ten eerste, deeltjes zoals B_s^0-mesonen zijn niet aanwezig in de gebruikelijke materie om ons heen en daarom moeten ze worden gecreëerd. Een van de hoofdfabrieken voor deeltjesproductie is de LHC-versneller bij CERN, waar protonen worden versneld tot snelheden van ongeveer 0.999999997 keer de lichtsnelheid. Vervolgens worden ze op elkaar gebotst en wordt een gedeelte van de energie van de botsing omgezet in nieuwe deeltjes. In sommige van die botsingen worden B_s^0-mesonen geproduceerd, die vervolgens kort daarna vervallen. Om de vervalsproducten op te vangen zijn detectoren om de botsingspunten geplaatst. De detector die specifiek ontworpen is om deeltjes die bottom-quarks bevatten te bestuderen is LHCb. Het unieke ontwerp van het experiment is gekozen om de voorwaartse richting maximaal te omvatten, wat er voor zorgt dat veel van de vervalsproducten van b-quarks gevangen kunnen worden. Binnen LHCb gebeuren protonbotsingen ongeveer 30 miljoen keer per seconde. Een systeem van het experiment, de 'trigger', is speciaal ontworpen om interessante gebeurtenissen te selecteren uit het enorme aantal pp-botsingen. In dit geval zijn interessante gebeurtenissen diegenen die de $B_s^0 \to J/\psi\phi$ en $\overline{B}_s^0 \to J/\psi\phi$ vervallen bevatten. Het trigger-systeem is een geavanceerde architectuur die extreem snel en efficiënt moet kunnen werken om interessante gebeurtenissen te selecteren. Hoe meer relevante gebeurtenissen worden geselecteerd, hoe preciezer de meting van ϕ_s zal zijn.

Het detecteren van alle vervalsproducten, $J/\psi \to \mu^+\mu^-$ en $\phi \to K^+K^-$, staat de reconstructie toe van het originele B_s^0- of $\overline{B}_s^0$-meson. Specifieke algorithmes

onderscheiden of het meson een B_s^0 of $\overline{B}_s^0$ was. Het meson reist gemiddeld een afstand van ongeveer 1 cm binnen de LHCb-detector. De meting van deze afstand maakt de berekening van de levensduur mogelijk voor elk B_s^0 ($\overline{B}_s^0$)-deeltje. De vergelijking van de kans van het verval van B_s^0 en $\overline{B}_s^0$ naar dezelfde $J/\psi\phi$-eindtoestand leidt vervolgens tot de meting van ϕ_s. In het geval dat de processen in het CP-spiegelbeeld hetzelfde zijn, zou ϕ_s precies nul zijn. Hoe meer het CP-spiegelbeeld anders is dan het origineel, hoe groter de waarde van ϕ_s zal zijn.

RESULTAAT

Wat is het resultaat van de meting? Voor de meting van de CP-schending die beschreven is in deze dissertatie zijn protonbotsingen gebruikt die gedetecteerd zijn door LHCb in 2015 en 2016. In rond de 117.000 gebeurtenissen van deze botsingen zijn ófwel een $B_s^0 \to J/\psi\phi$, ófwel een $\overline{B}_s^0 \to J/\psi\phi$ verval gevonden. Deze vervallen zijn gebruikt om ϕ_s te bepalen, en de gemeten waarde is

$$\phi_s = -0.083 \pm 0.041 \pm 0.006\,\text{rad}$$

waar de eerste onzekerheid komt van de beperkte hoeveelheid B_s^0-vervallen die zijn gevonden en de tweede door de imperfecties in de methode die is gebruikt om de meting te doen. Binnen de onzekerheden is het resultaat consistent met de verwachte waarde. De ϕ_s-parameter beschrijft CP-schending niet alleen in de vervallen van het B_s^0-$\overline{B}_s^0$-systeem naar de $J/\psi\phi$-eindtoestand, maar ook andere vervallen zoals $B_s^0 \to J/\psi\pi^+\pi^-$, $B_s^0 \to J/\psi K^+K^-$ voor de m_{KK}-regio boven $1.05\,\text{GeV}/c^2$, $B_s^0 \to \psi(2S)\phi$ and $B_s^0 \to D_s^+D_s^-$. De combinatie van de metingen van ϕ_s die gebruik maken van al deze vervallen binnen LHCb resulteert in de gecombineerde meting:

$$\phi_s = -0.042 \pm 0.025\,\text{rad}$$

waar de onzekerheid zowel het effect van het beperkte aantal B_s^0-vervallen die zijn gevonden, als de imperfecte methoden van de metingen beschrijft.

WAT VOLGT?

De indirecte bepaling van de waarde van ϕ_s, onder de hypothese van het Standaard Model, is veel preciezer dan de huidige experimentele bepaling, wat betekent dat er nog steeds een mogelijkheid is dat nieuwe deeltjes de waarde van ϕ_s beinvloeden. Om deze te vangen of er zeker van te zijn dat ze er niet zijn, is het essentieel om de onzekerheid van de meting te verkleinen. Dat betekent dat meer data moet worden verkregen en dat de meting van de data moet worden verbeterd. In de komende jaren wordt data die verkregen is bij LHCb in 2017 and 2018 geanalyseerd en zal de statistische onzekerheid van de gemeten waarde van ϕ_s omlaag gaan met een factor van rond de 1.7, wat ons dichterbij het ontrafelen van mogelijke bronnen van nieuwe fenonemen brengt. Hierna zal een meting volgen die zal worden toegepast op data die wordt verkregen met de nieuwere versie van het LHCb-experiment, waar grote delen van de detector vervangen

zullen zijn om zowel meer, als ook meer nauwkeurige data te kunnen verzamelen. De jacht naar nieuwe fenonemen met $B_s^0 \to J/\psi\phi$ vervallen zal doorgaan todat het duidelijk wordt of er wel of niet nieuwe deeltjes schuilen in dit proces.

Acknowledgments

If you are reading this, chances are that we have met during my PhD journey and therefore you've contributed to it in a way. Thank you for this.

The four years of my PhD at Nikhef were a great adventure. One of the reasons is my supervisor. Gerhard, it was fantastic to brainstorm with you on physics ideas and learn from your great experience. I'm very grateful for the freedom you gave me in pursuing research, dankjewel. Patrick, thank you for helping with making this manuscript readable, especially for your patience with *the* articles.

One of the main reasons why doing research at Nikhef bfys group is so great is its amazing atmosphere of eagerness and desire to share and learn. Marcel (aka Baas-1284184214), thank you for carrying out the attitude of the group through the years and encouraging your kids to speak up with Friday cookies. Of course I want to thank each person in the group: Aleksandra, Antonio, Carlos, Cristina, Daniel, Elena, Flavio, Greg, Igor, Jacco, Jeroen, Jordy, Kazu, Laurent, Lennaert, Lera, Lex, Mara, Marjolein, Mauricio, Maxime, Michele, Niels, Sean, Sevda, Silvia, Tjeerd and Wouter. Maarten and Mick, as my scientific besties and translators of my summary, you got a special thank you.

The analysis described in my thesis was performed in collaboration with the $J/\psi\phi$ team, thank you, Francesca, Greig, Jennifer, Konstantin, Liming, Simon, Veronika and Wenhua.

During my detachment at CERN, I collaborated with amazing people from trigger group, thank you, Conor, Niklas, Rosen, Sascha and Vava. Alex, even though I didn't manage to bring you to the $J/\psi\phi$ team, I'm very grateful for everything that you have taught me.

Most importantly, I would not be able to make it without the support of my family.

Семья, спасибо.